

Air Force Institute of Technology

AFIT Scholar

Theses and Dissertations

Student Graduate Works

3-2002

A Novel Electrocardiogram Segmentation Algorithm Using a Multiple Model Adaptive Estimator

Gregory S. Hoffman

Follow this and additional works at: <https://scholar.afit.edu/etd>



Part of the [Medicine and Health Sciences Commons](#)

Recommended Citation

Hoffman, Gregory S., "A Novel Electrocardiogram Segmentation Algorithm Using a Multiple Model Adaptive Estimator" (2002). *Theses and Dissertations*. 4450.

<https://scholar.afit.edu/etd/4450>

This Thesis is brought to you for free and open access by the Student Graduate Works at AFIT Scholar. It has been accepted for inclusion in Theses and Dissertations by an authorized administrator of AFIT Scholar. For more information, please contact richard.mansfield@afit.edu.



**A NOVEL ELECTROCARDIOGRAM
SEGMENTATION ALGORITHM USING A
MULTIPLE MODEL ADAPTIVE
ESTIMATOR**

THESIS

Gregory S. Hoffman, 2Lt, USAF
AFIT/GE/ENG/02M-10

**DEPARTMENT OF THE AIR FORCE
AIR UNIVERSITY**

AIR FORCE INSTITUTE OF TECHNOLOGY

Wright-Patterson Air Force Base, Ohio

APPROVED FOR PUBLIC RELEASE; DISTRIBUTION UNLIMITED.

Report Documentation Page

Report Date 26 Mar 02	Report Type Final	Dates Covered (from... to) Aug 2000 - Mar 2002
Title and Subtitle A Novel Electrocardiogram Segmentation Algorithm Using a Multiple Model Adaptive Estimator	Contract Number	
	Grant Number	
	Program Element Number	
Author(s) 2Lt Gregory S. Hoffman, USAF	Project Number	
	Task Number	
	Work Unit Number	
Performing Organization Name(s) and Address(es) Air Force Institute of Technology Graduate School of Engineering and Management (AFIT/EN) 2950 P Street, Bldg 640 WPAFB OH 45433-7765	Performing Organization Report Number AFIT/GE/ENG/02M-10	
Sponsoring/Monitoring Agency Name(s) and Address(es)	Sponsor/Monitor's Acronym(s)	
	Sponsor/Monitor's Report Number(s)	
Distribution/Availability Statement Approved for public release, distribution unlimited		
Supplementary Notes		

Abstract

This thesis presents a novel electrocardiogram (ECG) processing algorithm design based on a Multiple Model Adaptive Estimator (MMAE) for a physiological monitoring system. Twenty ECG signals from the MIT ECG database were used to develop system models for the MMAE. The P-wave, QRS complex, and T-wave segments from the characteristic ECG waveform were used to develop hypothesis filter banks. By adding a threshold filter-switching algorithm to the conventional MMAE implementation, the device mimics the way a human analyzer searches the complex ECG signal for a useable temporal landmark and then branches out to find the other key wave components and their timing. The twenty signals and an additional signal from an animal exsanguination experiment were then used to test the algorithm. Using a conditional hypothesis-testing algorithm, the MMAE correctly identified the ECG signal segments corresponding to the hypothesis models with a 96.8% accuracy-rate for the 11539 possible segments tested. The robust MMAE algorithm also detected any misalignments in the filter hypotheses and automatically restarted filters within the MMAE to synchronize the hypotheses with the incoming signal. Finally, the MMAE selects the optimal filter bank based on incoming ECG measurements. The algorithm also provides critical heart-related information such as heart rate, QT, and PR intervals from the ECG signal. This analyzer could be easily added as a software update to the standard physiological monitors universally used in emergency vehicles and treatment facilities and potentially saving thousands of lives and reducing the pain and suffering of the injured.

Subject Terms

Physiological monitoring, vital-sign monitoring, MMAE, ECG, Electrocardiogram

Report Classification

unclassified

Classification of this page

unclassified

Classification of Abstract

unclassified

Limitation of Abstract

UU

Number of Pages

177

The views expressed in this thesis are those of the author and do not reflect the official policy or position of the United States Air Force, Department of Defense, or the U. S. Government.

AFIT/GE/ENG/02M-10

A NOVEL ELECTROCARDIOGRAM SEGMENTATION ALGORITHM USING A
MULTIPLE MODEL ADAPTIVE ESTIMATOR

THESIS

Presented to the Faculty

Department of Electrical and Computer Engineering

Graduate School of Engineering and Management

Air Force Institute of Technology

Air University

Air Education and Training Command

In Partial Fulfillment of the Requirements for the
Degree of Master of Science in Electrical Engineering

Gregory S. Hoffman, B.S.

2Lt, USAF

March 2002

APPROVED FOR PUBLIC RELEASE; DISTRIBUTION UNLIMITED.

A NOVEL ELECTROCARDIOGRAM SEGEMENTATION ALGORITHM USING A
MULTIPLE MODEL ADAPTIVE ESTIMATOR


Gregory S. Hoffman, BS
2Lt, USAF

Approved:



Lieutenant Colonel Mikel M. Miller, Ph.D.
Assistant Professor, Committee Chairman

14 Mar 02
Date




Dr. Matthew Kabrisky
Professor Emeritus, Committee Member

18 MAR 02
Date



Dr. Peter S. Maybeck
Professor, Committee Member

14 MAR 02
Date



Major John F. Raquet, Ph.D.
Assistant Professor, Committee Member

14 MAR 02
Date

Acknowledgments

Special thanks to everyone who made this thesis possible: my committee, my classmates, my roomies, and my “peeps.” My advisor, LtCol Miller deserves my deepest thanks for keeping me on track and helping me see the big picture when I got frustrated. His motivation and excitement about this topic were greatly appreciated.

Dr. Maybeck brought a great deal of experience and insight to this new use of the MMAE. His enthusiasm and ideas seem to never end. The preparation for this thesis EENG 768 project was invaluable to making this algorithm come to fruition. I know that when you weigh this effort you will not find it lacking.

Dr. Kabrisky provided much needed insight into the physiological aspects of this research. His knowledge of biomedical and bioengineering applications is second to none.

Maj Raquet saw that I would never accomplish every goal I had for this thesis and bluntly told me to narrow it down. In one word—thanks. I never would have finished if it weren't for that sound advice.

Everyone in the GNC lab—it's been fun. Don, thanks for all your help with the shirt. I am sure it will all come together. Bethany, thanks for all of your research and help over the summer. Dave, thanks for being a great roomie. Your general lack of desire to learn was outstanding! Nugget, aren't you supposed to retire after 54 years in the service? I'll see you on the course. Paps, mate, the best Australian-Wisconsin accent ever. I'll come visit Perth sometime. Best of luck to you back in Australia. Last, but certainly not least, I am eternally grateful to my family for all their love.

Greg Hoffman

Table of Contents

Acknowledgments.....	iv
Table of Contents.....	v
List of Figures.....	viii
List of Tables.....	xiii
Notation.....	xiv
Acronym List.....	xv
Abstract.....	xvi
1. Introduction.....	1-1
1.1 Background.....	1-1
1.2 Research Objectives.....	1-3
1.3 Summary of Current Knowledge.....	1-4
1.4 Scope.....	1-7
1.5 Approach/Methodology.....	1-8
1.5.1. Analysis of ECG parameters.....	1-8
1.5.2. Development of ECG System Models for the MMAE.....	1-9
1.5.3. ECG Processing Software Testing and Validation.....	1-9
1.6 Thesis Overview.....	1-10
1.7 Summary.....	1-11
2. Current Knowledge.....	2-1
2.1 Introduction.....	2-1
2.2 Physiological Health Research.....	2-2
2.2.1. Physiological Sensor Information.....	2-3
2.2.1.1 Respiration Monitoring.....	2-3
2.2.1.2 Electrocardiogram.....	2-7
2.2.2. Physiological Monitoring Outside a Doctor's Office.....	2-14

2.3	Importance of GPS	2-20
2.4	Kalman Filter.....	2-22
2.4.1.	Multiple Model Adaptive Estimator (MMAE).....	2-26
2.4.2.	State Estimation vs. Parameter Estimation.....	2-30
2.4.3.	Lower Probability Bounds.....	2-31
2.5	Summary	2-31
3.	Methodology	3-1
3.1	Overview.....	3-1
3.2	Design and Analysis Process	3-1
3.3	ECG signal analysis.....	3-2
3.3.1.	Differentiator	3-3
3.3.2.	Signal Assumptions.....	3-5
3.3.3.	Correlation and Power Spectral Density Functions	3-5
3.4	System Modeling.....	3-9
3.4.1.	Hypothesis Filter Parameters.....	3-11
3.5	Kalman Filter Design.....	3-12
3.5.1.	Multiple Model Adaptive Estimator (MMAE) Design.....	3-15
3.5.2.	Lower Probability Bounds.....	3-17
3.5.3.	Hypothesis Filter Tuning.....	3-18
3.6	Hypothesis Determination Smoothing.....	3-20
3.6.1.	Hypothesis Swapping.....	3-21
3.6.2.	Hypothesis Bank Restart	3-23
3.7	RR, QT, and PR Interval Determination.....	3-24
3.8	Hypothesis Model Evolution.....	3-26
3.9	Changing Heart Rate and Changing Physiological Condition.....	3-29
3.10	Overall MMAE ECG Processing Algorithm Description	3-33
3.11	Summary	3-34
4.	Analysis of Results	4-1
4.1	Overview.....	4-1
4.2	MIT ECG Signal Analysis	4-1

4.2.1.	Sample ECG 3 Signal 1 and Other Fine Performance Examples	4-3
4.2.2.	Sample ECG 3 Signal 2 and Other Examples of Poor Performance	4-10
4.3	Animal Exsanguination ECG Data.....	4-16
4.3.1.	Analysis of Problem Samples Q4 and Q9	4-22
4.3.2.	Analysis of Problem Sample Q 14.....	4-24
4.3.3.	Analysis of Problem Sample Q 16, Q 17, Q 18.....	4-26
4.4	Summary	4-27
5.	Conclusions and Recommendations.....	5-1
5.1	Overview	5-1
5.2	Conclusion	5-2
5.3	Recommendations	5-5
5.4	Summary	5-10
Appendix A.	MIT ECG Figures	A-1
Appendix B.	ION GPS-2001 Paper	B-1
Bibliography	Bib-1
Vita.....	Vit-1

List of Figures

Figure 2-1. Absorption Coefficients for Hemoglobin and Oxyhemoglobin Relative to Light Wavelength (nm).....	2-4
Figure 2-2. Absorption as Light Passes Through the Body [19].	2-5
Figure 2-3. Typical Pulse Oximeter Placement [20].....	2-5
Figure 2-4. ECG Characteristic Waveform Corresponding to Heart Activity [23],[24].	2-8
Figure 2-5. Einthoven's Triangle of ECG Electrode Placement [25]	2-10
Figure 2-6. Diagram of Artificial Neural Network [36].....	2-13
Figure 2-7. GPS Constellation	2-20
Figure 2-8. Multiple Model Filtering Algorithm Block Diagram	2-28
Figure 3-1. Algorithm Development and Testing Process	3-2
Figure 3-2. FIR Differentiator	3-3
Figure 3-3. Sample ECG Signal, ECG Signal 1 st Derivative, and 2 nd Derivative	3-4
Figure 3-4. PSD Estimate for Sample QRS Complex Segment and 1 st Derivative.....	3-7
Figure 3-5. PSD Estimate for Sample T-Wave Segment and 1 st Derivative.....	3-8
Figure 3-6. PSD Estimate for Sample P-Wave Segment and 1 st Derivative	3-8
Figure 3-7. Online Hypothesis Swapping Algorithm	3-21
Figure 3-8. MMAE Online Restart Routine for Synchronization	3-24
Figure 3-9. Algorithm for RR, QT, and PR Interval Determination.....	3-25
Figure 3-10. Processing of Evaluation and Developing Filter Models.....	3-27
Figure 3-11. Offline Filter Bank Switch Algorithm	3-31
Figure 3-12. Algorithm Initialization Restart Flow Diagram.....	3-32
Figure 3-13. MMAE ECG Processing Flow Chart with Subroutines.....	3-34
Figure 4-1. Maximal Likelihood Filter Hypothesis for Sample 3 Signal 1	4-4
Figure 4-2. ECG Sample 3 Signal 1 Heart Rate	4-5
Figure 4-3. ECG Sample 3 Signal 1 QT Interval.....	4-6
Figure 4-4. ECG Sample 3 Signal 1 QTc Interval.....	4-7

Figure 4-5. ECG Sample 3 Signal 1 PR Interval	4-8
Figure 4-6. Maximal Likelihood Filter Hypothesis for Sample 3 Signal 2.....	4-11
Figure 4-7. ECG Sample 3 Signal 2 Heart Rate	4-12
Figure 4-8. ECG Sample 3 Signal 2 QT Interval.....	4-13
Figure 4-9. ECG Sample 3 Signal 2 QTc Interval.....	4-14
Figure 4-10. ECG 3 Signal 2 PR Interval.....	4-15
Figure 4-11. Animal Heart Rate During Exsanguination.....	4-18
Figure 4-12. Animal Exsanguination QT Interval.....	4-19
Figure 4-13. Animal Exsanguination QTc Interval	4-20
Figure 4-14. Animal Exsanguination PR Interval and PR Interval Variance.....	4-21
Figure 4-15. Representative ECG Sample from Q 4 with MAP Hypothesis	4-22
Figure 4-16. Representative ECG Sample from Q 9 with MAP Hypothesis	4-23
Figure 4-17. Representative ECG Sample from Q 14 with MAP Hypothesis	4-25
Figure 4-18. Representative ECG Sample from Q 17 with MAP Hypothesis	4-27
Figure A-1. ECG Sample 3 Signal 1 Heart Rate	A-1
Figure A-2. ECG Sample 3 Signal 1 QT Interval and QTc Interval.....	A-1
Figure A-3. ECG Sample 3 Signal 1 PR Interval	A-2
Figure A-4. Maximal Likelihood Filter Hypothesis for Sample 3 Signal 1.....	A-2
Figure A-5. ECG Sample 3 Signal 2 Heart Rate	A-2
Figure A-6. ECG Sample 3 Signal 2 QT Interval and QTc Interval.....	A-3
Figure A-7. ECG 3 Signal 2 PR Interval.....	A-3
Figure A-8. Maximal Likelihood Filter Hypothesis for Sample 3 Signal 2.....	A-3
Figure A-9. ECG Sample 5 Signal 1 Heart Rate	A-4
Figure A-10. ECG Sample 5 Signal 1 QT Interval and QTc Interval.....	A-4
Figure A-11. ECG Sample 5 Signal 1 PR Interval	A-4
Figure A-12. Maximal Likelihood Filter Hypothesis for Sample 5 Signal 1.....	A-5
Figure A-13. ECG Sample 5 Signal 2 Heart Rate	A-5
Figure A-14. ECG Sample 5 Signal 2 QT Interval and QTc Interval.....	A-5
Figure A-15. ECG Sample 5 Signal 2 PR Interval	A-6

Figure A-16. Maximal Likelihood Filter Hypothesis for Sample 5 Signal 2.....	A-6
Figure A-17. ECG Sample 11 Signal 1 Heart Rate	A-6
Figure A-18. ECG Sample 11 Signal 1 QT Interval and QTc Interval.....	A-7
Figure A-19. ECG Sample 11 Signal 1 PR Interval	A-7
Figure A-20. Maximal Likelihood Filter Hypothesis for Sample 11 Signal 1	A-7
Figure A-21. ECG Sample 11 Signal 2 Heart Rate	A-8
Figure A-22. ECG Sample 11 Signal 2 QT Interval and QTc Interval.....	A-8
Figure A-23. ECG Sample 11 Signal 2 PR Interval	A-8
Figure A- 24. Maximal Likelihood Filter Hypothesis for Sample 11 Signal 2	A-9
Figure A-25. ECG Sample 13 Signal 1 Heart Rate	A-9
Figure A-26. ECG Sample 13 Signal 1 QT Interval and QTc Interval.....	A-9
Figure A-27. ECG Sample 13 Signal 1 PR Interval	A-10
Figure A-28. Maximal Likelihood Filter Hypothesis for Sample 13 Signal 1	A-10
Figure A-29. ECG Sample 13 Signal 2 Heart Rate	A-10
Figure A-30. ECG Sample 13 Signal 2 QT Interval and QTc Interval.....	A-11
Figure A-31. ECG Sample 13 Signal 2 PR Interval	A-11
Figure A-32. Maximal Likelihood Filter Hypothesis for Sample 13 Signal 2.....	A-11
Figure A-33. ECG Sample 19 Signal 1 Heart Rate	A-12
Figure A-34. ECG Sample 19 Signal 1 QT Interval and QTc Interval.....	A-12
Figure A-35. ECG Sample 19 Signal 1 PR Interval	A-12
Figure A-36. Maximal Likelihood Filter Hypothesis for Sample 19 Signal 1	A-13
Figure A-37. ECG Sample 19 Signal 2 Heart Rate	A-13
Figure A-38. ECG Sample 19 Signal 2 QT Interval and QTc Interval.....	A-13
Figure A-39. ECG Sample 19 Signal 2 PR Interval	A-14
Figure A-40. Maximal Likelihood Filter Hypothesis for Sample 19 Signal 2.....	A-14
Figure A-41. ECG Sample 21 Signal 1 Heart Rate	A-14
Figure A-42. ECG Sample 21 Signal 1 QT Interval and QTc Interval.....	A-15
Figure A-43. ECG Sample 21 Signal 1 PR Interval	A-15
Figure A-44. Maximal Likelihood Filter Hypothesis for Sample 21 Signal 1	A-15
Figure A-45. ECG Sample 21 Signal 2 Heart Rate	A-16

Figure A-46. ECG Sample 21 Signal 2 QT Interval and QTc Interval.....	A-16
Figure A-47. ECG Sample 21 Signal 2 PR Interval	A-16
Figure A-48. Maximal Likelihood Filter Hypothesis for Sample 21 Signal 23	A-17
Figure A-49. ECG Sample 23 Signal 1 Heart Rate	A-17
Figure A-50. ECG Sample 23 Signal 1 QT Interval and QTc Interval.....	A-17
Figure A-51. ECG Sample 23 Signal 1 PR Interval	A-18
Figure A-52. Maximal Likelihood Filter Hypothesis for Sample 23 Signal 1	A-18
Figure A-53. ECG Sample 23 Signal 2 Heart Rate	A-18
Figure A-54. ECG Sample 23 Signal 2 QT Interval and QTc Interval.....	A-19
Figure A-55. ECG Sample 23 Signal 2 PR Interval	A-19
Figure A-56. Maximal Likelihood Filter Hypothesis for Sample 23 Signal 2	A-19
Figure A-57. ECG Sample 25 Signal 1 Heart Rate	A-20
Figure A-58. ECG Sample 25 Signal 1 QT Interval and QTc Interval.....	A-20
Figure A- 59. ECG Sample 25 Signal 1 PR Interval	A-20
Figure A-60. Maximal Likelihood Filter Hypothesis for Sample 25 Signal 1	A-21
Figure A-61. ECG Sample 25 Signal 2 Heart Rate	A-21
Figure A-62. ECG Sample 25 Signal 2 QT Interval and QTc Interval.....	A-21
Figure A-63. ECG Sample 25 Signal 2 PR Interval	A-22
Figure A-64. Maximal Likelihood Filter Hypothesis for Signal 25 Sample 2.....	A-22
Figure A-65. ECG Sample 27 Signal 1 Heart Rate	A-22
Figure A-66. ECG Sample 27 Signal 1 QT Interval and QTc Interval.....	A-23
Figure A-67. ECG Sample 27 Signal 1 PR Interval	A-23
Figure A-68. Maximal Likelihood Filter Hypothesis for Sample 27 Signal 1	A-23
Figure A-69. ECG Sample 27 Signal 2 Heart Rate	A-24
Figure A-70. ECG Sample 27 Signal 2 QT Interval and QTc Interval.....	A-24
Figure A-71. ECG Sample 27 Signal 2 PR Interval	A-24
Figure A-72. Maximal Likelihood Filter Hypothesis for Signal 27 Sample 2.....	A-25
Figure A-73. ECG Sample 39 Signal 1 Heart Rate	A-25
Figure A-74. ECG Sample 39Signal 1 QT Interval and QTc Interval.....	A-25
Figure A-75. ECG Sample 39 Signal 1 PR Interval	A-26

Figure A-76. Maximal Likelihood Filter Hypothesis for Sample 39 Signal 1	A-26
Figure A-77. ECG Sample 39 Signal 2 Heart Rate	A-26
Figure A-78. ECG Sample 39 Signal 2 QT Interval and QTc Interval.....	A-27
Figure A-79. ECG Sample 39 Signal 2 PR Interval	A-27
Figure A- 80. Maximal Likelihood Filter Hypothesis for Signal 39 Sample 2	A-27

List of Tables

Table 3-1. Hypothesis Model Parameters from Ten Sample Data Sets.....	3-9
Table 3-2. Hypothesis Filter Parameters	3-12
Table 3-3. Hypothesis σ^2 Tuning Values for Sample ECG Signals	3-19
Table 3-4. Initialization Hypothesis Filter Bank Parameters	3-22
Table 3-5. New Hypothesis Filter Bank Parameters.....	3-29
Table 3-6. Alternative Hypothesis Filter Bank Parameters, Bank 2.....	3-30
Table 3-7. Alternative Hypothesis Filter Bank Parameters, Bank 3.....	3-30
Table 4-1. MMAE ECG Processing Algorithm Scoring.....	4-3
Table 4-2. QT and PR Interval Accuracy for Accurately Detected R-wave	4-9
Table 4-3. ECG Sample Differences from Characteristic Waveform.....	4-16
Table 4-4. MMAE ECG Processing Score for Exsanguination Data	4-17
Table 5-1. Overall Algorithm Accuracy.....	5-3

Notation

Scalars, Vectors, Matrices

Scalars are denoted by upper or lower case letters in italic type, as in the scalar x .

Vectors are denoted by lower case letters in boldface type, as in the vector \mathbf{x} .

Matrices are denoted by upper case letters in boldface type, as in the matrix \mathbf{A} .

Subscripts

o -- Initial, as in initial conditions

d -- Discrete-Time

i,j -- Sampling Index Time

k -- Elemental Filter Index

u -- User GPS Receiver

Superscripts

$^{-1}$ -- Matrix Inverse

T -- Vector or Matrix Transpose

$^-$ -- Fourier Transform

Acronym List

Abbreviation

AFIT
AFRL
ANN
ANS
AV
BPM
C/A
COTS
DARPA
ECEP
ECG
EEG
EGG
EMG
EOG
FIR
GPS
GTWM
HE
HMM
JAMA
KF
L1
L2
MIT
MMAE
NASA
PC
PSD
PR
PSN
P(Y)
QT
RF
RR
SA
SNS
USAF
VO₂
WGN

Acronym

Air Force Institute of Technology
Air Force Research Lab
Artificial Neural Network
Autonomic Nervous System
Atrioventricular
Beats Per Minute
Course/Acquisition
Commercial Off-The-Shelf
Defense Advanced Products Research Agency
Earth-Centered, Earth-Fixed
Electrocardiogram
Electroencephalography
Electrogastrography
Electromyography
Electrooculography
Finite Impulse Response
Global Positioning System
Georgia Tech Wearable Motherboard™
Human Effectiveness
Hidden Markov Model
Journal of the American Medical Association
Kalman Filter
GPS Carrier Frequency, 1575.42 MHz
GPS Carrier Frequency, 1227.60 MHz
Massachusetts Institute of Technology
Multiple Model Adaptive Estimator
National Aeronautic Space Association
Personal Computer
Power Spectral Density
P-wave to R-wave
Parasympathetic Nervous System
Precision (Encrypted)
Q-wave to T-wave
Radio Frequency
R-wave to following R-wave
Sinoatrial
Sympathetic Nervous System
United States Air Force
Volume of Oxygen
White Gaussian Noise

Abstract

This thesis presents a novel electrocardiogram (ECG) processing algorithm design based on a Multiple Model Adaptive Estimator (MMAE) for a physiological monitoring system. Twenty ECG signals from the MIT ECG database were used to develop system models for the MMAE. The P-wave, QRS complex, and T-wave segments from the characteristic ECG waveform were used to develop hypothesis filter banks. The MMAE robustly locates these key temporal landmarks in the ECG signal, extracting crucial patient treatment information from the often distorted or unstable ECG waveform. By adding a threshold filter-switching algorithm to the conventional MMAE implementation, the device mimics the way a human analyzer searches the complex ECG signal for a useable temporal landmark and then branches out to find the other key wave components and their timing.

The twenty signals and an additional signal from an animal exsanguination experiment were then used to test the algorithm. Using a conditional hypothesis-testing algorithm, the MMAE correctly identified the ECG signal segments corresponding to the hypothesis models with a 96.8% accuracy-rate for the 11539 possible segments tested. The robust MMAE algorithm also detected any misalignments in the filter hypotheses and automatically restarted filters within the MMAE to synchronize the hypotheses with the incoming signal. Finally, the MMAE selects the optimal filter bank based on incoming ECG measurements. The algorithm also provides critical heart-related information such as heart rate, QT, and PR intervals from the ECG signal. This analyzer

could be easily added as a software update to the standard physiological monitors universally used in emergency vehicles and treatment facilities and potentially saving thousands of lives and reducing the pain and suffering of the injured.

A NOVEL ELECTROCARDIOGRAM SEGMENTATION ALGORITHM USING A MULTIPLE MODEL ADAPTIVE ESTIMATOR

1. Introduction

1.1 Background

Medical patient monitoring advances allow doctors to gain insight into complex body functions. With a few tests, types of blood gases and their levels, heart function parameters, lung function parameters, and brain parameters are easily obtained. During surgery, continuous monitoring of vital signs ensures that the patient is provided the best care possible, even in the most extreme conditions.

Conditions that tax the body exist outside the doctor's office. A firefighter inside a burning building undergoes extreme stress, as he must worry about not only putting out a fire or getting occupants to safety, but about ensuring that he is capable of performing his job as he was trained so as not to injure himself or his co-workers. Few know what reactions occur in the body when a firefighter experiences the adrenaline rush of standing in a burning building trying to put out a fire. Safety and job performance could be increased if a process to monitor and analyze a fire fighter's vital signs were available.

Vital sign monitoring could also increase efficiency and safety for many different professions and athletes. Athletes often monitor their training intensity based on their heart rate. For example, runners may cover a distance based on a coach's desired heart

rate range regardless of the pace required to maintain the heart rate. A coach would be interested in the runner's pace, how hills affected the runner, or if the extra "motivation" given during the run helped. Little has been done with correlating an athlete's position or speed to the physiological responses experienced by the athlete. New and more effective training routines could be constructed if the coach had the means to monitor the athletes' vital signs along with their position and velocity.

A squad in a combat operation can be selected for the most dangerous and critical missions. Information about the squad's position and physiological condition could give a commander and the medical staff the necessary situational awareness on the battlefield that is needed to win an engagement. The information delivered by these physiological monitors and seen by a commander will give immediate insight into whether a team member is down, how badly he is hurt, and if the situation warrants an immediate attempt at rescue.

There are portable systems designed for patient monitoring away from a doctor's office. There also exist the means to determine accurately a person's position on Earth. Small, lightweight Global Positioning System (GPS) receivers are can determine a person's position within approximately 10 meters rms. There are also many techniques to transmit data to a remote location, including wireless networks, cellular technology, satellite communications, or radio frequency (RF) transmission links. Thus, the components exist to provide a real-time remote physiological and position monitoring system. A paper describing the proposed system was presented at the Institute of Navigation (ION) GPS-2001 Conference in Salt Lake City, UT, and is placed in Appendix B.

1.2 Research Objectives

The purpose of this research is to lay the foundation for an outdoor physiological and position monitoring system. The system will combine physiological sensors and a GPS receiver into a comfortable garment that can transmit the position and physiological information (vital signs) to a remote monitoring or base station using an RF transceiver. The overall research endeavor also includes the design of base-station software capable of processing the transmitted data, providing real-time information concerning the team member's physiological status and position in a format that is easy to interpret. The software will provide warning indications to the monitor when a physiological parameter indicates danger or is outside of a desired range.

This research focuses on developing the software algorithms to extract information from an electrocardiogram (ECG), which may relate an event or a relationship between events in the ECG to the possibility of a dangerous physical condition. The heart's electrical activity not only contains information about how quickly the cardiac muscle is contracting and relaxing, but also contains information regarding the balance between the sympathetic and parasympathetic nervous systems. The sympathetic nervous system (SNS) generally increases heart rate, and the parasympathetic nervous system (PNS) decreases heart rate. Other relationships between the events in the ECG may be found during strenuous situations, including fires, law enforcement situations, combat, or injury.

1.3 Summary of Current Knowledge

A summary of the current knowledge in this research area focuses on answering the following question: Does the technology exist to develop a system capable of real-time physiological and location monitoring? The summary will first analyze current physiological monitoring techniques and options, then discuss real-time transmission techniques, review physical location determination in the context of team monitoring applications, and finally overview the physiological parameter software algorithm.

Extensive research at the Air Force Institute of Technology (AFIT) into motion sickness using electroencephalography (EEG) sets a precedent for physiological research at this institution [3, 50, 56, 63]. AFIT has worked with the Air Force Research Lab Human Effectiveness Directorate's (AFRL/HE) motion sickness research. AFRL/HE continues to study the effects of various levels of acceleration (g's) in a centrifuge while using various techniques trying to overcome physical difficulties when flying.

Several advances in medical technology allow doctors to monitor their patients' the physiological functions quickly and comfortably. Harrington [22] remarks that non-invasive monitoring has few complications compared to invasive monitoring techniques. Several alternatives to traditional blood pressure monitoring, blood oxygen level monitoring, and heart rate monitoring have been developed that are more comfortable than the invasive techniques.

Several efforts have been made to observe the body's physiological condition while a person is performing a task. For example, Nakra [46] observed the changes in heart rate, galvanic skin response, and muscle activity while a symphony conductor directs the musicians. She found a high correlation between the music intensity and the

conductor's physiological responses. Similarly, Dr. Steve Olvey, CART Racing Medical Director, researched a racecar driver's physiological state during the May 2001 Indy 500 [45]. Using a sensor system called LifeShirt®, Dr. Olvey concluded that drivers are under extreme stress during the entire race and that race crews may be able to alert a driver to a diminished physiological or mental state, thus increasing driver safety.

Many options exist to transmit data in real-time. These options range from using satellite communication technology, to the Internet, to RF transmission. The *Journal of the American Medical Association* reported that vital signs of an experiment subject were transmitted using an airplane cellular telephone system [55]. The data was then uploaded to the Internet for worldwide distribution to monitoring officials with the proper authorization credentials. Expedition members climbing Mount Everest used an RF transmission link, as well. Repeaters were used to “bounce” the signal from mountain to mountain since the RF transmission technology used was line-of-sight only. The data was received at the base station and then uploaded to the Internet [53]. Such a complex and potentially expensive system need not be used to achieve accurate transmission. A runner's training evaluation system used a 900MHz spread-spectrum transceiver to send data in real-time [42]. If an RF system is used, care must be taken when choosing the frequency band. One must consider the system implementation environment and choose a frequency that works well in that situation. The Georgia-Tech Wearable Motherboard has been tested in indoor applications using an RF link. A different frequency design allows this system to achieve a 100-foot range, whereas other systems would not work as well in an indoor environment [14].

Physical location can be determined very precisely using GPS. GPS, however, does not work in indoor applications because the signal power used is very low. GPS is a radio navigation system currently utilizing 28 satellites. The system operates at carrier frequencies of 1575.42 MHz (L1) and 1227.60 MHz (L2). Using spread-spectrum technology, a Course/Acquisition (C/A) signal at a chipping rate of 1.023 MHz and a Precision (Encrypted) [P(Y)] code at a chipping rate of 10.23MHz are modulated on the L1 signal. The L2 frequency only carries the P(Y) code [44]. A system accuracy of 10 meters rms is a reasonable expectation of an outdoor user.

Several systems have utilized GPS and have had promising results. For example, Miller [42] was able to correlate position and velocity data during cross-country training with heart rate data. The GPS data was processed on the coach's laptop computer. Using this new training aid, the coach tailored the training program to the specific runner. The Mount Everest Expedition members also had GPS receivers. This data allowed the base station monitors to locate each member accurately. Mountain climbers are concerned about getting lost in a storm or not being able to receive help if injured because the rescue personnel do not know the person's precise location [53].

Another important area that has not been discussed thus far is the software used to process and display the data. Several software packages have been used in previous work, including Microsoft Access [53] and LabView [42]. The software used in a system display seems to be more dependent on designer preference or experience than on the advantages or disadvantages of one package versus another package.

In contrast, the special warning software requires a more precise approach. This research focuses on the ECG waveform and extracts information in the ECG signal to

find a correlation with a physically dangerous situation. The ECG signal varies greatly from person to person and varies as heart rate increases and decreases. The signal's amplitude, the fundamental frequencies in the waveform, and the timing of the waveform all can change with time. While the signal is "pseudo-periodic" [54] it can be treated as a random signal. Thus, with the uncertainties in the specific waveform parameters, the multiple filter estimation bank lends itself very well to solving this problem. A multiple model adaptive estimator (MMAE) based on the Kalman filter allows for various hypothesized system models and uses a conditional probability calculation to determine which hypothesized model best represents the true system model given the measurement history of the true system model. The MMAE then functions as a parameter estimation algorithm to estimate the various parameters in the true system. The MMAE has been used significantly in the guidance, navigation, and control areas to identify and redistribute controls in an aircraft with failed sensors or failed control surfaces with great success [2, 21, 37, 38]. Thus, the technology to develop a real-time position and physiological monitoring system exists and has been demonstrated in various forms.

1.4 Scope

The goal in the overall research is to develop a real-time positioning and physiological monitoring system. However, this research will focus solely on an ECG processing algorithm. In addition, the associated results will be analyzed and compared to industry-accepted solutions. Advanced software algorithms will be developed to warn the monitor of dangerous or abnormal physiological parameter. The advanced software will be an MMAE that will extract critical information from the ECG signal, including

determining the exact time of the R-wave peak (to be discussed in Section 3.7) and the heart rate. This software will provide the means to correlate events or the relationships among events in the ECG signal with person's activities in a strenuous environment.

1.5 Approach/Methodology

The multiple model adaptive estimator (MMAE) only performs as well as the models upon which it is based. When a model does not fully characterize the true system, the performance of the MMAE is suboptimal. Models of the true system will be built on the segments of the ECG signal. Thus, a firm understanding regarding the parameters in the ECG signal must first occur. Insight into how the ECG signal propagates, its dynamics in time, the frequencies contained in various signal segments, and the signal strength may all help develop a proper system model describing the various signal segments.

1.5.1. Analysis of ECG parameters

The ECG signal will first be divided into its various segments relating to the electrical signal conduction through the heart. The signal segments' first and second derivatives can then be found. An estimate of the signal segment's autocorrelation function and the derivatives thereof gives insight into how the signal changes in time and the amplitudes of the signal segments. Similarly, the Fourier transform of the autocorrelation estimate shows the frequencies and an estimate of the power contained in the signal segments. Initially, the assumption will be made that the ECG signal is similar to a normal signal: it contains no abnormalities indicative of a health problem. This

assumption gives the model the necessary knowledge to determine the sequence that the segments follow and may give the model another parameter that can make it more accurately represent the true system.

1.5.2. Development of ECG System Models for the MMAE

Once knowledge and understanding pertaining to the ECG signal's properties are grasped, the system models for the MMAE can be developed. The system model in state-space form relies on the time-domain mathematical relationships of the system states. The system states used in the model depend on the measurements available and the desired information. The only measurement available is the ECG signal itself, and the state of interest is the ECG signal segment. Thus, the system model needs at least one state but will most likely require more to model the true system accurately. Note that the goal is not to estimate the signal; the measured signal contains the information of interest. Because the goal is to estimate the ECG signal events and the relationships between the events automatically, the event models should be distinct from one another to aid the MMAE algorithm (to be discussed in Section 3.3.3). This distinction can come from the expected signal strengths, the expected operational frequencies, or other parameters in the models.

1.5.3. ECG Processing Software Testing and Validation

Testing and validation of the ECG processing software will use digitized ECG signals from the MIT ECG database [13]. This database was created to provide a worldwide-accessible set of ECG signals for ECG algorithm testing and validation. The

database contains signals from healthy humans, as well as signals that contain various irregularities called arrhythmias. Some signals contain annotations from a doctor who reads the ECG. This provides a means to test and validate the ECG processing software against a trained medical doctor. The algorithm will be tested against a variety of signals to ascertain whether or not it is robust in its processing capabilities and to what extent it can handle difficult signals. The algorithm will also be tested to determine if the heart rate calculation and determination of the exact P-wave, R-wave, and T-wave peaks are accurate (as shown in Section 4.2). Data from research involving monitoring an animal's changing physiological parameters during exsanguination will also be tested in the algorithm. Significant challenges exist in this data set, including a changing heart rate, varying waveforms, and decreased signal power as the animal is exsanguinated.

1.6 Thesis Overview

Chapter 2 presents theory behind physiological monitoring in general, various sensor technologies, previous physiological monitoring research and applications, GPS theory, Kalman filtering, and MMAE theory. Chapter 3 describes the development of the MMAE used in this research, various techniques for analyzing ECG signals including time and frequency domain techniques and the digital signal processing algorithms used, and the hypothesized ECG system model development. Chapter 4 presents the ECG processing algorithm results when signals from the MIT ECG database and the animal exsanguination are processed. Chapter 5 summarizes the research effort and offers suggestions for further research.

1.7 Summary

This chapter provided an overview of the plan of attack for designing, building, testing, and evaluating the software for a real-time remote positioning and physiological monitoring system. An overview of previous research was presented, including the theory pertaining to physiological sensors, GPS, Kalman filtering, and previous applications. Chapter 2 will further develop the theory behind the technologies associated with the monitoring system.

2. Current Knowledge

2.1 Introduction

Research into remote patient monitoring has recently been undertaken in the medical community. While doctors have monitored their patients closely since medicine's beginning, not until recent advances in communications, computers, and physiological sensors have doctors had the ability to monitor patient status from another room. With the advent of such technologies as the Internet, cellular communications, and broadband wireless technology, it is now possible to transmit vast amounts of data at incredible speeds. Other technical advances in computer technology, speed and size, and advances in noninvasive physiological sensors allow accurate patient monitoring in a variety of physical activities. While the medical community is eager to make advances in patient monitoring, reduce cost, and improve patient safety and quality of care, very little has been done in the way of remote monitoring.

Remote monitoring has applications for the public in addition to health care patients. For example, do coaches really know exactly how the body responds to exercise? Does the fire chief know exactly when, where, and why a fire fighters died or if the death could have been prevented? Does the racecar driver understand the extreme stress on the body during a race? Or more importantly, what happened right before the crash? Most people can only speculate at the answers to these questions.

A new and exciting research area follows: can a non-invasive physiological monitoring unit be combined with Global Positioning System (GPS) navigation information to provide more information to doctors, coaches, or other personnel

monitors? Non-invasive physiological monitoring, GPS, and communication technology, if linked, would provide physiological information that could have tremendous impact on personnel safety, training, and work in stressful environments. While there is little research directly correlating physiological data with personnel navigation information, general research in the areas of non-invasive physiological monitoring or remote monitoring will yield a strong foundation to answer the question of interest. A summary of current knowledge focuses on four distinct areas: non-invasive monitoring (including the physiological parameters in this research, the electrocardiogram), parameter estimation and system identification algorithms (the major focus in this research), GPS technology, and communication technology.

2.2 *Physiological Health Research*

Physiological health research requires the ability to monitor a subject's physiological parameters accurately in several different environments besides the doctor's office or hospital. The following sensors are typically required for accurate physiological health estimation: electrocardiogram (ECG), respiration rate, pulse oxygen saturation, and skin temperature. Additionally, depending on the environment and activity, other sensors such as electroencephalography (EEG) and environmental CO₂ sensors may be required to give a high quality physiological indication of a person's performance and health.

2.2.1. Physiological Sensor Information

Advances in non-invasive physiological monitoring technology have allowed the replacement of invasive monitoring equipment and yielded several key benefits. In one of the few articles detailing the various alternatives to invasive monitoring, Harrington [22] points out that non-invasive monitoring has none of the complications associated with invasive monitoring. He goes on to explain that several complications can result from invasive arterial blood pressure monitoring. The most serious complication is nerve damage and infection to the areas surrounding the monitoring site. Finally, the risk of complication increases significantly when the duration monitoring exceeds 96 hours. Several viable non-invasive techniques are now available. One non-invasive application is the Dinamap, or “Device for Noninvasive Mean Arterial Pressure.” This is the standard blood pressure cuff used in most doctors’ offices today. However, inaccuracies may occur due to improper cuff placement and excessive cuff movement. Photoplethysmography, a technique in which specific wavelengths of light are beamed into the body and blood pressure determined by the amount of light returned to a sensor, works well in physiologically stressful situations. Several studies indicate that the pressure cuff around a finger is as accurate as the Dinamap. Thus, several authors have concluded that non-invasive blood pressure monitoring can replace invasive techniques in most situations.

2.2.1.1 Respiration Monitoring

Harrington [22] also compares the techniques for respiratory monitoring. The standard invasive technique for respiratory monitoring is blood gas determination. The

main drawback with this technique stems from using an arterial catheter. Several non-invasive techniques are available, including pulse oximetry, transcutaneous oxygen, and strain gauges. Pulse oximetry uses two wavelengths of light: 940nm (infra-red light) and 660nm (red light). As shown in Figure 2-1, oxygen rich hemoglobin responds to a 940 nm wavelength of light and oxygen-depleted hemoglobin responds to a 660 nm wavelength of light [66]. An algorithm determines the oxyhemoglobin and deoxyhemoglobin ratio based on their relative absorbance at the two wavelengths.

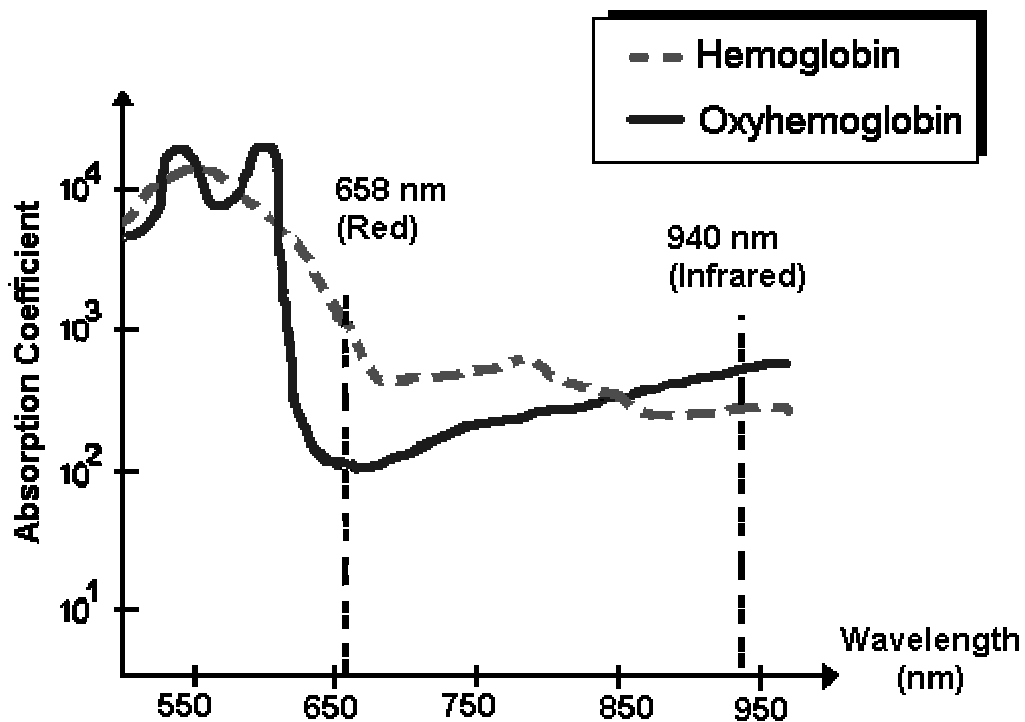


Figure 2-1. Absorption Coefficients for Hemoglobin and Oxyhemoglobin Relative to Light Wavelength (nm).

Additionally, the amount of light absorbed is proportional to the blood volume under the sensor area, as shown in Figure 2-2. For each heartbeat, the volume of pumped

blood increases when the heart contracts and then decreases when the heart relaxes. The pulse oximeter is typically placed on a toe, finger, or earlobe as shown in Figure 2-3.

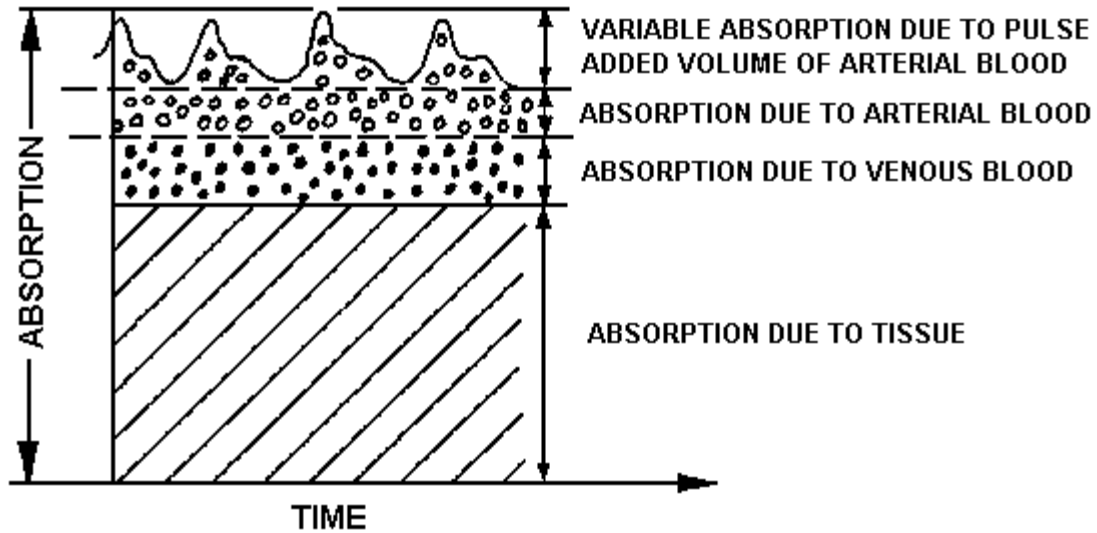


Figure 2-2. Absorption as Light Passes Through the Body [24].

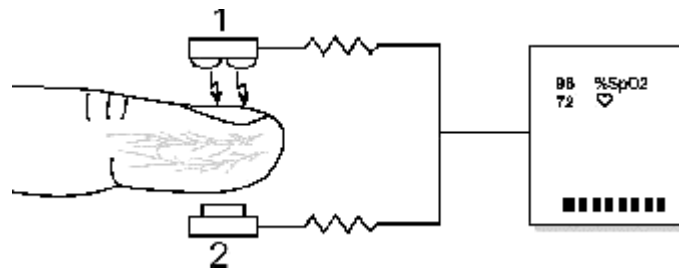


Figure 2-3. Typical Pulse Oximeter Placement [19].

The pulse oximeter bases its measurement on the amount of light absorbed as it passes through the body. Because the blood volume and the amount of oxygen in the blood change in time, the heart rate and the oxygen level can be derived based on the light intensity measurements.

Thus, pulse oximetry gives indications of blood oxygen content and heart rate. The heart rate from the pulse oxygen sensor can serve as a crosscheck for the ECG heart rate. While the respiration sensor will give indications as to how fast and how deeply a person is breathing, the oxygen content of the blood will relate the respiration rate to how well the lungs are functioning. However, pulse oximetry cannot distinguish between the types of gases in the blood. The saturation level includes oxyhemoglobin, carboxyhemoglobin, and methemoglobin. While this drawback may not impact the of the sensor's accuracy in most applications, certain environments such as a fire may give overly optimistic blood oxygen level readings [22].

While pulse oximetry works well in benign environments such as hospitals, evaluation of the sensor's accuracy while a subject is moving is critical for dangerous and dynamic operation in the real world. An extensive study with the pulse oximetry sensor attached to three different locations on an athlete's body (left ear lobe, right ear lobe, index finger) was conducted to compare the pulse oximetry sensor outputs against blood gas levels [33]. The athletes exercised at five different intensity levels based on the maximum volume of oxygen ($\max \text{VO}_2$) consumed by the body ($\max \text{VO}_2$) ($\leq 20\% \max \text{VO}_2$, $21-40\% \max \text{VO}_2$, $41-60\% \max \text{VO}_2$, $61-80\% \max \text{VO}_2$, and $\geq 81\% \max \text{VO}_2$). The authors showed that the pulse oximetry sensor estimated oxyhemoglobin to within $0.01\% \pm 1.4\%$ (mean $\pm 1\sigma$) and concluded that it gave an accurate oxyhemoglobin measurement during exercise. Powers et al. [49] also investigated the accuracy of pulse oximetry on healthy subjects during exercise, and again concluded that pulse oximetry accurately measures oxyhemoglobin levels. However, tests conducted on a group of smokers showed that the pulse oximetry sensor gave optimistically high results compared

to the blood gas levels because of the high carboxyhemoglobin levels. Thus, extending this research to include people working in environments where CO levels may be high requires other sensors such as those that measure environment CO₂ or CO. Other drawbacks to the pulse oximeter are motion artifacts in the output waveform that can cause erroneous results in the heart rate due to the sensor changing measurement position or forces from movement or gravity.

A transcutaneous oxygen monitor is not used as often as pulse oximetry because the increased skin thickness in adults causes less reliable readings. However, these sensors are used in the intensive care unit and during surgery with great success. The main drawback is that the electrodes must be moved every four to six hours to prevent burns [22].

Respiration monitoring also occurs by measuring the increase and decrease in midsection size with a strain gauge. The respiration sensor provides respiration rate and an insight into breathing quality. Two sensor locations are generally acceptable -- on the chest and on the abdomen. One may wish to use both locations to understand an individual's breathing pattern better. Generally, one will see an increase in chest breathing when a person is excited, experiencing the effects of an aroused sympathetic nervous system. Oppositely, one will see abdominal breathing dominate chest breathing when a person relaxes [58].

2.2.1.2 *Electrocardiogram*

An electrocardiogram (ECG) measures the heart's electrical activity. The ECG signal shows the voltage in the heart muscle as it contracts and relaxes, as measured from

a spot on the body (different positions for the ECG leads will show different voltage levels). Figure 2-4 shows an ECG signal and the signal components. In a normal, healthy human, the signal starts at the sinoatrial (SA) node at the top of the heart, triggering the atria, which contract and relax (P-wave). The signal slows significantly at the atrioventricular (AV) node, allowing the ventricles to fill. The signal travels down the right and left bundle branch triggering the ventricle which then contracts (QRS) and relaxes (T), (U). The heart is then relaxed until the next “heart beat” starting with the P-wave. Figure 2-4 shows the characteristic waveform with the corresponding heart activity. The shaded areas in the diagram represent the electrical signal traveling through the heart.

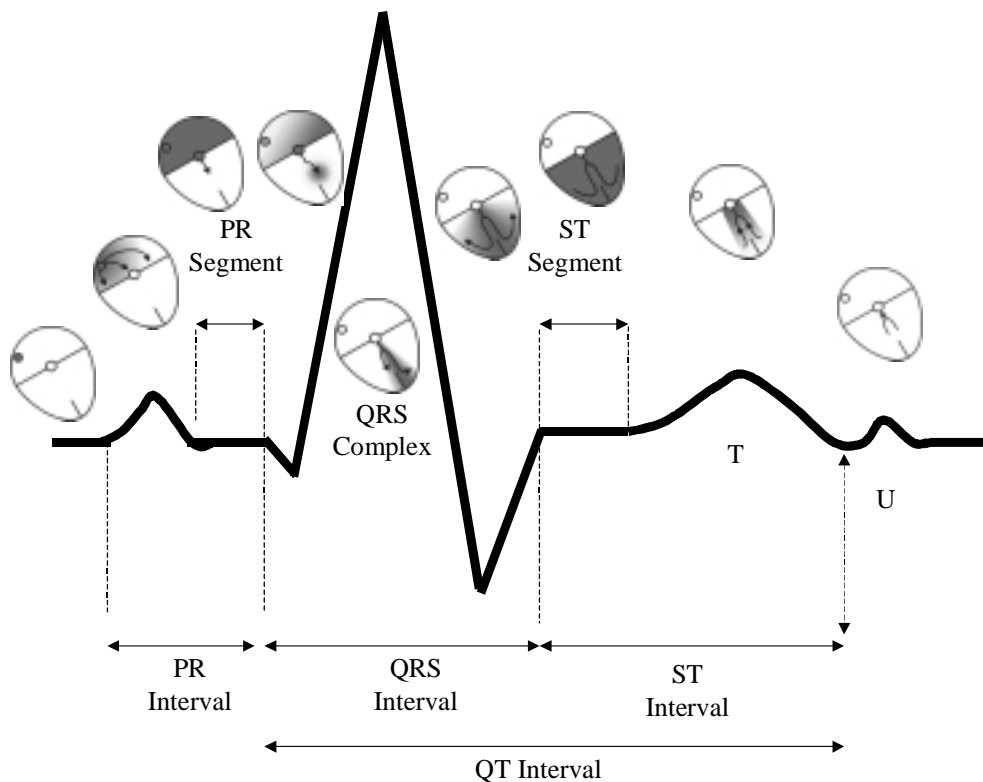


Figure 2-4. ECG Characteristic Waveform Corresponding to Heart Activity [29], [10].

A summary describing the characteristic ECG waveform and the corresponding heart activity [10]:

P-wave

SA node depolarization and atrial contraction

QRS Complex

Ventricular depolarization and contraction

T-wave

Ventricular repolarization

U-wave

Represents the final stage of ventricular repolarization

The ECG waveform should follow the standard “P, Q, R, S, T, U” distinct electrical events in the heart [58]. The signal obtained during an ECG recording depends on several facts:

1. The location of the leads
2. How well the leads are placed on the skin
3. The quality of the signal amplifiers
4. The amount of measurement noise.

The three limb leads denoted Lead I, Lead II, and Lead III are shown in Figure 2-5 and are called the Einthoven’s Triangle. Additionally, six leads, denoted V1-V6, may be placed around the heart, each measuring a different heart axis. These leads provide a more precise electrical measurement and help localize medical conditions. Note that not all leads measure the events creating the characteristic ECG waveform, thus making lead selection critical when events of interest want to be analyzed.

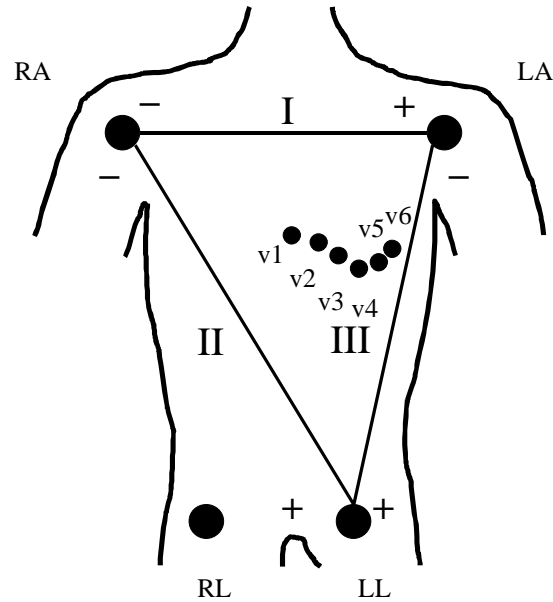


Figure 2-5. Einthoven's Triangle of ECG Electrode Placement [27]

An ECG system may use as many as 15 leads. However, three leads are the minimal number needed because one lead serves as a reference and the two other leads are differenced. The three electrodes are located on the left arm, right arm, and right leg, with lead I being the difference between the left arm and right arm, lead II the difference between the right arm and the left leg, and lead III the difference between the left arm and the left leg. Note that the leads can be placed on the chest and the midsection rather than the extremities. The voltage measurement amplitudes increase as the electrodes are placed closer to the heart.

The time between “R” events follows a periodic oscillation known as the sinus arrhythmia. The resting RR interval is not constant; generally, it has a Gaussian distribution about some mean rate. This “heart rate variability” occurs when the heart rate changes as a person inhales and exhales. Doctors speculate that when a person goes into shock, the Gaussian distribution of the heart rate becomes essentially a delta

function, meaning the heart rate's standard deviation becomes very small [26]. Such an insight into the problems occurring in the body may not come from any other sensors, especially when time is critical, such as in a hospital emergency room. A Fast Fourier Transform can show the heart rate oscillation and can indicate a dangerous physiological parameters if the normal sinus arrhythmia is not present [58].

Other heart rate variability models try to couple the autonomic nervous system with events in the heart. The autonomic nervous system (ANS) regulates key functions in the body including the heart, smooth muscles, and glands. The ANS is made up of the parasympathetic nervous system (PNS) and the sympathetic nervous systems (SNS). The PNS slows heart rate and increases intestinal and gland activity, while the SNS increases heart rate, constricts blood vessels, and increases blood pressure. It has been noted that the balance, or lack thereof, between the sympathetic and parasympathetic systems is related to heart rate variability [6].

The relationships between segments of the ECG signal provide significant information as to what events and activities occur in the body. For example, the PR interval decreases as the RR interval decreases (due to an increase in heart rate); however, in a person with a problem with the autonomic nervous system, the PR interval may not properly decrease as the RR interval decreases [12]. Additionally, the relationship between the QT interval and the RR interval has been shown to not change linearly as the RR interval decreases. The measurement of the QT and RR intervals during exercise may help identify people with Coronary Artery Disease [5].

Modeling each ECG segment can be accomplished using several different mathematical tools. Dynamic time warping [64], artificial neural networks [60], hidden

Markov models [57, 30], and the wavelet transform [51] all have been used in automated ECG processing in the past. Dynamic time warping is a dynamic programming algorithm that has been applied to speech recognition. It requires two signal parameters: the features and the distance between the features. A dynamic programming algorithm finds the lowest distance measure between the input feature and a template feature.

Hidden Markov models are also used for recognition algorithms, including speech and handwriting recognition. Hidden Markov models consist of three things: states, probabilities of transitions between states, and probabilities of a particular observation while in a particular state. The Markov nature of the model lies in the fact that the probability of the observation or transition depends only on the particular state and not on the state history. If the probabilities do depend on previous states, the model can then be described as Markov-n, where n is the number of states the probability calculations requires. The states themselves are hidden to the outside viewer who only sees the state outcomes or observations, thus the “hidden” name.

Artificial neural networks (ANN's) are loosely modeled on the activities in the brain. A complex function is broken up into several simpler functions, each with a connection; see Figure 2-6. The connection is controlled by a number that represents the connection's strength. The strengths are then modified to generate the appropriate output. The power of ANN's is the interconnections that share the processing task. Very simple functions can be combined and compared to the expected result, with the error driving a change in the connection strengths.

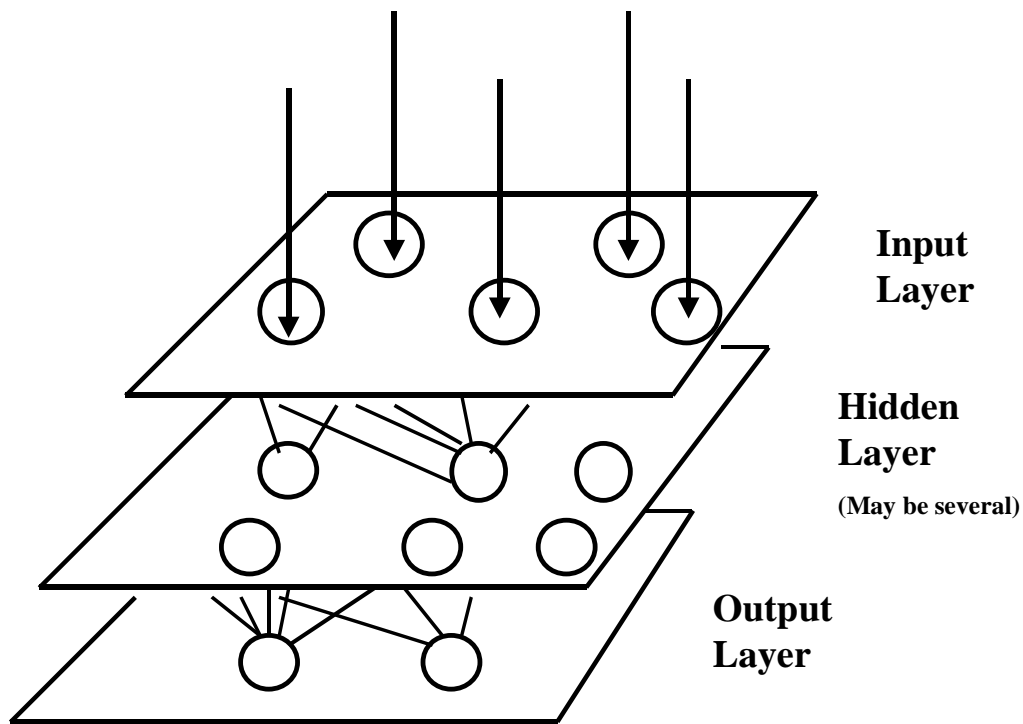


Figure 2-6. Diagram of Artificial Neural Network [28].

Note the high degree of interconnections in Figure 2-6. Adaptively changing the connection strength allows the ANN to “learn” in a similar fashion as a human learns. This algorithm works especially well in tasks that require parallel computations.

The Wavelet Transform is a mathematical algorithm to view both a signal’s time domain and frequency domain components at the same time, with a tradeoff between resolution in one domain for resolution in the other. All transforms use a set of basis vectors to describe waveforms in different domains. The transform is applied to a signal to obtain information from the signal that is not apparent in the raw signal. The Fourier transform uses the orthogonal basis set of sines and cosines; however, the Wavelet

transform can use other specially designed basis sets. The original signal can then be written as a series expansion of the basis vectors [7].

This research proposes the use of a multiple model adaptive estimator (MMAE). A multiple model filter bank has been used extensively in guidance, navigation, and control applications to detect parameter changes in the system in addition to its many other applications [9, 16, 18, 34, 35, 36, 41, 52, 65]. Willsky reported great success in arrhythmia detection and classification in electrocardiograms using both a multiple hypothesis model and the generalized likelihood ratio (GLR) [17, 67]. These systems, however, already had the different ECG segments decomposed from the ECG signal; they merely analyzed and identified changes in the relationships among the segments. This research, however, uses the MMAE as the basis for the ECG segmentation algorithm.

2.2.2. Physiological Monitoring Outside a Doctor's Office

Harrington [22] also analyzed several other areas of non-invasive monitoring. While not specific to his research effort, he showed that the medical community accepted non-invasive monitors as a reliable alternative to traditional invasive monitors. The authors remarked, “Non-invasive monitors provide the potential to observe a variety of physiologic processes on a continuous basis and allow for intervention prior to significant decompensation”[22]. Yet, doctors know very little about a patient’s vital signs when they are not in the office or hospital. Therefore, significant advances in patient monitoring and patient care can stem from the increased use of non-invasive monitors.

The use of non-invasive monitors is also motivated in others areas, not just for care in a doctor's office. With the enormous increase in telecommunication capability in recent years, "wireless" or more appropriately "officeless" patient care may allow virtual monitoring and treatment. A doctor can monitor a patient's health throughout the day, not just for a few minutes in the office.

In 1998, the *Journal of the American Medical Association* reported the first patient monitoring trial (experiment) while onboard an airplane [55]. Using the Boeing 767's cellular telephone system; electrocardiograph signals (ECG), blood pressure, respiratory rate, pulse rate, blood oxygen saturation from a pulse oximeter sensor, and body temperature were transmitted to a base station along with real-time video of the "patient." The base station received the signal and uploaded it to the Internet. Doctors around the world read and analyzed the signals, correctly identifying the medical condition. The study reported that the advantage of using the Internet to transmit the data resides in the ability to transmit medical data to any hospital close to where the plane might land during a real emergency. Thus, the hospital has the data required to treat the patient appropriately. Other advantages of in-flight monitoring include improved in-flight care, better preparation by teams meeting the patient on the ground, and possibly the ability to negate an emergency landing, which is expensive to airlines and an inconvenience to other passengers. While this proof of concept study was successful, among the several drawbacks to this system include the monitoring equipment's size and cost. The monitoring equipment, computer, and phone took up a row in an airplane and the cost was estimated at \$10,000.

The idea of non-invasive monitoring can also be applied in other areas. The National Aeronautic Space Association (NASA) is very interested in the causes of motion sickness. Using non-invasive physiological monitoring, NASA has developed a biofeedback system that will train people to gain control of their physiological responses [47]. The system is much more compact than the system used onboard the Boeing 767 described above, using sensors attached to a shirt, a belt mounted recording device, and a wrist display unit. The system can measure ECG, electromyography (EMG) (electrical activity of muscles) of leg and arm muscles, electroencephalography (EEG) (electrical activity of the brain), electrooculography (EOG) (electrical activity of the eyes), electrogastrography (EGG) (electrical activity of the intestine), skin temperature, blood volume pulse, blood pressure, and skin conductance levels. In addition, tri-axial accelerometers are used to give the head's position. The data recorder also includes electronic circuitry to process the data, batteries, and computer connections. The researchers looked for a relationship between motion sickness and the parasympathetic and sympathetic nervous systems activities.

Relating physiological parameters to a person's work is also of interest. Nakra [46] created the Conductor's Jacket to measure a symphony conductor's physiological parameters and gestures during a performance. Essentially, this system was a tuxedo jacket with interwoven physiological sensors. The system provided 16 different parameters for real-time analysis using a personal computer. The physiological parameters included respiration rate, heart rate, galvanic skin response (GVR), and muscle activity. Analysis of the conductor's physiological responses and the music

revealed strong correlation between the conductor's gestures, physiological responses, and tendencies with the music dynamics [46].

The Indy Racing League (IRL) is interested in using physiological monitoring to increase the safety of its drivers. Using the LifeShirt® by Vivometrics [45], an Indy car driver was monitored during the world famous 2001 Indy 500 race. Dr. Steve Olvey, the CART Racing Medical Director, suggests that knowing the driver's physiological parameters during a race will help crews increase the safety of the driver and will allow medical teams to understand an injury's severity immediately after a crash. Understanding how the body responds to the stress of a race can also lead to better training regimens [45].

Wearable sensor systems are also being developed by other agencies. The Defense Advanced Projects Research Agency (DARPA) recently sponsored an initiative to develop a system that will enable the Medical Corps to perform "virtual triage" [14]. Named the Georgia Tech Wearable Motherboard™ (GTWM), the creators suggest that for the first time there is a systematic way to monitor vital signs unobtrusively. In addition to physiological sensors, plastic fiber optic cords are woven into the shirt allowing the shirt to sense "projectile penetration." While the shirt was originally developed to minimize loss of life on the battlefield and to assist triage procedures, it also lends itself well to civilian healthcare scenarios. Much as the dental community has shifted its focus to preventative care, the GTWM could focus other health care communities from "treatment to prevention through wellness." Taking a virtual reality approach to health care, the GTWM could improve the quality of care while reducing costs through the added capabilities given to doctors to perform preventative medicine.

The GTWM uses a flexible wiring bus to connect the sensors. It also incorporates the DARPA personnel status monitor (PSM) type of sensor connectors [14], enabling the shirt to include previously developed non-invasive sensor technology. While the shirt sounds intriguing, only respiration, ECG, and projectile monitoring have been tested. The shirt has a capability to use other sensors such as environmental carbon dioxide (CO₂) sensors, useful in fire-fighting applications, voice monitors, and other physiological sensors. The shirt has the potential for use in several other applications due to its configurable and tailored design. These applications include sports or performance specialties, fire fighter or law enforcement, specialized health care including telemedicine, and aircrew monitoring [14].

Other areas of interest are physiological responses to exercise, including the relationship between perceived work and performance. Athletic heart rate monitors available today provide an athlete an accurate heart rate measurement. However, prior to 2000, a system did not exist that could correlate heart rate to the athlete's position and velocity. For example, if a runner's heart rate increased rapidly over a 30 second interval, did the increase occur because he ran up a hill or increased his pace? Miller [42] developed a novel system using a small, lightweight, low-cost GPS receiver in conjunction with a heart rate monitor to collect both types of data simultaneously. By using position, velocity, and heart rate information as another training tool in a coach's "tool box," racers should be able to increase their performance. Using evaluation software on a personal computer (PC), the GPS and heart rate data were displayed in graph form, showing heart rate, position, and instantaneous velocity. The data was transmitted in real time through a spread spectrum transceiver so that real-time

monitoring could occur. Using an OEM GPS receiver card, batteries, a microcontroller, a 900 MHz transceiver system, and real-time software, a coach can monitor the athletes training during workouts and competition [42].

Finally, real time monitoring in perhaps the harshest of conditions was accomplished in 1999. Dr. Richard Satava at Yale University used a vital signs monitoring system (VSM) including ECG, heart rate and skin temperature sensors, a GPS receiver, and a transceiver, to monitor climbers on Mount Everest from a base station [53]. FitSense Technologies designed the system which can be custom configured for other applications. Using radio frequency (RF) transmission, each of the sensors was connected to a data hub where the data was time stamped using GPS time. The VSM can monitor up to 16 people, each equipped with up to 16 sensors. Running for 10 days on two AA batteries, the system collected data every 15 seconds and transmitted data every 5 minutes, although the transmission rate was adjustable. The system used a serial port to connect to a personal computer or Palm Pilot. From the base station, data was transmitted using a TCP/IP satellite connection and then put onto the Internet. Data was then displayed on a graphical user interface (GUI), which gave doctors the ability to monitor any climber they desired. The authors remarked that numerous applications of the VSM such as hospitals, nursing homes, and space travel were possible, given that the VSM worked so well in extreme environments. Additionally, with more non-invasive sensors added to the system, doctors will gain a better understanding of the human body and the complex physiological activities that occur within it.

2.3 Importance of GPS

GPS provides an additional advantage previously not attainable when monitoring patients. An individual's position and velocity anywhere on the Earth can now be determined very precisely with a GPS receiver. Using GPS, correlations between an individual's physiological "events," position, and velocity have the potential to provide new insights into the body's physiological response at a given instant in time and a given location. This correlation will lead to new training methods for athletes, increased job safety in dangerous working environments, increased information for commanders of military forces, law enforcement, or public safety personnel.

The next several paragraphs provide a brief overview of GPS. For a more detailed explanation, see [44]. GPS is a space based radio navigation system with three main segments: the space segment, the control segment, and the user segment. The GPS space segment currently uses a constellation of 31 satellites in a medium earth orbit of 10,900 nautical miles (26,560 km) or 20,200 km above the earth. 24 satellites are required for full operational capability.

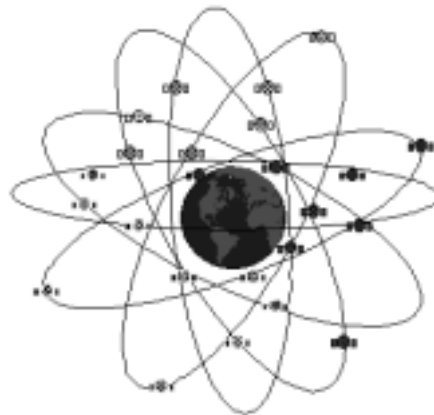


Figure 2-7. GPS Constellation

Each satellite in the constellation transmits two different codes: the coarse/acquisition code (C/A) and the precision (encrypted) [P(Y)] code. The C/A code is modulated on a 1575.42 MHz carrier frequency (L1) and the P(Y) code is modulated on the 1575.42 MHz carrier and a 1227.60 MHz carrier frequency (L2). A transmitted ephemeris message includes satellite clock correction parameters, satellite position and velocity parameters, and an almanac for all satellites [44]. The transmitted signal also identifies the satellite through its Pseudorandom Code Number (PRN) and functions as the ranging signal.

The control segment monitors the GPS satellite positions and updates the ephemeris message with correction parameters. The control segment consists of a master control station, five reference stations, and three data uploading stations. The reference stations collect the signals from the satellites and pass them on to the master control station where the ephemerides are recomputed. The new ephemerides and timing corrections for the satellite clocks are transmitted to the satellites.

The user segment consists of all of the equipment used to track and receive a GPS signal. A GPS receiver has five basic functions:

1. Receive RF signals from each visible satellite
2. Separate the signals from each satellite
3. Determine signal transmit time and Doppler shift
4. Decode navigation message to determine satellite position
5. Estimate user position, velocity, and time.

When the receiver is first turned on, it must search through all of the possible satellites and determine which satellites are visible. Once all of the satellites in view are acquired

and locked, the receiver can begin to estimate position, velocity, and time through its data processing algorithm [44].

2.4 Kalman Filter

A mathematical model describing the ECG signal has been attempted many times in the past [54]. Most of these models were not robust in their ability to model changes in the ECG waveform, whether from the same person or from different people. The ECG signal contains many uncertain parameters stemming from the signal's variability, as discussed in the background information in Section 2.2.1. Given these uncertain parameters, a Bayesian approach to parameter identification is possible using a multiple model adaptive filtering algorithm based on a bank of Kalman filters. The remainder of the section will present the theory behind a Kalman filter [39].

The general linear Kalman filtering algorithm is based on:

$$d\mathbf{x}(t) = \mathbf{F}(t)\mathbf{x}(t)dt + \mathbf{B}(t)\mathbf{u}(t)dt + \mathbf{G}(t)d\boldsymbol{\beta}, \quad (2.1)$$

where

- $\mathbf{x}(t)$ = the Kalman filter model state vector,
- $\mathbf{F}(t)$ = the Kalman filter state dynamics matrix,
- $\mathbf{B}(t)$ = the Kalman filter model control input matrix,
- $\mathbf{u}(t)$ = the system input vector,
- $\mathbf{G}(t)$ = the Kalman filter model noise input matrix,
- $\boldsymbol{\beta}$ = Brownian motion with statistics

$$E\{\boldsymbol{\beta}(t)\} = \mathbf{0}$$

$$E\{[\boldsymbol{\beta}(t) - \boldsymbol{\beta}(t')][\boldsymbol{\beta}(t) - \boldsymbol{\beta}(t')]^T\} = \int_{t'}^t \mathbf{Q}(\tau) d\tau \quad (2.2)$$

where $\mathbf{Q}(t)$ is a symmetric and positive semidefinite matrix.

This can also be written heuristically as:

$$\dot{\mathbf{x}}(t) = \mathbf{F}(t)\mathbf{x}(t) + \mathbf{B}(t)\mathbf{u}(t) + \mathbf{G}(t)\mathbf{w}(t) \quad (2.3)$$

where \mathbf{w} is the dynamics driving noise and is the hypothetical derivative of Brownian motion known as white Gaussian noise with statistics

$$E\{\mathbf{w}(t)\} = \mathbf{0}$$

$$E\{\mathbf{w}(t)\mathbf{w}(t')^T\} = \mathbf{Q}(t)\delta(t-t') \quad (2.4)$$

and where $\mathbf{Q}(t)$ is described above.

The differential equation is propagated forward from some initial condition with mean $\hat{\mathbf{x}}_0$ and covariance \mathbf{P}_0 :

$$E\{\mathbf{x}(t)\} = \hat{\mathbf{x}}_0$$

$$E\{[\mathbf{x}(t) - \hat{\mathbf{x}}_0][\mathbf{x}(t) - \hat{\mathbf{x}}_0]^T\} = \mathbf{P}_0 \quad (2.5)$$

where \mathbf{P}_0 is an n-by-n symmetric and positive semidefinite matrix. If \mathbf{F} , \mathbf{G} , and \mathbf{Q} are constant and time invariant, \mathbf{P}_0 can be set to the steady state value of the covariance matrix, ensuring steady state conditions for all time. The steady state value is found by solving:

$$\dot{\mathbf{P}}(t) = \mathbf{F}\mathbf{P} + \mathbf{P}\mathbf{F}^T + \mathbf{G}\mathbf{Q}\mathbf{G}^T = \mathbf{0} \quad (2.6)$$

Measurements are available discretely as a function of the states and additive white Gaussian noise:

$$\mathbf{z}(t_i) = \mathbf{H}(t_i)\mathbf{x}(t_i) + \mathbf{v}(t_i) \quad (2.7)$$

where

- $\mathbf{z}(t_i)$ = the Kalman filter model measurement vector,
- $\mathbf{H}(t_i)$ = the Kalman filter model output matrix,
- $\mathbf{v}(t_i)$ = additive white Gaussian measurement noise,
- t_i = the i^{th} discrete measurement time.

The statistics of \mathbf{v} are similar to the statistics of \mathbf{w} and are as follows:

$$E\{\mathbf{v}(t_i)\} = \mathbf{0}$$

$$E\{\mathbf{v}(t_i)\mathbf{v}(t_j)^T\} = \begin{cases} \mathbf{R}(t_i) & t_i = t_j \\ \mathbf{0} & t_i \neq t_j \end{cases} \quad (2.8)$$

The dynamics driving noise and the measurement noise are assumed independent:

$$E\{\mathbf{w}(t)\mathbf{v}^T(t_i)\} = \mathbf{0} \quad (2.9)$$

The filter is then propagated over the sample time from t_i to t_{i+1} , where t_i is a discrete time epoch and t_{i+1} is the next discrete time epoch, and updated at time t_{i+1} with the measurement.

An equivalent discrete-time model follows:

$$\mathbf{x}(t_{i+1}) = \Phi(t_{i+1}, t_i)\mathbf{x}(t_i) + \mathbf{B}_d(t_i)\mathbf{u}(t_i) + \mathbf{w}_d(t_i) \quad (2.10)$$

$\Phi(t_{i+1}, t_i)$, $\mathbf{B}_d(t_i)$, and $\mathbf{Q}_d(t_i)$ are found by solving the following differential equations:

$$\begin{aligned} \dot{\Phi}(t, t_i) &= \mathbf{F}(t)\Phi(t, t_i) \\ \dot{\bar{\mathbf{B}}}(t, t_i) &= \mathbf{F}(t)\bar{\mathbf{B}}(t, t_i) + \mathbf{B}(t) \\ \dot{\bar{\mathbf{Q}}}(t, t_i) &= \mathbf{F}(t)\bar{\mathbf{Q}}(t, t_i) + \bar{\mathbf{Q}}(t, t_i)\mathbf{F}^T(t) + \mathbf{G}(t)\mathbf{Q}(t)\mathbf{G}^T(t) \end{aligned} \quad (2.11)$$

These differential equations are integrated forward from the following initial conditions:

$$\bar{\Phi}(t_i, t_i) = \mathbf{I} \quad \bar{\mathbf{B}}(t_i, t_i) = \mathbf{0} \quad \bar{\mathbf{Q}}(t_i, t_i) = \mathbf{0} \quad (2.12)$$

If \mathbf{F} is time invariant $\Phi(t_{i+1}, t_i)$ can be found using a matrix exponential:

$$\Phi(t_{i+1}, t_i) = e^{\mathbf{F}(t_{i+1}-t_i)} \quad (2.13)$$

\mathbf{B}_d and \mathbf{Q}_d are also found by solving the following integrals:

$$\begin{aligned} \mathbf{B}_d(t_i) &= \int_{t_i}^{t_{i+1}} \Phi(t_{i+1}, \tau) \mathbf{B}(\tau) d\tau \\ \mathbf{Q}_d(t_i) &= \int_{t_i}^{t_{i+1}} \Phi(t_{i+1}, \tau) \mathbf{G}(\tau) \mathbf{Q}(\tau) \mathbf{Q}^T(\tau) \Phi^T(t_{i+1}, \tau) d\tau \end{aligned} \quad (2.14)$$

The discrete time white Gaussian noise $\mathbf{w}_d(t_i)$ has statistics:

$$\begin{aligned} E\{\mathbf{w}_d(t)\} &= \mathbf{0} \\ E\{\mathbf{w}_d(t_i) \mathbf{w}_d(t_j)^T\} &= \begin{cases} \mathbf{Q}_d(t_i) & t_i = t_j \\ \mathbf{0} & t_i \neq t_j \end{cases} \end{aligned} \quad (2.15)$$

The algorithm is again started from the initial conditions shown in Equation (2.5) and then the state estimates, $\hat{\mathbf{x}}$, and the covariance matrix \mathbf{P} , are propagated from the discrete time sample t_i^+ (where superscript indicates just after the measurement up at time t_i) to time t_{i+1}^- (where the superscript indicates just before discrete sample time t_{i+1}) as follows:

$$\begin{aligned} \hat{\mathbf{x}}(t_{i+1}^-) &= \Phi(t_{i+1}, t_i) \hat{\mathbf{x}}(t_i^+) + \mathbf{B}_d(t_i) \mathbf{u}(t_i) \\ \mathbf{P}(t_{i+1}^-) &= \Phi(t_{i+1}, t_i) \mathbf{P}(t_i^+) \Phi^T(t_{i+1}, t_i) + \mathbf{G}_d(t_i) \mathbf{Q}_d(t_i) \mathbf{G}_d^T(t_i) \end{aligned} \quad (2.16)$$

Note that, with \mathbf{Q}_d as in Equation 2.15, \mathbf{G}_d is \mathbf{I} . At time t_{i+1}^+ the state estimates and the covariance matrix are updated as follows:

$$\begin{aligned} \mathbf{A}(t_{i+1}) &= \mathbf{H}(t_{i+1}) \mathbf{P}(t_{i+1}^-) \mathbf{H}^T(t_{i+1}) + \mathbf{R}(t_{i+1}) \\ \mathbf{K}(t_{i+1}) &= \mathbf{P}(t_{i+1}^-) \mathbf{H}^T(t_{i+1}) \mathbf{A}(t_{i+1})^{-1} \\ \mathbf{r}(t_{i+1}) &= \mathbf{z}_{i+1} - \mathbf{H}(t_{i+1}) \hat{\mathbf{x}}(t_{i+1}^-) \\ \hat{\mathbf{x}}(t_{i+1}^+) &= \hat{\mathbf{x}}(t_{i+1}^-) + \mathbf{K}(t_{i+1}) \mathbf{r}(t_{i+1}) \\ \mathbf{P}(t_{i+1}^+) &= \mathbf{P}(t_{i+1}^-) - \mathbf{K}(t_{i+1}) \mathbf{H}(t_{i+1}) \mathbf{P}(t_{i+1}^-) \end{aligned} \quad (2.17)$$

$\mathbf{K}(t_i)$ is the Kalman gain and weights the measurements and the filter predicted measurement values to update the filter properly. The knowledge of the states improves after each update and becomes less certain as the states are propagated. The residual vector $\mathbf{r}(t_i)$ is simply the difference between the measurements, $\mathbf{z}(t_i)$, at time t_i and the filter's best estimate of the measurements before they are taken ($\mathbf{H}\hat{\mathbf{x}}(t_i^-)$). Note that a properly tuned filter will have a residual vector $\mathbf{r}(t_i)$ that is zero mean with covariance equal to the filter-computed $\mathbf{A}(t_i)$, and that is Gaussian and white. The \mathbf{A} , \mathbf{P} , and \mathbf{K} time histories require no measurement knowledge and can be precomputed offline. The linear Kalman filter is an optimum estimator by any criterion: it provides simultaneously the mean, median, and mode due to the Gaussian characteristics of both the states and the state estimation errors.

2.4.1. Multiple Model Adaptive Estimator (MMAE)

When a system has certain characteristics or parameters that can change, the system model used in the filtering algorithm may be invalid. The Kalman filter performance is only as good as the models used in the algorithm. Any characteristics not included in the model make the Kalman filter a suboptimal estimator. One way to deal with the uncertainties in the model is to develop a multiple model filtering algorithm. A multiple model adaptive estimator (MMAE) is a bank of parallel Kalman filters, each with a different filter model and an algorithm to test for the adequacy of the assumed model in each filter [40].

One could create a discretized parameter space from the continuous parameter space of all possible parameter values. Let \mathbf{a} be a vector of all possible parameter values

$\{\mathbf{a}_1, \mathbf{a}_2, \dots, \mathbf{a}_j\}$ ($j=1,2,\dots,J$). A bank of Kalman filters is designed for each of the parameters as follows:

$$\begin{aligned}\mathbf{x}_j(t_{i+1}) &= \Phi_j(t_{i+1}, t_i)\mathbf{x}_j(t_i) + \mathbf{B}_{dj}(t_i)\mathbf{u}_j(t_i) + \mathbf{w}_{dj}(t_i) \\ \mathbf{z}_j(t_{i+1}) &= \mathbf{H}_j(t_{i+1})\mathbf{x}_j(t_{i+1}) + \mathbf{v}_j(t_{i+1})\end{aligned}\quad (2.18)$$

where

- $\mathbf{x}_j(t_i)$ = the Kalman filter model state vector for parameter j
- $\Phi_j(t_{i+1}, t_i)$ = the Kalman filter state transition matrix for parameter j
- $\mathbf{B}_{dj}(t_i)$ = the Kalman filter model control input matrix for parameter j
- $\mathbf{u}_j(t_i)$ = the system input vector for parameter j

and where \mathbf{w}_{dj} and \mathbf{v}_j are independent and are both zero-mean white Gaussian noise with statistics:

$$\begin{aligned}E\{\mathbf{v}_j(t_i)\mathbf{v}_j(t_j)^T\} &= \begin{cases} \mathbf{R}_j(t_i) & t_i = t_j \\ \mathbf{0} & t_i \neq t_j \end{cases} \\ E\{\mathbf{w}_{dj}(t_i)\mathbf{w}_{dj}(t_j)^T\} &= \begin{cases} \mathbf{Q}_{dj}(t_i) & t_i = t_j \\ \mathbf{0} & t_i \neq t_j \end{cases}\end{aligned}\quad (2.19)$$

Each Kalman filter is propagated by

$$\begin{aligned}\hat{\mathbf{x}}_j(t_{i+1}^-) &= \Phi_j(t_{i+1}, t_i)\hat{\mathbf{x}}_j(t_i^+) + \mathbf{B}_{dj}(t_i)\mathbf{u}_j(t_i) \\ \mathbf{P}_j(t_{i+1}^-) &= \Phi_j(t_{i+1}, t_i)\mathbf{P}_j(t_i^+)\Phi_j^T(t_{i+1}, t_i) + \mathbf{Q}_{dj}(t_i)\end{aligned}\quad (2.20)$$

and is updated by

$$\begin{aligned}\mathbf{A}_j(t_{i+1}) &= \mathbf{H}_j(t_{i+1})\mathbf{P}_j(t_{i+1}^-)\mathbf{H}_j^T(t_{i+1}) + \mathbf{R}_j(t_{i+1}) \\ \mathbf{K}_j(t_{i+1}) &= \mathbf{P}_j(t_{i+1}^-)\mathbf{H}_j^T(t_{i+1})\mathbf{A}_j(t_{i+1})^{-1} \\ \mathbf{r}_j(t_{i+1}) &= \mathbf{z}_{i+1} - \mathbf{H}_j(t_{i+1})\hat{\mathbf{x}}_j(t_{i+1}^-) \\ \hat{\mathbf{x}}_j(t_{i+1}^+) &= \hat{\mathbf{x}}_j(t_{i+1}^-) + \mathbf{K}_j(t_{i+1})\mathbf{r}_j(t_{i+1}) \\ \mathbf{P}_j(t_{i+1}^+) &= \mathbf{P}_j(t_{i+1}^-) - \mathbf{K}_j(t_{i+1})\mathbf{H}_j(t_{i+1})\mathbf{P}_j(t_{i+1}^-)\end{aligned}\quad (2.21)$$

where the subscript j denotes the elemental filter modeled with parameter vector \mathbf{a}_j .

Each elemental filter is given the same measurements and will produce an optimal state or parameter estimate based on its internal model. The residual vector $\mathbf{r}_j(t_i)$ and the filter computed covariance of the residual vector $\mathbf{A}_j(t_i)$ are measures of how well the filter models the real world. Note that the MMAE uses three residual characteristics from a correctly modeled system: they should be zero-mean, Gaussian and with a covariance $\mathbf{A}_j(t_i)$. Each filter's $\mathbf{Q}_{d,j}$ and \mathbf{R}_j values should be tuned such that it achieves its best performance given that the filter models the true system.

A block diagram of the MMAE is shown in Figure 2-8. Note the outputs of the hypothesized system models are scaled by a probability weighting computation.

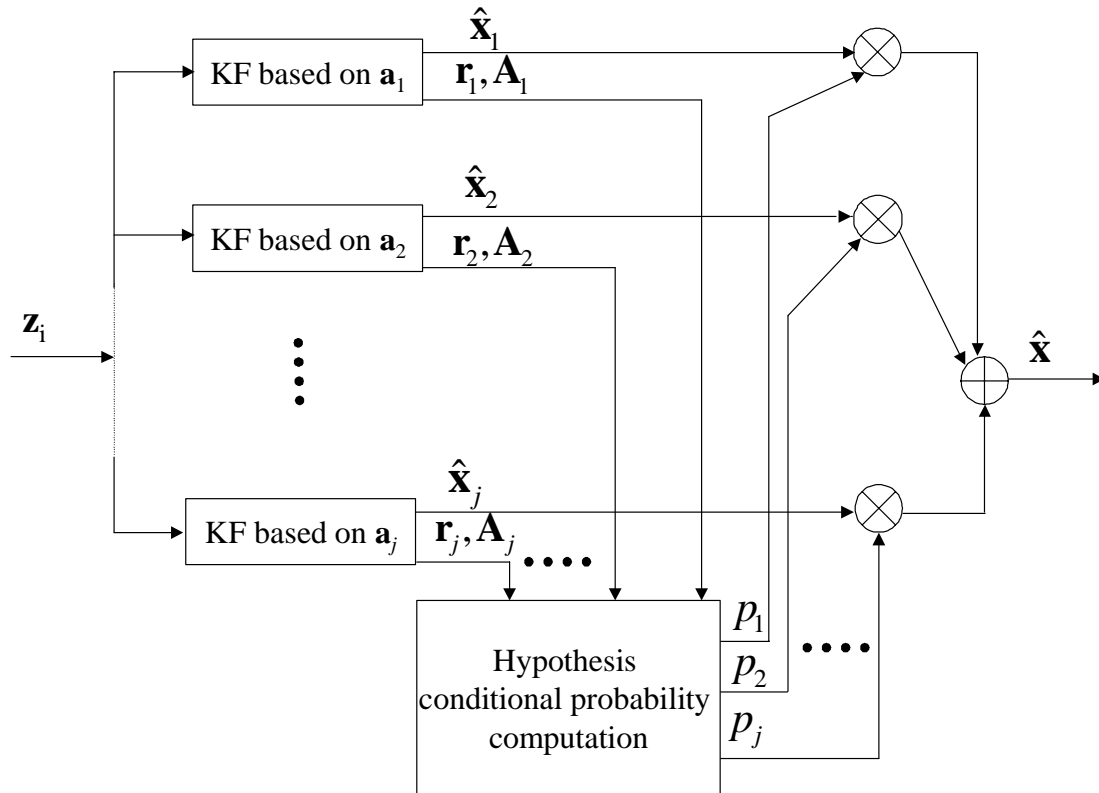


Figure 2-8. Multiple Model Filtering Algorithm Block Diagram

The hypothesis conditional probability computation in Figure 2-8 is a conditional probability that the parameter vector \mathbf{a} assumes the true value \mathbf{a}_j conditioned on the measurement history \mathbf{Z}_i , defined as

$$p_j(t_i) = \text{prob}\{\mathbf{a} = \mathbf{a}_j / \mathbf{Z}(t_i) = \mathbf{Z}_i\}. \quad (2.22)$$

The probability of each filter modeling the true system can be evaluated as a function of both the vector of parameter values and the measurement history through a probability density function and the probability weighting at a sample time earlier:

$$p_j(t_i) = \frac{f_{\mathbf{z}(t_i)|\mathbf{a}, \mathbf{Z}(t_{i-1})}(\mathbf{z}_i | \mathbf{a}_j, \mathbf{Z}_{i-1}) p_j(t_{i-1})}{\sum_{n=1}^J f_{\mathbf{z}(t_i)|\mathbf{a}, \mathbf{Z}(t_{i-1})}(\mathbf{z}_i | \mathbf{a}_n, \mathbf{Z}_{i-1}) p_n(t_{i-1})} \quad (2.23)$$

The conditional density function of the current measurement vector $\mathbf{z}(t_i)$ based on the parameter vector \mathbf{a}_j and the measurement history \mathbf{Z}_{i-1} can be shown to be [40]:

$$f_{\mathbf{z}(t_i)|\mathbf{a}, \mathbf{Z}(t_{i-1})}(\mathbf{z}_i | \mathbf{a}_j, \mathbf{Z}_{i-1}) = \frac{1}{(2\pi)^{m/2} |\mathbf{A}(t_i)|^{1/2}} \exp\left\{-\frac{1}{2} \mathbf{r}_j^T(t_i) \mathbf{A}_j(t_i)^{-1} \mathbf{r}_j(t_i)\right\} \quad (2.24)$$

where m is the number of measurements. When filter j 's model matches the true system, the residual vector $\mathbf{r}_j(t_i)$ will be zero mean with covariance $\mathbf{A}_j(t_i)$. Filter Probabilities are started out such that

$$p_j(t_i) = 1/J \quad (2.25)$$

and are then updated after each measurement incorporation by Equation 2.24. Note that the denominator is a scaling factor to ensure that the filter probabilities add up to one. In certain cases, the elemental filter residuals can seem good causing the filter to generate an erroneous probability, especially if its residual is going through zero at the time of the update.

The final state estimate from the MMAE is a blend of all the hypothesized system model outputs and their associated filter computed probabilities:

$$\begin{aligned}\hat{\mathbf{x}}(t_i^+) &= E\{\mathbf{x}(t_i) | \mathbf{Z}(t_i) = \mathbf{Z}_i\} \\ &= \sum_{j=1}^J \hat{\mathbf{x}}_j(t_i^+) p_j(t_i) \\ \mathbf{P}(t_i^+) &= \sum_{j=1}^J p_j(t_i) \{ \mathbf{P}_j(t_i^+) + [\hat{\mathbf{x}}_j(t_i^+) - \hat{\mathbf{x}}(t_i^+)] [\hat{\mathbf{x}}_j(t_i^+) - \hat{\mathbf{x}}(t_i^+)]^T \}\end{aligned}\quad (2.26)$$

where $\mathbf{P}_j(t_i^+)$ is the state error covariance as computed by the Kalman filter associated with parameter \mathbf{a}_j .

2.4.2. State Estimation vs. Parameter Estimation

It was noted previously that the filter model based on hypothesis \mathbf{a}_j should first be tuned for optimal performance given that the filter models the true system. This type of tuning will yield good state estimates and may not give the best estimation of the true system parameter. Herein lies the tradeoff that the designer must weight for his own benefit. Conservative tuning efforts (for instance, using a large \mathbf{Q}_j so that the filter overestimates its own errors in the computed $\mathbf{P}_j(t_i)$ and $\mathbf{A}_j(t_i)$) may enhance state estimation performance but may also mask the differences in models. Thus, while a conservatively tuned filter may have a very good blended state estimate output, the parameter estimate may be hampered. Because the MMAE will be used for parameter estimation of the ECG signal, tight tuning of the Kalman filter is desired at the risk of producing divergent filters. However, the filters can easily be restarted, if divergence does occur. If the $\mathbf{r}_j^T(t_i) \mathbf{A}_j(t_i)^{-1} \mathbf{r}_j(t_i)$ is above a certain limit, typically an order of magnitude larger than the expected, the filter is declared divergent. The divergent filter's

$\hat{\mathbf{x}}$ and \mathbf{P} are reset to the MMAE's blended output using only the nondivergent filters and the probability is set to the lower bound.

2.4.3. Lower Probability Bounds

One would expect the probability of the filter associated with the “correct” hypothesis to increase while the probabilities of the other filters decrease. As shown in Equation (2.24), the probability calculation is recursive in nature. The lower a filter's probability, the longer the probability takes to transition to larger values when that filter's hypothesis is, in fact, correct. In extreme cases, if a filter's probability goes to zero, the filter will never come back from zero probability. Thus, a lower probability bound for each filter will balance the speed at which a filter transitions from a low probability to a high probability and will prevent the MMAE from eliminating a filter from its bank. Henderson [23] noted that lower probability bounds (ϵ) are typically in the range of $0.0005 < \epsilon < 0.01$, while he found that a value of $\epsilon = 0.001$ worked best for his purposes.

2.5 Summary

The open literature supports the need for a wearable sensor system that supports a real-time remote physiological monitoring system. Several in the biomedical community have worked to make sensors more comfortable while still maintaining accuracy and reliability. The immediate effects of stress on the body in a physically taxing environment are now only beginning to be studied outside of the laboratory. While exercise stress testing and other forms of controlled research have been accomplished, research in the correlation between perceived work and physical performance has only

recently been undertaken. Few have studied the physiological responses of people in stressful environments. Even though FitSense Technologies has a system capable of team monitoring, there is still much work to be done in this area. Using the recent advancements in non-invasive monitoring, GPS, and wireless technology, a unique wearable monitoring system can be developed and applied to numerous areas of interest. The warning system based on parameter estimation and system identification algorithm will provide a warning when a person is in danger. The ECG signal provides a wealth of information about the heart and the autonomic nervous system, the physical condition, and possibly some more relationships that can be exploited with the online identification software. The MMAE provides a strong basis for parameter estimation of the ECG waveform, given its ability to calculate a probability for each parameter value based on the measurements it receives. Chapter 3 will lay out the methodology for developing the ECG processing algorithm using the MMAE as the basis.

3. Methodology

3.1 Overview

This chapter presents the system model development, digital signal processing, hypothesis testing techniques, and analysis techniques for the electrocardiogram (ECG) processing algorithm. First, an overall development process description is presented. Then, the signal processing technique is detailed, followed by the descriptions pertaining to the hypothesis models and the Kalman filtering equations. Next, the hypothesis testing techniques are presented. This is followed by the description of the algorithm used to determine the heart rate accurately. Finally, approaches to analyze the MMAE ECG processing algorithm accuracy and robustness are presented.

3.2 Design and Analysis Process

The ECG segmentation algorithm development was an iterative process, as shown in Figure 3-1. The process started with ECG signal analysis and possible segmentation techniques, i.e. ways to extract the segments of interest from the ECG waveform. A sample ECG signal was analyzed both in the time domain and in the frequency domain to grasp the signal dynamics. Hypothesized system models were developed based on the insight gained from the sample ECG signal analysis. These hypothesized models were developed as distinctly as possible from each other. The hypothesized models were used in the ECG segmentation algorithm and the performance was tested on a sample signal. If the algorithm did not perform as expected, then hypothesis model parameter tuning or

algorithm modification was required. This process continued until the algorithm performed well given several different sample signals.

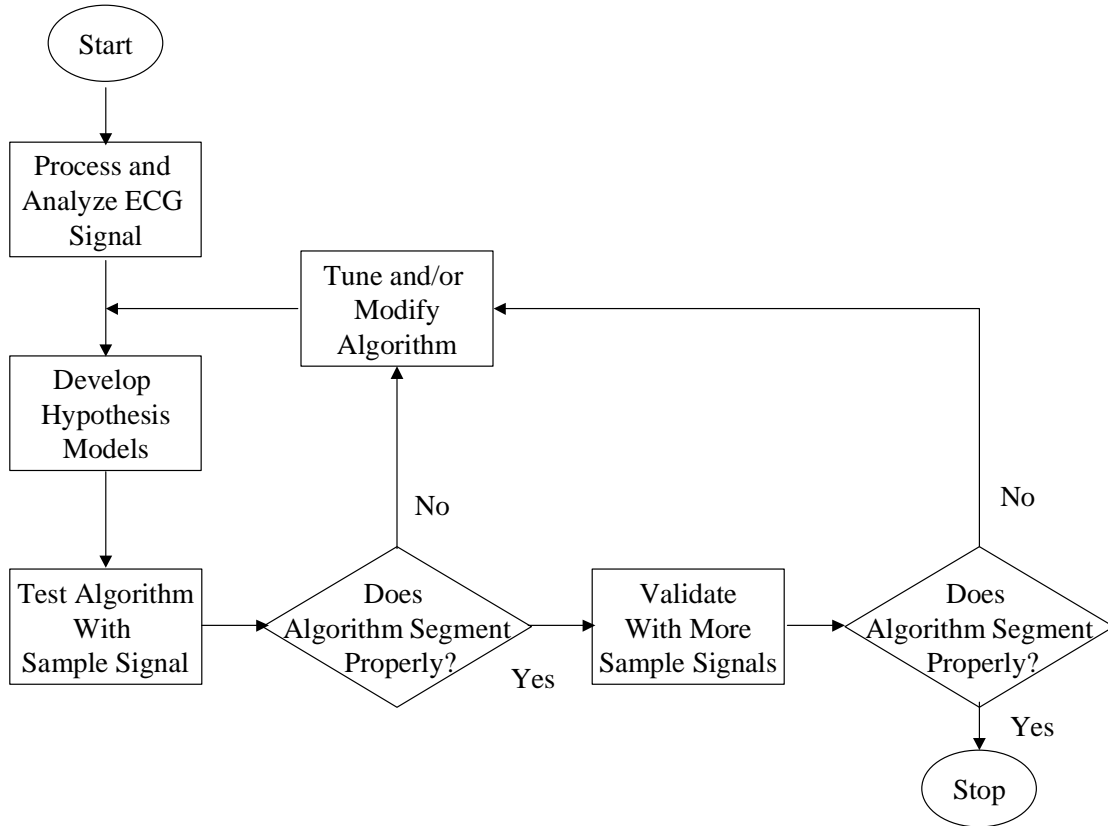


Figure 3-1. Algorithm Development and Testing Process

3.3 ECG signal analysis

The first step in developing a hypothesis model for the filter bank was to segment the signal based on the ECG characteristic waveform. The P-wave, QRS complex, and T-wave segments were visually selected from a signal taken from the MIT ECG database. Based on the visual waveform segmentation, a segment power spectral density estimate was formed for each segment type. Then, a PSD was compared to several well-defined stochastic system models and white Gaussian noise (WGN) shaping filters [37, 39]. Once the PSD matched a stochastic system model, then hypothesis models for the

MMAE were developed. Note that the models do not have to be based on the signal itself; they can be based on signal derivatives.

3.3.1. Differentiator

The continuous time derivative transfer function is:

$$H(\omega) = j\omega \quad (3.1)$$

The differentiator discrete time equivalent can be approximated with a high order finite impulse response (FIR) filter. A sufficiently high order FIR filter was created in MATLAB[®] using a least squares approach to approximate this frequency response. The transfer function for a 29-order filter is shown in Figure 3-2:

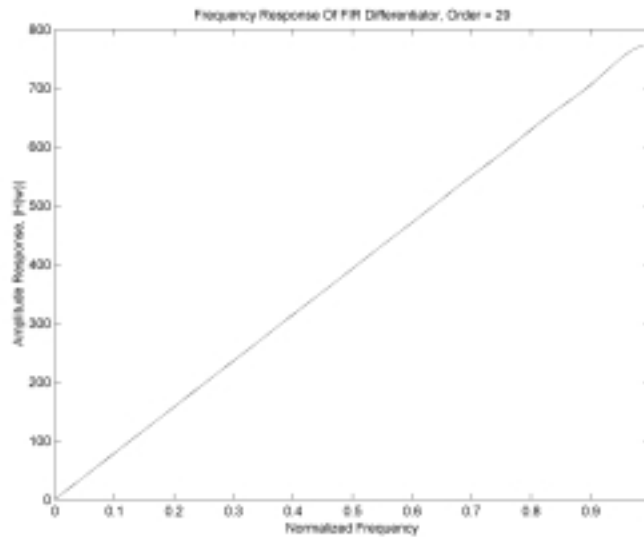


Figure 3-2. FIR Differentiator

An odd order filter was selected because the amplitude response, $|H(\omega)|$, at the Nyquist frequency, $f_s/2$, could be set to the desired gain. An even order filter requires the amplitude response at the Nyquist frequency to be zero. The FIR differentiator is

advantageous in that it has a linear phase response, meaning that the derivative of the phase response, or the group delay, is constant [48]. The signals were differentiated using the high order differentiator and were then shifted to correct for the group delay, τ_g , given in Equation (3.2):

$$\tau_g = \frac{M-1}{2} = 14 \quad (3.2)$$

where

τ_g = the delay in number of samples

M = the filter order.

Once the signal is differentiated and the proper group delay is applied to the derivatives, the P-wave, QRS complex, and T-wave segments are visually selected from the ECG signal. The ECG signal derivatives are also segmented using the same segment indices for each sequence. An example ECG sample and its associated first and second derivatives are shown in Figure 3-3.

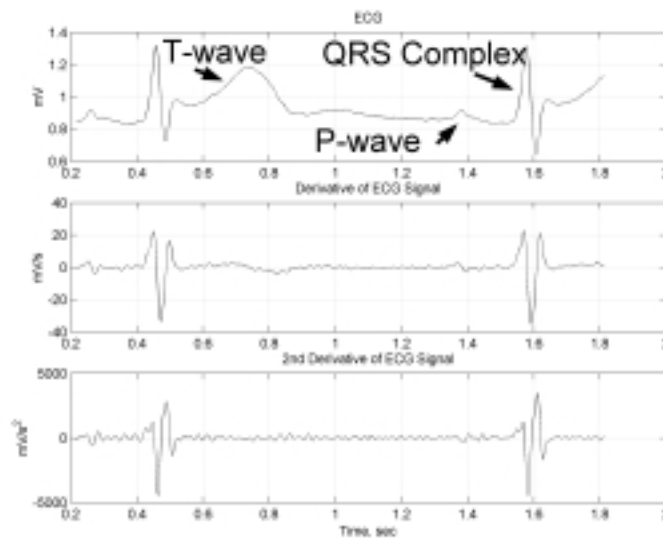


Figure 3-3. Sample ECG Signal, ECG Signal 1st Derivative, and 2nd Derivative

Note that the time domain signal analysis does not provide a great amount of information. While there is a large amplitude change in the derivatives, this does not give great insight into how the signal can be modeled. Frequency domain techniques provide greater insight into the signal dynamics. A segment power spectral density estimate is a better choice, and can be obtained if some assumptions about the signal are made. These assumptions are presented in the next section.

3.3.2. *Signal Assumptions*

To estimate the ECG waveform power spectral density using a Fourier transform, several assumptions must first be made. The ECG signal itself is not stationary; the ECG characteristic waveform segments are “quasi-stationary.” The ECG segments can be considered quasi-stationary, meaning that, while the statistics of the ECG signal change in time, the statistics of the segments change very slowly with respect to the characteristic ECG waveform length. Additionally, the correlation function is strictly a function of the time offset, τ , and the segment probability density function is time-invariant [21].

3.3.3. *Correlation and Power Spectral Density Functions*

A sequence autocorrelation is defined as

$$\Psi(\tau) = \frac{1}{N-1} \sum_{n=(N-1-\tau)}^{N-1-\tau} \mathbf{x}(t_{i-n})\mathbf{x}(t_{i-n-\tau}). \quad (3.3)$$

where

$\Psi(\tau)$ = the autocorrelation function

$\mathbf{x}(t_i)$ = the discrete signal sequence

- N = the length of \mathbf{x}
- τ = the number of samples of offset.

The autocorrelation function shows how well the signal relates to itself as a function of the time offset, τ . A segment PSD estimate is then the Fourier transform of the autocorrelation function:

$$\bar{\Psi}(f) = \frac{1}{N-1} \sum_{\tau=-(N-1)}^{N-1} \sum_{n=-(N-1-\tau)}^{N-1-\tau} \mathbf{x}(t_{i-n}) \mathbf{x}(t_{i-n-\tau}) \exp(-j2\pi f \tau). \quad (3.4)$$

where

- $\bar{\Psi}(f)$ = the PSD
- $\mathbf{x}(t_i)$ = the discrete signal sequence
- N = the length of \mathbf{x}
- τ = the number of samples of offset
- f = frequency in Hz.

The PSD estimate can be similarly computed from the sequence's Fourier transform itself as follows:

$$\bar{\Psi}(f) = \frac{1}{N-1} \left| \sum_{n=0}^{N-1} \mathbf{x}(t_{i-n}) \exp(-j2\pi f \tau) \right|^2. \quad (3.5)$$

where $\bar{\Psi}(f)$, \mathbf{x} , N , τ , and f are defined above.

Equation (3.5) is a desirable way to compute a PSD estimate because Fast Fourier transforms (FFT) are very quick and efficient [39]. A PSD estimate was computed for each individual ECG signal segment. Zero padding each signal segment to 512 samples was used in the FFT calculation to improve the waveform density in the frequency domain. While this technique does not improve the frequency resolution, it

does give a better visual representation of the frequency characteristics. The frequency interval is inversely proportional to the total signal time, NT , (where N is the number of samples and T is the sampling period) as shown Equation (3.6) [48]:

$$\Delta f = 1 / NT \quad (3.6)$$

Equation (3.6) shows that as the signal length decreases in time, the corresponding frequency interval increases when using the Fourier transform. An example PSD estimate for the ECG signal segments is shown in Figure 3-4, Figure 3-5, and Figure 3-6. The top plot shows the PSD estimate for the specific signal segment, and the bottom plot shows the PSD estimate for the specific segment's first derivative.

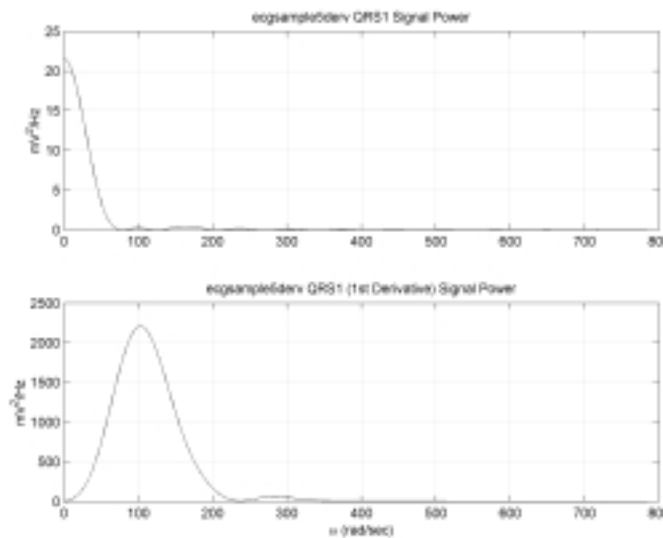


Figure 3-4. PSD Estimate for Sample QRS Complex Segment and 1st Derivative

Figure 3-4 through Figure 3-6 give insight into the ECG signal segment dynamics. Specifically, it is readily apparent that the PSD estimate for each signal segment's first derivative looks like a bandpass filter's output, each with its own center frequency and gain.

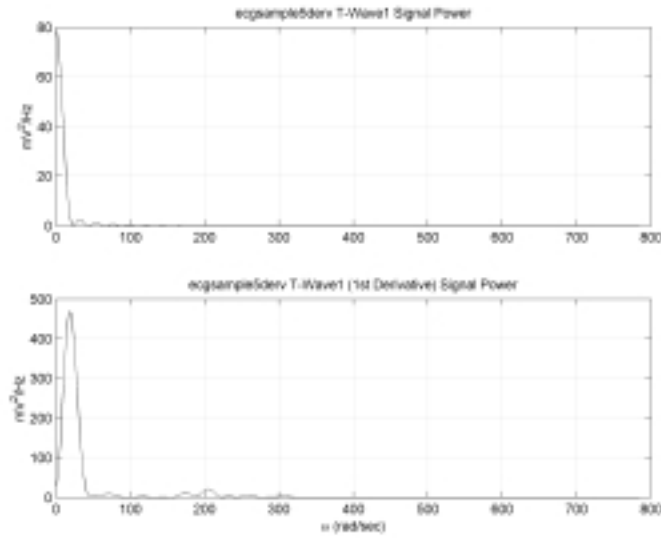


Figure 3-5. PSD Estimate for Sample T-Wave Segment and 1st Derivative

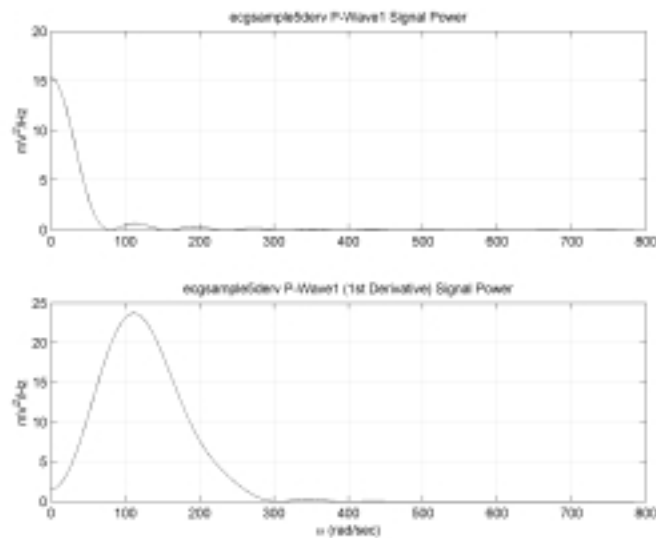


Figure 3-6. PSD Estimate for Sample P-Wave Segment and 1st Derivative

Nineteen additional ECG signals were segmented and analyzed by the same process. PSD analysis shows that the ECG signal segment derivatives all have bandpass filter characteristics, as shown in Table 3-1. For each signal segment (P-wave, QRS

complex, and T-wave), the bandpass filter center frequency, ω_c , and the gain, σ^2 , are given. The signals are separated into signal 1 and signal 2 based on the format from the MIT ECG database [13], showing that the different leads require different tuning.

Table 3-1. Hypothesis Model Parameters from Ten Sample Data Sets

Sample	data set	signal 1	P- ω_c	P- σ^2	QRS- ω_c	QRS- σ^2	T- ω_c	T- σ^2
3	e0103	V4	45	93	106	3100	23	451
5	e0105	V4	112	27	104	2200	18	435
11	e0111	MLIII	59	22	116	1725	35	460
13	e0113	MLIII	108	11.5	112	6950	32	49
19	e0119	V4	42	112	114	13400	32	500
21	e0121	V4	46	157	131	23000	31	760
23	e0123	V4	35	82	118	25700	18	110
25	e0125	V4	34	81	110	18000	51	127
27	e0127	V4	43	35	107	23000	32	26
39	e0139	MLIII	61	45	183	2525	20	14.4
Mean			58.5	66.6	120.1	11960.0	29.2	293.2
Sample	data set	signal 2	P- ω_c	P- σ^2	QRS- ω_c	QRS- σ^2	T- ω_c	T- σ^2
3	e0103	MLIII	47	10.8	83	1810	30	33
5	e0105	MLIII	44	20	75	8000	20	18.5
11	e0111	V4	43	157	103	32500	26	596
13	e0113	V4	55	49	135	30500	23	164
19	e0119	MLIII	50	260	85	5060	52	98
21	e0121	MLIII	44	70	128	2430	54	9.4
23	e0123	MLIII	42	16	90	1135	28	54
25	e0125	MLIII	31	22	95	580	26	105
27	e0127	MLIII	62	66	142	4400	33	50
39	e0139	V4	45	54	94	15800	25	29
Mean			46.3	72.5	103.0	10221.5	31.7	115.7

Note in Table 3-1 that the mean values for the center frequencies, ω_c , and the gains, σ^2 , for each signal segment are very distinct. Knowing that the individual segment dynamics are very different, hypotheses based on a bandpass filter could be developed.

3.4 System Modeling

A bandpass filter's transfer function can be described as:

$$G(s) = \frac{s + \omega_n}{s^2 + 2\alpha s + \omega_n^2} \quad (3.7)$$

where ω_n and α are defined as:

$$\begin{aligned} \alpha &= \text{half power frequency from center frequency, } \omega_c, \text{ and} \\ \omega_n &= (\alpha^2 + \omega_c^2)^{0.5}. \end{aligned} \quad (3.8)$$

This filter always gives a peak value of $\sigma^2 \alpha^{-1}$ with the assumption that the driving function is WGN and has strength $2\alpha\sigma^2$. This bandpass filter form allows easy center frequency and bandpass region width manipulation.

The transfer function is then put into observable state-space form as follows:

$$\underbrace{\begin{bmatrix} \dot{x}_1(t) \\ \dot{x}_2(t) \end{bmatrix}}_{\mathbf{x}(t)} = \underbrace{\begin{bmatrix} 0 & 1 \\ -\omega_n^2 & -2\alpha \end{bmatrix}}_{\mathbf{F}} \underbrace{\begin{bmatrix} x_1(t) \\ x_2(t) \end{bmatrix}}_{\mathbf{x}(t)} + \underbrace{\begin{bmatrix} g_1 \\ g_2 \end{bmatrix}}_{\mathbf{G}} w(t) \quad (3.9)$$

$$z(t) = \underbrace{\begin{bmatrix} 1 & 0 \end{bmatrix}}_{\mathbf{H}} \underbrace{\begin{bmatrix} x_1(t) \\ x_2(t) \end{bmatrix}}_{\mathbf{x}(t)} \quad (3.10)$$

where

- $\mathbf{x}(t)$ = the state vector
- \mathbf{F} = the state dynamics matrix
- \mathbf{G} = the noise input matrix
- $w(t)$ = the scalar WGN
- $z(t)$ = the scalar output
- \mathbf{H} = the output matrix.

\mathbf{G} comes from the Laurent series coefficients for $G(s)$. The Laurent series is simply the remainder coefficients of a long division operation on the transfer function $G(s)$:

$$G(s) = \frac{1s^{-1} + (\omega_n - 2\alpha)s^{-2}}{s^2 + 2\alpha s + \omega_n^2} \cdot \frac{s + \omega_n}{-(s + 2\alpha)} \cdot \frac{\omega_n - 2\alpha}{\omega_n - 2\alpha} \quad (3.11)$$

From Equation (3.11), \mathbf{G} was:

$$\mathbf{G} = \begin{bmatrix} 1 \\ \omega_n - 2\alpha \end{bmatrix} \quad (3.12)$$

Thus, the hypothesis models for the individual ECG segments are easily implemented knowing the state-space form and the three parameters, ω , σ^2 , and α

3.4.1. Hypothesis Filter Parameters

Ten sample data sets taken from the MIT ECG database [13] were differentiated and segmented, as in Section 3.3.1. PSD's were generated followed by determining the filter parameters for each data set. The results are shown in Table 3-1 in Section 3.3. An additional "Rest" hypothesis was created to account for the samples between the T-wave offset and the P-wave onset when the heart was resting and very little activity was taking place. The "Rest" hypothesis looks for low frequencies and low strength in the signal derivative. The filter parameters in Table 3-2 were then used as the basis for the hypothesis models:

Table 3-2. Hypothesis Filter Parameters

Hypothesis	QRS Complex	T-Wave	“Rest”	P-Wave
ω_c	110	35	10	65
σ^2	15000	360	0.1	60
α	1	1	10	1

Note the strong distinctions in the center frequencies and the σ^2 values. The bandpass filter width was specifically chosen to be narrow to enhance distinction among the different hypotheses. If the filter hypotheses are distinct, then the residuals from each model will also be distinct, aiding the conditional hypothesis probability calculation, which is based on the residuals.

3.5 Kalman Filter Design

The Kalman filter as discussed in Chapter 2 was the basis for each hypothesis model. The model was developed in state-space form consisting of the dynamics matrix and a WGN driving term was assumed as shown in Equation (3.13).

$$\dot{\mathbf{x}}(t) = \mathbf{F}\mathbf{x}(t) + \mathbf{G}w(t) \quad (3.13)$$

where $w(t)$ is scalar WGN with statistics

$$\begin{aligned} E\{w(t)\} &= 0 \\ E\{w(t)w(t+\tau)\} &= Q(t)\delta(\tau) \end{aligned} \quad (3.14)$$

and where Q is a positive semidefinite scalar. The Kalman filter model used was based on the state space model in Equation (3.9) and Equation (3.10). An additional state was implemented because the measurement was the signal itself, not the signal's first derivative for which the preceding PSD's were computed to yield the bandpass filter model in Section 3.4. The Kalman filter model is then:

$$\underbrace{\begin{bmatrix} \dot{x}_1(t) \\ \dot{x}_2(t) \\ \dot{x}_3(t) \end{bmatrix}}_{\dot{\mathbf{x}}(t)} = \underbrace{\begin{bmatrix} 0 & 1 & 0 \\ 0 & 0 & 1 \\ 0 & -\omega_n^2 & -2\alpha \end{bmatrix}}_{\mathbf{F}} \underbrace{\begin{bmatrix} x_1(t) \\ x_2(t) \\ x_3(t) \end{bmatrix}}_{\mathbf{x}(t)} + \underbrace{\begin{bmatrix} 0 \\ 1 \\ \omega_n - 2\alpha \end{bmatrix}}_{\mathbf{G}} w(t) \quad (3.15)$$

The input WGN driving term has statistics:

$$\begin{aligned} E\{w(t)\} &= 0 \\ E\{w(t)w(t+\tau)\} &= Q(t)\delta(\tau) = 2\alpha\sigma^2\delta(\tau) \end{aligned} \quad (3.16)$$

These statistics come from the transfer function's assumption that the input WGN strength is $2\alpha\sigma^2$.

The differential equation was propagated forward from some initial condition with mean $\hat{\mathbf{x}}_0$ and covariance \mathbf{P}_0 :

$$\begin{aligned} E\{\mathbf{x}(t_0)\} &= \hat{\mathbf{x}}_0 = [0 \ 0 \ 0]^T \\ E\{[\mathbf{x}(t_0) - \hat{\mathbf{x}}_0][\mathbf{x}(t_0) - \hat{\mathbf{x}}_0]^T\} &= \mathbf{P}_0 \end{aligned} \quad (3.17)$$

where \mathbf{P}_0 is an n-by-n symmetric and positive semidefinite matrix. \mathbf{P}_0 was found by setting Equation (2.6) equal to zero. \mathbf{P}_0 was determined to be:

$$\mathbf{P}_0 = \begin{bmatrix} 1 & 0 & 0 \\ 0 & \sigma^2 & -\alpha\sigma^2 \\ 0 & -\alpha\sigma^2 & 0.5\sigma^2(\omega_n^2 + (\omega_n - 2\alpha)^2) \end{bmatrix} \quad (3.18)$$

where ω_n , α , and σ^2 were the system model transfer function parameters defined in Equation (3.8).

Measurements were available discretely as a function of the states and additive WGN:

$$z(t_i) = [1 \ 0 \ 0]\mathbf{x}(t_i) + v(t_i) \quad (3.19)$$

The v statistics were as follows:

$$E\{v(t_i)\} = 0$$

$$E\{v(t_i)v(t_j)^T\} = \begin{cases} R(t_i) = 0.005 & t_i = t_j \\ 0 & t_i \neq t_j \end{cases} \quad (3.20)$$

R was set to 0.005, meaning that the measurements were essentially noiseless. This allows the Kalman filter to weight the measurements very heavily. The effect is easy to see through the Kalman gain matrix. As the R -value goes down, K goes up. This affects both the state estimate and the filter-computed covariance. The state estimate is affected in the residual term and the filter computed covariance is smaller. The R value also affects how quickly the state estimates follow the measurements. A lower R value allows the filter to follow the measurements closely. The dynamics driving noise and the measurement noise were assumed independent:

$$E\{w(t)v(t_i)\} = 0 \quad (3.21)$$

The continuous-time filter was converted to its equivalent discrete filter [39] in Equation (2.11). In this case the \mathbf{B}_d term is $\mathbf{0}$ and not included in the model:

$$\mathbf{x}(t_{i+1}) = \Phi(t_{i+1}, t_i)\mathbf{x}(t_i) + w_d(t_i) \quad (3.22)$$

where $\Phi(t, t_i)$ is the state transition matrix. Because \mathbf{F} in Equation (3.13) is time invariant, Φ can be found using a matrix exponential:

$$\Phi(t_{i+1}, t_i) = e^{\mathbf{F}(t_{i+1}-t_i)} \quad (3.23)$$

\mathbf{Q}_d is found by solving the following integral:

$$\mathbf{Q}_d(t_i) = \int_{t_i}^{t_{i+1}} \Phi(t_{i+1}, \tau)\mathbf{G}\mathbf{Q}\mathbf{G}^T\Phi^T(t_{i+1}, \tau)d\tau \quad (3.24)$$

The algorithm is started from the initial conditions $\hat{\mathbf{x}}_0$ and \mathbf{P}_0 in Equation (3.17) and then the states are propagated to time t_{i+1}^- as follows:

$$\begin{aligned}\hat{\mathbf{x}}(t_{i+1}^-) &= \Phi(t_{i+1}, t_i) \hat{\mathbf{x}}(t_i^+) \\ \mathbf{P}(t_{i+1}^-) &= \Phi(t_{i+1}, t_i) \mathbf{P}(t_i^+) \Phi^T(t_{i+1}, t_i) + \mathbf{Q}_d(t_i)\end{aligned}\quad (3.25)$$

and at time t_{i+1}^+ are updated as follows:

$$\begin{aligned}A(t_{i+1}) &= \mathbf{H}(t_{i+1}) \mathbf{P}(t_{i+1}^-) \mathbf{H}^T(t_{i+1}) + R(t_{i+1}) \\ \mathbf{K}(t_{i+1}) &= \mathbf{P}(t_{i+1}^-) \mathbf{H}^T(t_{i+1}) A(t_{i+1})^{-1} \\ r(t_{i+1}) &= z_{i+1} - \mathbf{H}(t_{i+1}) \hat{\mathbf{x}}(t_{i+1}^-) \\ \hat{\mathbf{x}}(t_{i+1}^+) &= \hat{\mathbf{x}}(t_{i+1}^-) + \mathbf{K}(t_{i+1}) r(t_{i+1}) \\ \mathbf{P}(t_{i+1}^+) &= \mathbf{P}(t_{i+1}^-) - \mathbf{K}(t_{i+1}) \mathbf{H}(t_{i+1}) \mathbf{P}(t_{i+1}^-)\end{aligned}\quad (3.26)$$

3.5.1. Multiple Model Adaptive Estimator (MMAE) Design

It was shown in Chapter 2 that uncertain parameters in the Kalman filter system model could be handled using an MMAE. The uncertain parameters in this case were the bandpass filter center frequency and the input driving noise gain, as shown in Section 3.4.1. A hypothesis model based on \mathbf{a}_j was developed as follows:

$$\begin{aligned}\mathbf{x}_j(t_{i+1}) &= \Phi_j(t_{i+1}, t_i) \mathbf{x}_j(t_i) + w_{dj}(t_i) \\ z_j(t_{i+1}) &= \mathbf{H}_j \mathbf{x}_j(t_{i+1}) + v_j(t_{i+1})\end{aligned}\quad (3.27)$$

where w_{dj} and v_j are independent and are both zero-mean WGN with statistics

$$\begin{aligned}E\{v_j(t_i) v_j(t_j)\} &= \begin{cases} R_j(t_i) & t_i = t_m \\ 0 & t_i \neq t_m \end{cases} \\ E\{w_{dj}(t_i) w_{dj}(t_j)\} &= \begin{cases} Q_{dj}(t_i) & t_i = t_m \\ 0 & t_i \neq t_m \end{cases}\end{aligned}\quad (3.28)$$

The continuous-time WGN strength was given by the driving term in Equation (3.16).

The discrete equivalent WGN was found using Equation (3.24). The measurement noise was given in Equation 3.20.

Each elemental Kalman filter is propagated by Equation (3.25) and is updated by Equation (3.26). Each hypothesis model is given the same measurement, z_{i+1} , and produces an optimal state estimate based on its hypothesis model. The hypotheses' Q and R values should be tuned such that each hypothesis performs well when the hypothesis model matches the true system model. Tuning parameters for 20 signals are shown in Section 3.5.3.

The conditional probability that the parameter vector assumes the value \mathbf{a}_j conditioned on the measurement history \mathbf{Z}_i for each parameter is defined as

$$p_j(t_i) = \text{prob}\{\mathbf{a} = \mathbf{a}_j / \mathbf{Z}(t_i) = \mathbf{Z}_i\} \quad (3.29)$$

The conditional density function for the current measurement vector $\mathbf{z}(t_i)$ based on the hypothesized parameter value \mathbf{a}_j and the measurement history \mathbf{Z}_{i-1} is then

$$f_{z(t_i)|\mathbf{a}, \mathbf{Z}(t_{i-1})}(z_i | \mathbf{a}_j, \mathbf{Z}_{i-1}) = \frac{1}{(2\pi)^{1/2} |A_j(t_i)|^{1/2}} \exp\left\{-\frac{1}{2} L_j(t_i)\right\} \quad (3.30)$$

where $L_j(t_i)$ is the scalar likelihood quotient and is defined as:

$$L_j(t_i) = \frac{r_j(t_i)^2}{A_j(t_i)}. \quad (3.31)$$

When the filter model j matches the true system, the residual $r_j(t_i)$ will be zero mean with filter-computed covariance $A_j(t_i)$. The likelihood quotient will be approximately equal to the number of measurements, which is one. The filter probabilities are started out such that

$$p_j(t_i) = 1/J \quad (3.32)$$

and are then updated after each measurement incorporation by

$$p_j(t_i) = \frac{f_{z(t_i)|\mathbf{a}, \mathbf{Z}(t_{i-1})}(z_i | \mathbf{a}_j, \mathbf{Z}_{i-1}) p_j(t_{i-1})}{\sum_{j=1}^J f_{z(t_i)|\mathbf{a}, \mathbf{Z}(t_{i-1})}(z_i | \mathbf{a}_j, \mathbf{Z}_{i-1}) p_j(t_{i-1})} \quad (3.33)$$

Note that the denominator is a scaling factor to ensure that the probabilities of all the filters add up to one.

It was shown in Section 2.4.1 that the MMAE uses Bayesian blending to compute the final algorithm. However, in this research, a different approach than the Bayesian method used by the MMAE blending is used to determine the correct hypothesis. The *maximum a posteriori* (MAP) MMAE design uses the elemental filter containing the highest probability hypothesis rather than the Bayesian blending as in Equation (2.27). Because the assumption was made that ECG segment cannot be a combination of hypotheses for distinguishability purposes, the highest probability filter does make logical sense in this application. Other designs to eliminate false classifications wait to declare a hypothesis as correct until the probability is over some predefined threshold value, such as 0.5. This scheme is advantageous when many hypotheses are in the filter bank, and effectively limit the noisy probability calculation.

3.5.2. Lower Probability Bounds

As stated in Section 2.4.3, one would expect the filter probability associated with the “correct” hypothesis to increase while the other filter probabilities decrease. As shown in Equation (3.33), the conditional density function associated with $p_j(t_i)$ is scaled by the previous probability, $p_j(t_{i-1})$. A lower bound on the hypothesis probability was set to prevent any elemental filter from being eliminated from the bank and to increase the probability transition speed and hypothesis change declarations. The lower probability

bounds for each of the four discrete parameter values were set at 0.01, 0.03, 0.05, 0.10, 0.15, and 0.20 to determine the algorithm's potential. It was determined that a lower probability bound of 0.20 provided rapid probability flow and aided the MAP probability hypothesis calculation transition. Although the lower probability bound acted much like another tuning parameter, it was found that the benefit of having the lower bound set high compared to previous research was that of desirably swift hypothesis transitions.

3.5.3. Hypothesis Filter Tuning

Filter Q value tuning using the σ^2 gain parameter was performed on the 20 data sets from Table 3-1. The σ^2 tuning values are shown in Table 3-3. It should be noted here that each signal required extensive tuning. Sample ECG 5 had outstanding results in that the hypothesis probabilities correctly transitioned and identified the signal segments of interest. However, even after the extensive tuning, some signals were not segmented correctly, with the algorithm performing inadequately given samples ECG 19 and ECG 11. As shown in Table 3-3, there was not any distinct pattern in the tuning parameters.

The tuning process was limited to only changing the σ^2 value. The tuning process was iterative in that changing the σ^2 value for one hypothesis directly affected the detectability for another hypothesis. Initially, the tuning effort focused on narrowing down appropriate values to ensure that the MMAE could successfully identify the signal measurements of interest.

Table 3-3. Hypothesis σ^2 Tuning Values for Sample ECG Signals

Sample	Signal	H1--T-Wave	H2--"rest"	H3--P-Wave	H4--QRS Complex
ECG 3	1	6	0.2	6	30000
	2	21	0.1	21	30000
ECG 5	1	5	0.2	7	3000
	2	7	0.05	6	15000
ECG 11	1	20	0.6	40	20000
	2	20	0.5	20	60000
ECG 13	1	15	0.2	7.5	20000
	2	5	0.2	5	60000
ECG 19	1	10	0.2	2	30000
	2	15	0.2	5	10000
ECG 21	1	30	0.2	10	40000
	2	12	0.3	9	15000
ECG 23	1	10	0.3	15	40000
	2	40	0.2	5	60000
ECG 25	1	4	0.1	2	1500
	2	4	0.1	2	1500
ECG 27	1	6	0.2	6	30000
	2	21	0.1	21	30000
ECG 39	1	5	0.1	5	1000
	2	4	0.5	5	10000

For example, if an ECG signal segment corresponding to the QRS complex was given to the MMAE, the hypothesis corresponding to the QRS complex was tuned for adequate performance. This initial tuning was also carried out for the P-wave hypothesis and the T-wave hypothesis. However, just because adequate performance was achieved when the filter only faced one ECG segment type, this did not guarantee the MMAE performance when a whole ECG waveform was tested. Extensive tuning was then required to acquire proper probability flow between the hypotheses at the proper time.

Additional tuning techniques, such as online Q adaptation as proposed by Lund [32] and Miller [43] were investigated. The Lund algorithm seeks to tune Q adaptively to make the residuals in the different elemental filters more distinguishable from one

another. It was found that, although the algorithm performed as designed, it did not work well for this application. The Q value tuning in this application was a delicate balance of the σ^2 value for each hypothesis and the probability-flow timing. In many cases, it was required that the Q values be increased rather than decreased from the baseline hypothesis model parameters. The Lund algorithm, however, limits itself by either decreasing the Q value or leaving it unchanged. This does increase the distance between the residuals, but also makes one hypothesis perform very well compared to the other hypotheses, seemingly incapacitating the other hypotheses.

3.6 Hypothesis Determination Smoothing

The conditional probabilities can change quickly from sample to sample, especially with a high lower probability bound. While quick transitions in the probability calculation are desirable, erroneous hypothesis changes from a noisy hypothesis declaration are not desirable. It is assumed that a hypothesis cannot be valid for only a small number of samples because it is known that the segment lengths are generally longer than 5 ms. Therefore, if the MAP estimate is not constant for a set number of samples, the previous estimate is retained. If a hypothesis change takes place and does not remain at that hypothesis for more than four samples, which for a signal sampled at 500 Hz is 1 ms, the algorithm will distribute the hypothesis determination between the last constant hypothesis and the new hypothesis. This eliminates the quick jumps in the MAP output and ensures that a hypothesis declaration is smooth.

3.6.1. Hypothesis Swapping

Because the ECG signal is “pseudo-periodic,” more information is known about the signal than the algorithm is telling the MMAE, thus far. For example, it is assumed that the T-wave almost always follows the QRS complex. Following the T-wave is a “rest” period, and following the “rest” period is the P-wave. The filter can take advantage of this segment order information to help it determine when the specific segment starts and ends. The hypothesis swapping routine flow diagram is shown in Figure 3-7. Therefore, the MMAE does not need to calculate which of the four hypotheses is correct. This gives the MMAE the ability to use the event order information to narrow down which of the hypotheses is correct.

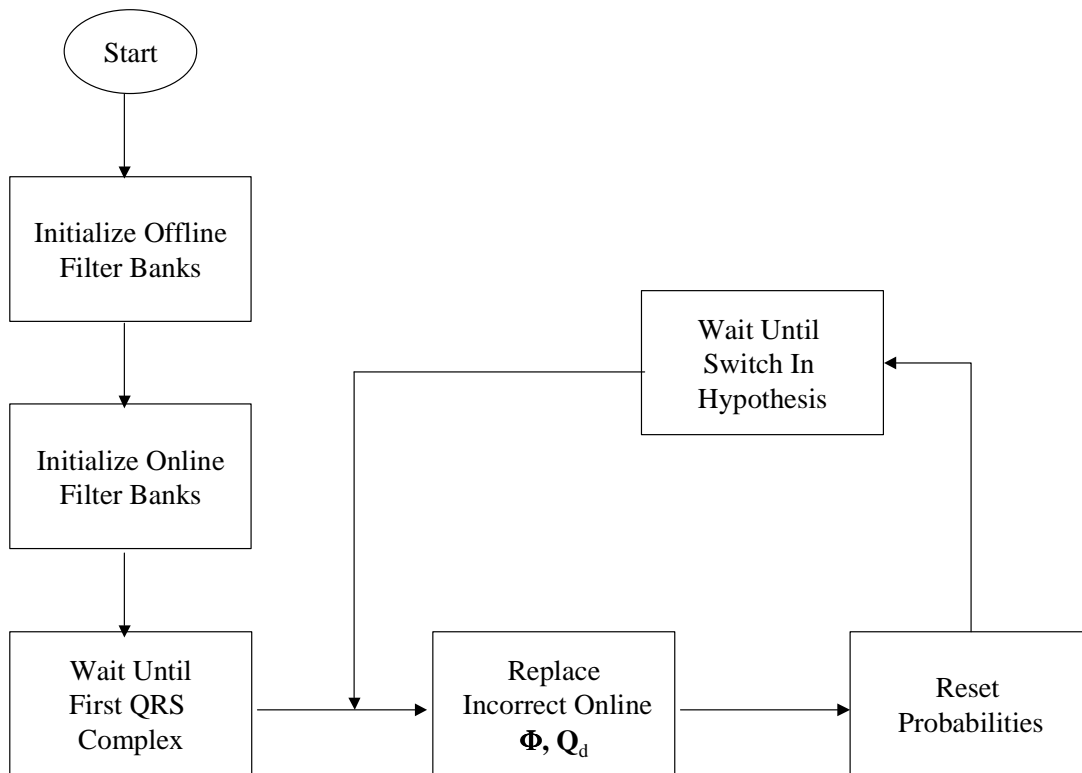


Figure 3-7. Online Hypothesis Swapping Algorithm

Once the algorithm is locked onto the QRS complex, it no longer has to distinguish between the T-wave and P-wave, which was difficult to do otherwise. The algorithm is initialized to choose between two online filters, one tuned for the QRS complex and another tuned for lower frequency and lower strength signals. The hypothesis filter parameters for the initialization bank are shown in Table 3-4.

Table 3-4. Initialization Hypothesis Filter Bank Parameters

Hypothesis	Not QRS	QRS Complex
ω_c	25	100
σ^2	50	30000
α	2	2

An offline filter bank containing hypotheses for the characteristic ECG waveform is also initialized. The online filter bank waits until the QRS complex hypothesis in filter two is detected for at least five consecutive samples. This eliminates much of the possible jitter in the probability calculation and ensures that the QRS complex hypothesis is consistent for an extended time. Once the QRS complex is declared, the correct hypothesis, the first online elemental filter's Φ and Q_d are replaced with the Φ and Q_d from the offline T-wave hypothesis. When the new hypothesis is brought online, the conditional hypothesis probabilities are reset to the lower bound for the online T-wave hypothesis and (1-lower bound) for the QRS complex hypothesis that was just declared correct. The online filters continue with the normal MMAE propagate and update cycle. These two filters remain online until the T-wave filter is declared correct for five samples in the same manner as the QRS complex was declared correct.

When the T-wave hypothesis is declared correct, the QRS complex hypothesis in online filter two is replaced with the offline "rest" period hypothesis. Again, the online

Φ and Q_d in filter two are replaced with the offline Φ and Q_d from the rest hypothesis and the conditional probabilities are reset. The MMAE then continues with the normal propagate and update cycles. This process continues, with the two hypotheses in the online filter bank at any one time being the correct hypothesis and the next expected corrected hypothesis. Thus, the hypothesis-testing algorithm never has to distinguish between four hypotheses, only two. An advantage of this type of filter swapping is that the maximum probability hypothesis from the MAP MMAE design is also the hypothesis with a probability over 0.5.

3.6.2. Hypothesis Bank Restart

The filter swapping routine can get unsynchronized with the ECG signal due to irregularities in the waveform or filter swap incorrect timing. If the filter bank is not synchronized, the QRS hypothesis will not be online at the correct time. When the QRS complex measurements are used in the MMAE, high residuals in the two online hypothesis filters will result in a high likelihood quotient, L , from Equation (3.31). An algorithm to restart the filter bank is shown in Figure 3-8. As stated in Section 3.5.1, if the hypothesis model matches the true system model, the likelihood quotient and the number of measurements will be approximately equal. Thus, if the QRS hypothesis is not online at the correct time, the filter bank can be declared out of sync if a likelihood quotient is detected above a threshold. The threshold value of 10 gives a safety margin to account for signal changes during the ECG recording, while ensuring that when the filter bank is not synchronized, a restart is declared as quickly as possible.

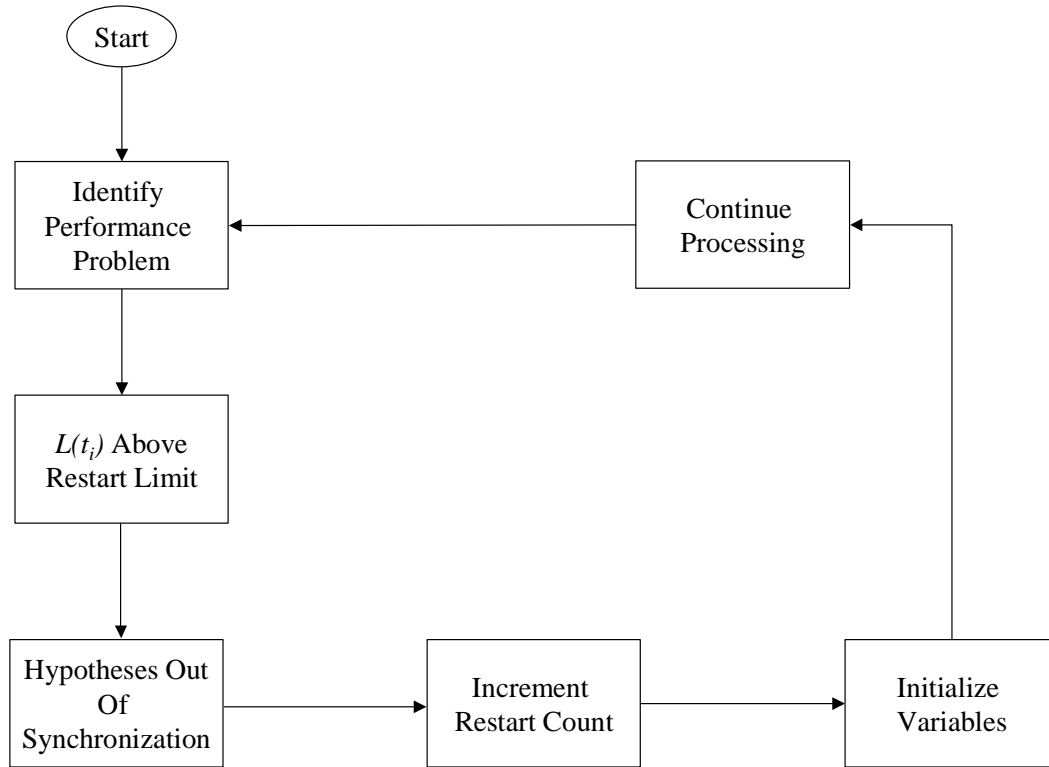


Figure 3-8. MMAE Online Restart Routine for Synchronization

When the restart is declared, the filter banks are reinitialized to the starting values and the swapping routine waits for the next QRS complex declaration to begin.

3.7 *RR, QT, and PR Interval Determination*

A correct hypothesis declaration by the MMAE effectively provides a sample segment over which the hypothesis best matches the data. This correct hypothesis restricts the sample region that an algorithm has to search over to find a specific segment area of interest. The RR, QT, and PR intervals can easily be calculated using the P-wave,

R-wave, and T-wave peaks and the correct QRS complex hypothesis start for the Q-wave. An algorithm flow diagram is shown in Figure 3-9.

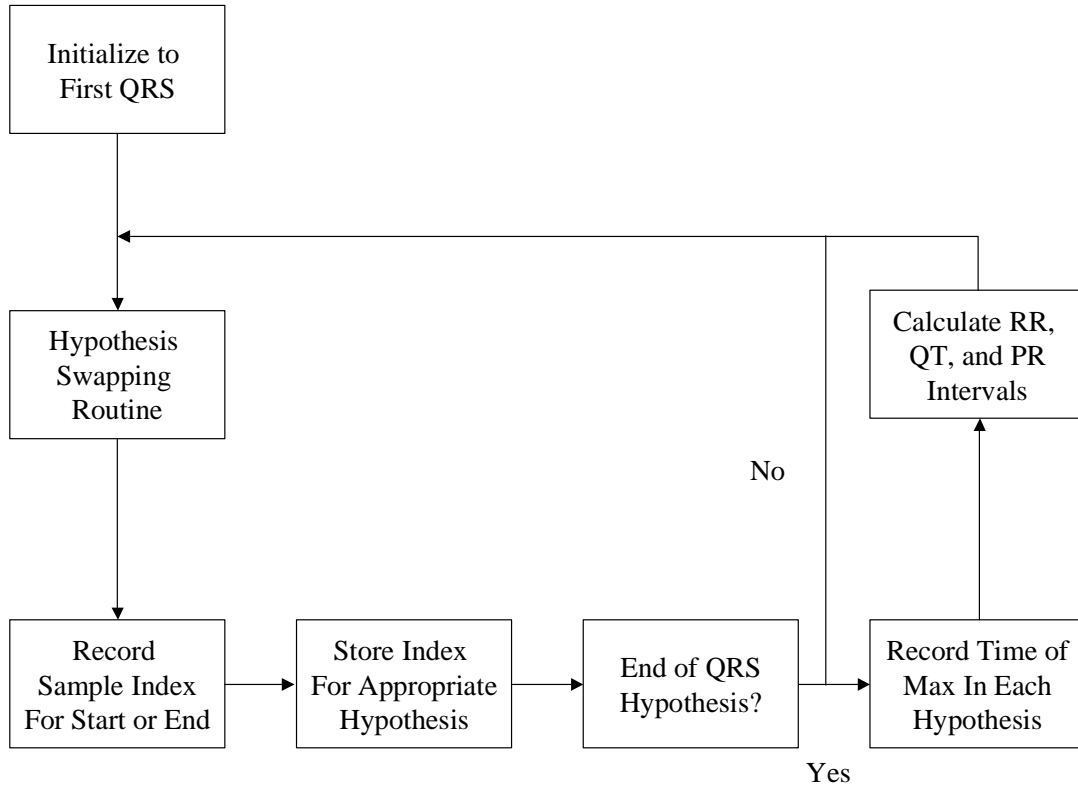


Figure 3-9. Algorithm for RR, QT, and PR Interval Determination

Exact R-wave peak time determination is aided by the correct QRS complex hypothesis declaration. Knowing where to look for the QRS complex peak (the R-wave) is greatly simplified if the search region is reduced. The algorithm does not have to worry about locking onto a tall T-wave peak as opposed to the R-wave peak. A simple maximum routine in MATLAB[®] routine looking only in the sample space of the last declared correct QRS complex hypothesis yields the QRS complex peak, the R-wave.

The difference between two successive R-peaks is the RR interval. The heart rate is given by:

$$\text{Heart Rate} = 60 / \text{RR interval} \quad (3.34)$$

Knowing the R-R interval also allows other analysis to be done, including heart rate variability analysis and inter-beat frequency analysis.

The QT interval is determined similarly to the method developed above. The Q-wave is defined as the first negative action after the P-wave. The filter hypotheses do not test for this condition, so the Q-wave is estimated to be the first correct QRS complex hypothesis sample. The T-wave is gated by a correct T-wave hypothesis declaration, restricting the T-wave maximum search space. A MATLAB[®] routine finds the maximum value and the time is noted. The QT interval is then the difference between the two times.

Finally, the PR interval is determined in a likewise manner. The P-wave search space is restricted by a correct P-wave declaration. A MATLAB[®] routine finds the maximum value in this search space. The PR interval is then the difference between the R-wave time, which is already known, and the P-wave maximum value time.

3.8 Hypothesis Model Evolution

The four hypotheses were again tuned to each data set from the MIT ECG database using the conditional probability hypothesis computation smoothing and the filter swapping algorithms. While the tuning was easier than for the first effort (Section 3.5.3), the filter bank still was inappropriately declaring a hypothesis to be correct. A

diagram describing the model evaluation and improvement process is shown in Figure 3-10.

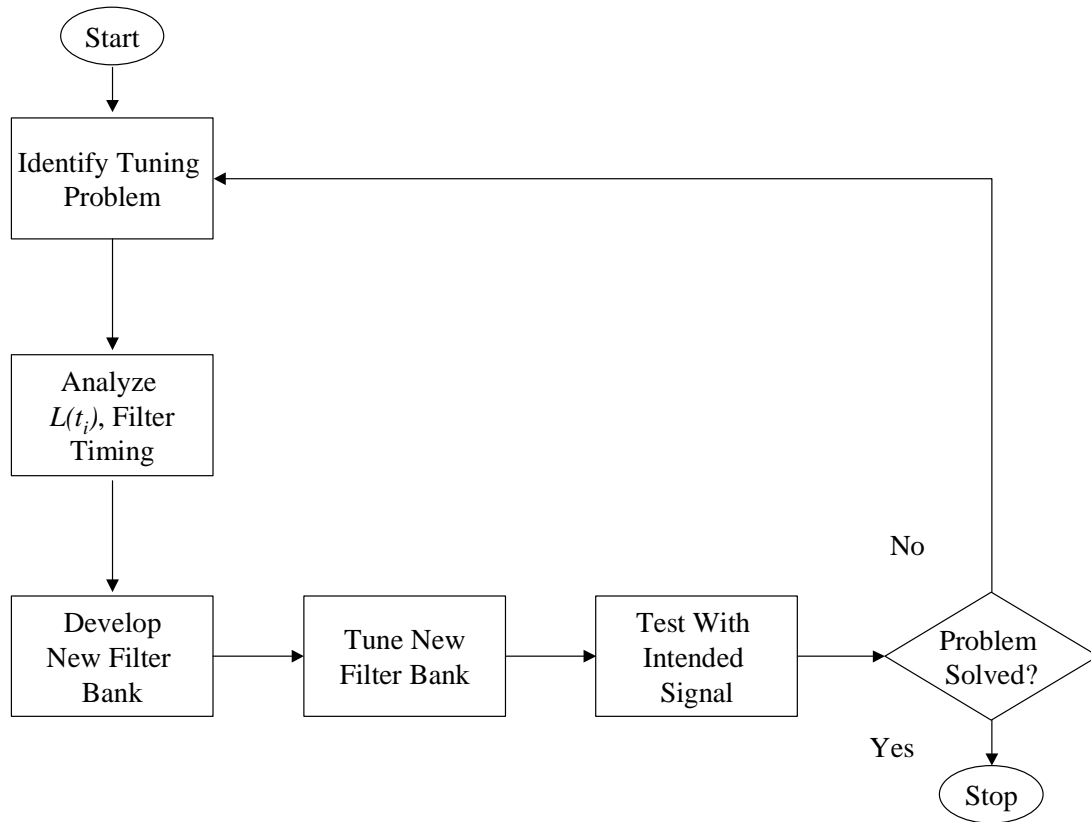


Figure 3-10. Processing of Evaluation and Developing Filter Models

The main problem area was the transition from the QRS complex to the T-wave and then the transition area between the T-wave and the P-wave. An approach similar to a target-tracking problem was then devised. In a target-tracking problem, the filter bank uses the lower frequency hypotheses when the target is not changing course rapidly [37]. However, when the target is changing course rapidly, the filter declares a higher frequency and higher noise level filter correct, and many times will declare an inappropriately high filter correct to track the maneuver.

The ECG signal was thought to be similar to the target-tracking problem. The QRS complex can essentially be approximated through a piecewise linear function with a direction change between each piece. There are also direction changes at the T-wave onset, T-wave peak, and the T-wave offset. These turns can be tracked with a higher frequency filter with a strong input driving noise so the filter can easily track the quick changes in direction. The piecewise linear functions can be tracked by a lower frequency filter and a weaker input driving noise.

Since the QRS complex has a short duration, one model was developed to track the whole complex, not the individual direction changes, noting that the filter would not give up probability quickly enough to track the individual Q-waves, R-waves, and S-waves. There was little problem tracking the QRS complex with the tuning parameters in Section 3.4.1, so only minor changes were made to this model. A model was developed to catch the transition between the QRS complex and the T-wave. This filter had a higher frequency and lower WGN strength than the QRS complex to allow distinguishability between the two hypotheses. The T-wave was next modeled by a lower frequency, lower WGN strength filter which transitioned to a higher frequency, high WGN strength filter at the direction change at the T-wave peak. The next hypothesis would be the “rest” hypothesis between the T-Wave and the P-wave, and then the P-wave hypothesis. There was not as much problem identifying the P-wave as the T-wave, so this filter required only minor modifications. It simply required a higher frequency filter with a higher WGN strength; with the noise level set to balance the transition time between the Rest hypothesis and the QRS complex hypothesis.

Finally, the QRS complex was changed to a high power, low frequency filter based on experimental results. It was found that the probabilities flowed much better between the different hypotheses if the QRS complex model took and gave back probability very stringently. When the QRS complex was more correctly modeled as a high frequency, high strength signal, the QRS complex hypothesis tended to keep probability too long or take probability too soon. Again, to summarize the changes: the T-wave was modeled by three separate hypotheses to account for direction changes at the T-wave onset and the T-wave peak. The P-wave hypothesis parameters were set to balance the transition times between the “Rest” hypothesis and the QRS complex hypothesis. Table 3-5 shows the modified filter bank parameters.

Table 3-5. New Hypothesis Filter Bank Parameters

Hypothesis	QRS Complex	T-Wave	“Rest”	P-Wave
ω_c	100	100, 10, 100	10	100
σ^2	30000	50, 0.5, 50	0.5	30
α	2	2, 2, 2	2	2

3.9 Changing Heart Rate and Changing Physiological Condition

The animal exsanguination data from Qualia Computing, Inc. [1] provided a special challenge not seen in the MIT ECG data files. The heart rate increased as time went on, the signal waveforms change shape, the T-wave changed location, and the signal strength decreased dramatically. Two additional MMAE filter banks were created and the ability to switch to a new bank was created using the process described in the previous section, Section 3.8. The new filter banks were very similar to the original filter banks with the only changes residing in tuning the filter bank to a particular signal

section. For example, the filter banks in Table 3-5 worked well until the signal strength dropped low enough essentially to incapacitate the conditional hypothesis computation algorithm. The high input WGN strength made the residuals look good for the whole waveform, not allowing the MMAE to change filters. Lower input WGN strengths for each hypothesis and a switch to the new filter banks at the proper time allowed the MMAE ECG processing algorithm to continue functioning properly. Table 3-6 and Table 3-7 show the parameters for filter banks two and three.

Table 3-6. Alternative Hypothesis Filter Bank Parameters, Bank 2

Hypothesis	QRS Complex	T-Wave	“Rest”	P-Wave
ω_c	100	100, 10, 100	10	100
σ^2	15000	20, 0.7, 20	0.7	15
α	2	2, 2, 2	2	2

Table 3-7. Alternative Hypothesis Filter Bank Parameters, Bank 3

Hypothesis	QRS Complex	T-Wave	“Rest”	P-Wave
ω_c	100	100, 10, 100	10	100
σ^2	5000	5, 1, 5	0.7	10
α	2	2, 2, 2	2	2

Tuning banks two and three was performed in the same manner as in Section 3.5.3. The QRS complex hypothesis WGN input was tuned such that the likelihood quotient, $L_j(t_i)$, was approximately four. Again, this is tighter tuning than would normally be performed, remembering that $L_j(t_i)$ is approximately the number of measurements with conservative tuning. The other filter hypotheses’ WGN values were also reduced based on the hypothesis calculation transitions.

In addition, the MMAE banks were switched based on heart rate. When the heart rate was above 165 beats per minute (BPM), filter bank two switched into the offline

filter bank and was used in the hypothesis-swapping algorithm. A flow diagram of the switch is shown in Figure 3-11.

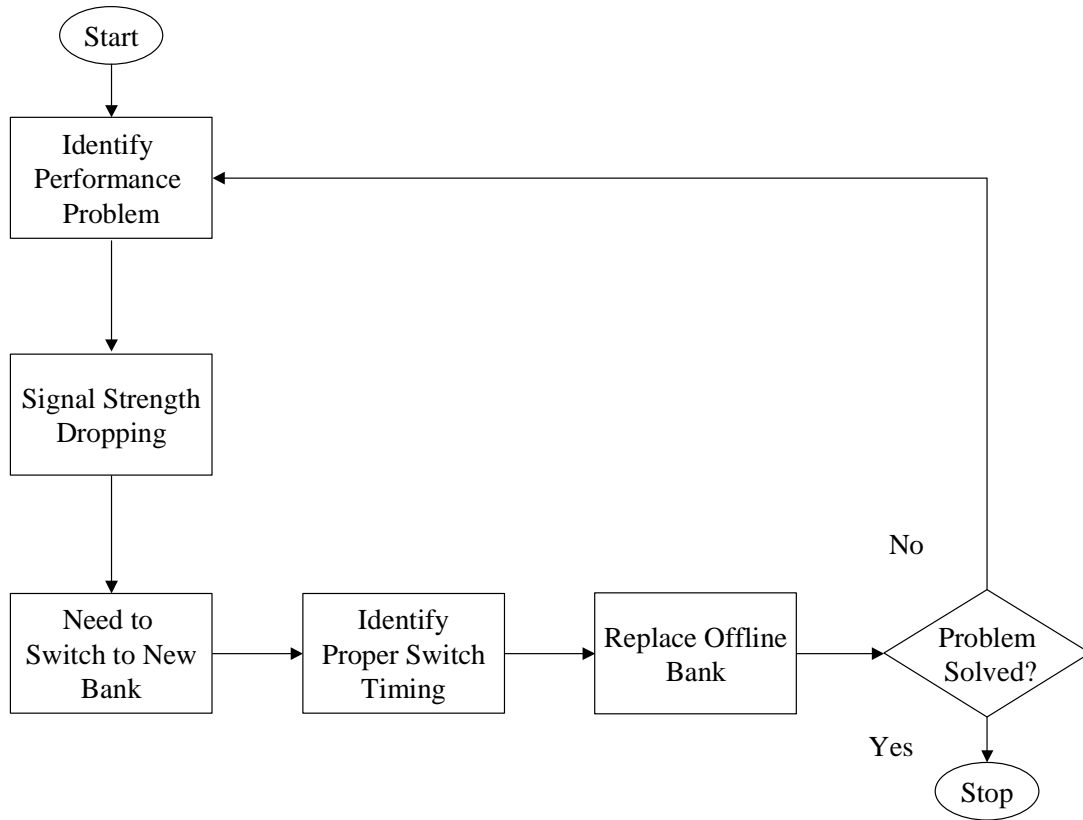


Figure 3-11. Offline Filter Bank Switch Algorithm

The proper time to switch the offline filter banks was based on the heart rate. While this may not always be the case for every signal, it proved very effective for the animal exsanguination data. The MMAE ECG processing algorithm then worked in the same manner, except that the filters being swapped in and out of the online hypotheses were from filter bank two instead of filter bank one. When the heart rate was above 195 BPM, filter bank three was brought online.

The additional offline filter banks allow for an increase in the algorithm's robustness because an algorithm can be created to take advantage of both the restart routine and the offline filter bank switch routine. If a signal has characteristics that do not fit the first online filter bank, the algorithm will restart several times. Thus, this is another method to determine the proper offline filter bank switch timing, as shown in Figure 3-12.

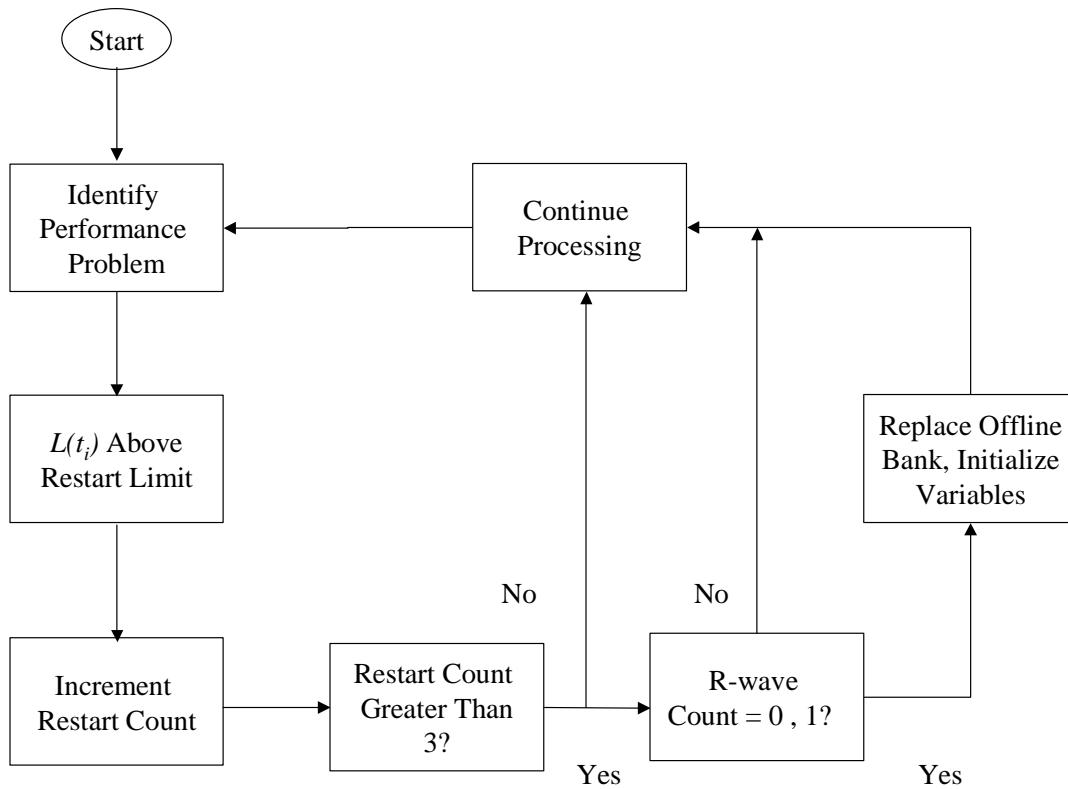


Figure 3-12. Algorithm Initialization Restart Flow Diagram

The filter bank starts with bank one and uses the restart algorithm to choose when to try the next filter bank. If the difference between the number of restarts and the number of R-waves detected is two or three, the next filter bank is used in the swapping

routine. This means that if the signal does not initially match the hypotheses in filter bank one, several restarts will occur. The MMAE was given a chance to synchronize the filter banks with the signal. When three restarts happen in a row, filter bank one was switched to filter bank two. All variables were reinitialized, including the number of restarts and the number of R-waves detected. If the signal did not match the hypotheses in filter bank two, three restarts in a row happened again and bank two was switched out for bank three. All variables were again reinitialized and the algorithm starts over.

3.10 Overall MMAE ECG Processing Algorithm Description

The overall MMAE ECG processing algorithm is depicted in the flow diagram shown in Figure 3-13. Following the path through the diagram, first the MMAE is initialized as outlined in the initialization and restart routine. Once the filter banks are synchronized with the signal, the MMAE begins the overall propagate and update routine. Every sample is checked by the restart routine to ensure that the online filters are synchronized with the signal. If a restart is needed, the restart routine is followed. Next, the hypothesis swapping routine checks if the online filter hypotheses need to be swapped with offline hypotheses. If a swap is needed, the interval calculation routine is run; if not, the algorithm continues processing data.

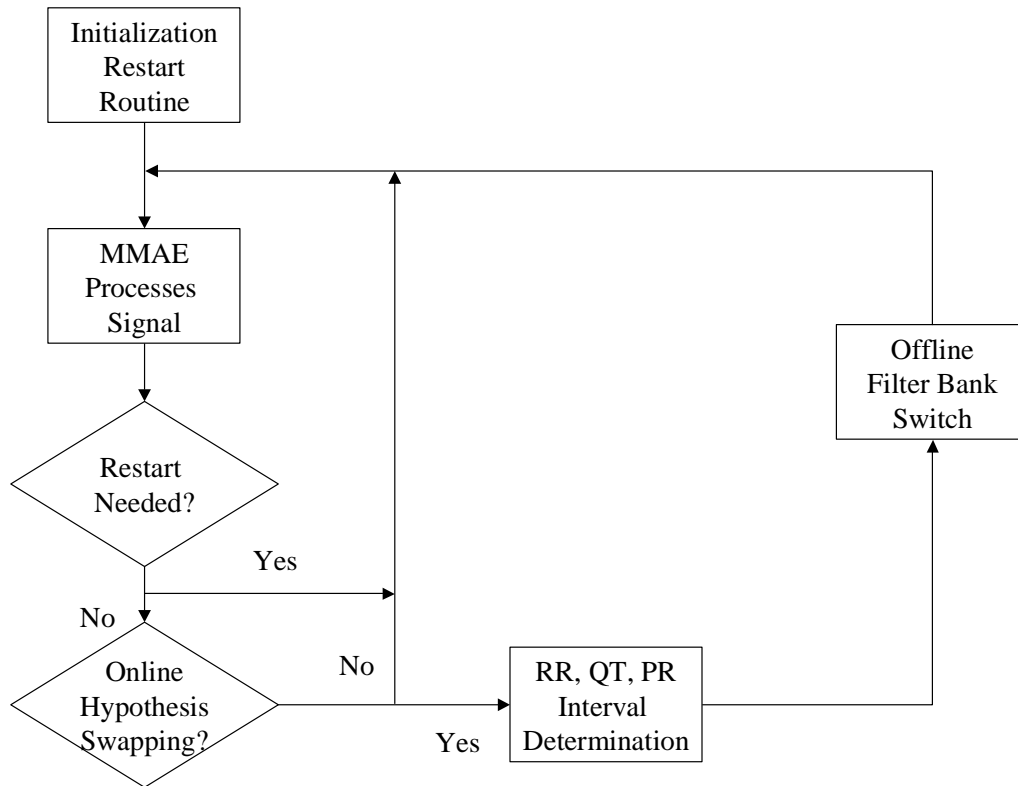


Figure 3-13. MMAE ECG Processing Flow Chart with Subroutines

After the intervals are calculated, the offline filter bank switching routine is used to check if offline filter banks can better match the signal measurements. The algorithm continues processing ECG data until the signal end.

3.11 Summary

This chapter looked at the overall algorithm description. It gave the iterative process for developing the ECG processing algorithm. The algorithm development flow diagram was used to develop and evaluate the MMAE hypothesis models methodically. First, time domain and frequency domain signal processing techniques were used to

develop a mathematical signal model and its individual characteristic segments. A transfer function was developed to approximate the signal segments' first derivatives' power spectral density estimates. An MMAE was used in a parameter estimation scheme to determine which hypothesis was correct. The Bayesian MMAE algorithm was changed to the MAP implementation. The hypotheses were then paired down to two from the possible four hypotheses taking advantage of the segment order information. The T-wave model was changed from one hypothesis model to a set of three sequential hypotheses to help the MMAE track the T-wave better than the first filter bank. Two new filters banks were also developed, each with lower WGN input strengths. In addition, a heart rate determination algorithm was developed based on the knowledge of when the QRS complex hypothesis is correct. Finally, a filter bank-switching algorithm was developed based on heart rate. Chapter 4 will give the MMAE ECG processing algorithm test results.

4. Analysis of Results

4.1 Overview

This chapter analyzes the MMAE ECG processing algorithm using actual ECG signals. The algorithm is tested using 20 signals from the MIT ECG database and 120 minutes of ECG data from an animal exsanguination. The analysis focused on: (1) the algorithm's ability to stay synchronized with the signal, (2) the P-wave, R-wave, and T-wave peak accuracies, and (3) the types of signals that this algorithm did and did not process well. The signals challenged the MMAE because they did not always match the characteristic ECG waveform model. The major cause for model discrepancies was due to ECG lead placements on the body. The following sections will analyze several representative examples, including successful performance with detailed analysis of why the algorithm performed well. Furthermore, a representative example indicating poor performance is included in the analysis with an explanation as to why the MMAE did not perform well under sub-optimal conditions. Finally, the animal exsanguination ECG data is analyzed in detail to show the MMAE's performance in a real-world life-threatening situation. Figures for all signals analyzed in this research are found in Appendix A.

4.2 MIT ECG Signal Analysis

The MMAE ECG processing algorithm was used to analyze 20 ECG signals obtained from the MIT ECG database and used in the system model development in Chapter 3. The algorithm's ability to detect the R-waves accurately and to determine the heart rate was first analyzed. The R-wave detection accuracy was defined as follows:

$$Accuracy = \frac{R\text{-wave}}{R\text{-wave} + \text{Restart}} \quad (4.1)$$

where

R-wave = number of R-waves detected correctly

Restart = number of restarts during the processing

The accuracy measured how well the algorithm determined the QRS complex location. It was penalized for restarts and was penalized for missed R-waves. For example, if the algorithm quickly restarted itself, it may have had several restarts but missed few R-waves. Conversely, if the algorithm has had many restarts and detected few R-waves, it had a low score. It was found that even though the MMAE algorithm restarted when required, it never incorrectly identified an R-wave and failed to restart. Thus, the R-wave count contains only true R-wave peaks, not T-wave or P-wave peaks that may be identified before a restart. Therefore, the heart rate plot contains no intervals where the R-wave peak may have been incorrectly identified.

The algorithm hinged on correctly finding the QRS complex, restarting the algorithm if it did not, and calculating the QT and the PR intervals when possible. Note that the algorithm scored above 0.90 for 14 out of 20 signals with 8 perfect runs, and scored below 0.50 two times. The algorithm scoring is shown in Table 4-1, clearly showing the measurement lead effect on the MMAE algorithm's performance. Typically, the algorithm scored well when the signal was from lead V4, but did not score well when the signal was from lead III. This accuracy score was very important to the MMAE algorithm's performance analysis.

Table 4-1. MMAE ECG Processing Algorithm Scoring

Sample	Signal	R-Wave Detected	Restarts	Accuracy	Lead
ECG 3	1	55	2	96.49%	V4
	2	16	29	35.56%	MLIII
ECG 5	1	52	0	100.00%	V4
	2	19	17	52.78%	MLIII
ECG 11	1	53	35	60.23%	MLIII
	2	56	1	98.25%	V4
ECG 13	1	9	40	18.37%	MLIII
	2	60	0	100.00%	V4
ECG 19	1	57	0	100.00%	V4
	2	56	8	87.50%	MIII
ECG 21	1	72	0	100.00%	V4
	2	66	6	91.67%	MLIII
ECG 23	1	70	4	94.59%	V4
	2	70	4	94.59%	MLIII
ECG 25	1	68	0	100.00%	V4
	2	67	0	100.00%	MLIII
ECG 27	1	69	0	100.00%	V4
	2	66	0	100.00%	MLIII
ECG 39	1	66	29	69.47%	MLIII
	2	74	3	96.10%	V4

Clearly, the algorithm scored well when the ECG lead placement measured all events in the characteristic ECG waveform. In the following sections, three sample signals will be analyzed.

4.2.1. Sample ECG 3 Signal 1 and Other Fine Performance Examples

ECG 3 was from modified Lead III and Lead V4 (a chest lead rather than a limb lead, as discussed in Chapter 2). This sample clearly shows the MMAE algorithm's good and bad performance throughout the ECG sample. Signal 1 from lead V4 followed the characteristic ECG waveform as expected by the MMAE. The processed results are shown in Figure 4-1 through Figure 4-5. Figure 4-1 shows the ECG signal with the MAP

hypothesis overlaid. The hypotheses are strictly a one or two, corresponding to the online hypothesis filter number. Note that the hypotheses were brought online according to the swapping method outlined in Chapter 3.

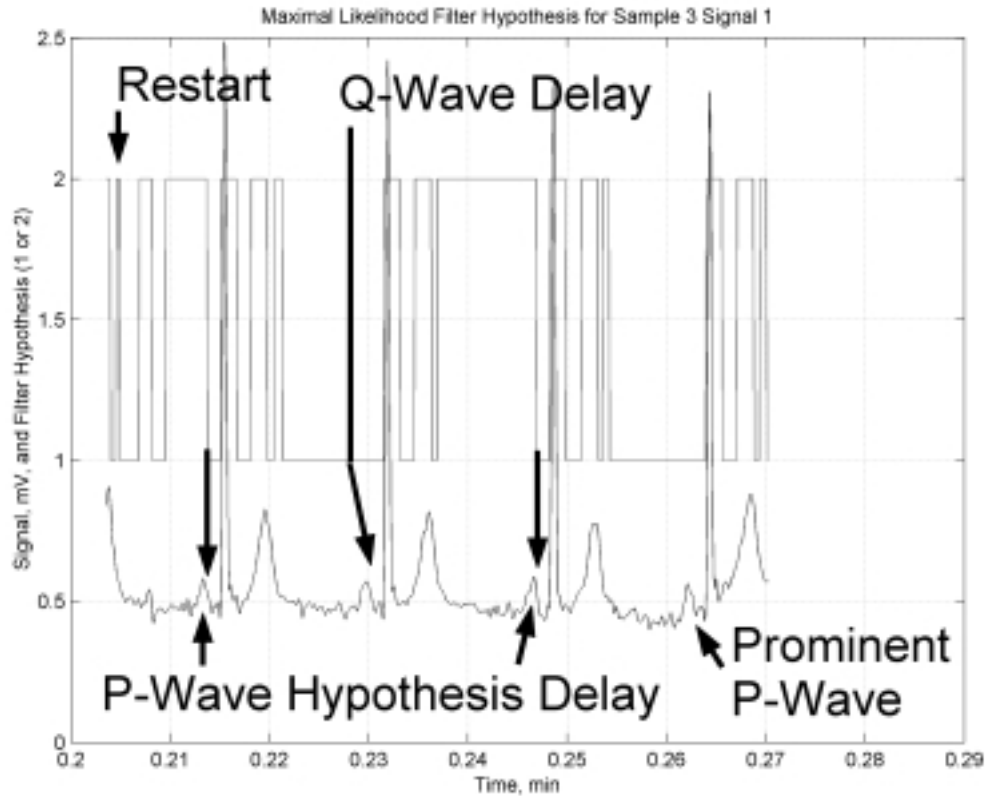


Figure 4-1. Maximal Likelihood Filter Hypothesis for Sample 3 Signal 1

The hypothesis swapping, as demonstrated Figure 4-1, worked well except for the cases noted where the P-wave hypothesis was declared correct after the peak of the P-wave. The restart algorithm's performance worked well, as shown by the restart declared at 0.204 minutes and the algorithm accurately locked onto the next QRS complex. The restart was declared because the low frequency filter did not match the positive slope to negative slope change well and the scalar likelihood quotient went above the pre-specified restart value of 10. While a higher restart value would have allowed the

MMAE to continue with the hypothesis swapping without the restart, the filter bank synchronized itself perfectly with the next QRS complex. The first hypothesis filter caught the transition between the S-wave and the T-wave, the second T-wave filter caught the rise of the T-wave, and the third T-wave filter was declared to be correct right after the T-wave peak. The filter then switched to a low frequency and low power hypothesis, and changed to the P-wave hypothesis at the T-wave offset. The MMAE waited until the QRS complex was declared correct to take the P-wave filter offline and brought the first T-wave filter back online.

The R-wave was consistently identified, yielding a well-formed heart rate plot as shown in Figure 4-2.

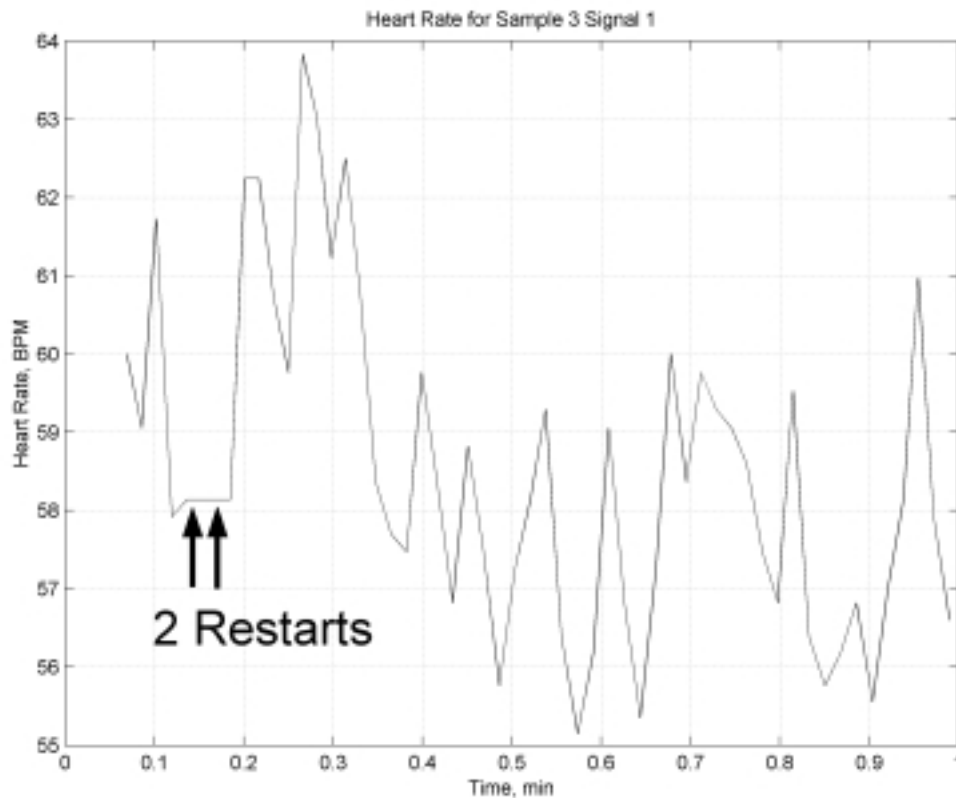


Figure 4-2. ECG Sample 3 Signal 1 Heart Rate

Note that the region between 0.15 to 0.20 minutes is caused by the two restarts. The MMAE algorithm also identified the QT interval accurately. The corrected QT interval, QTc, is a standard QT interval normalization method [4]. The QT interval was normalized based on heart rate, as shown in Equation (4.2).

$$QTc = \frac{QT}{\sqrt{RR}} \quad (4.2)$$

The QTc interval is typically 0.40 sec [29]. The results of the QT interval and the QTc processing are shown in Figure 4-3 and Figure 4-4.

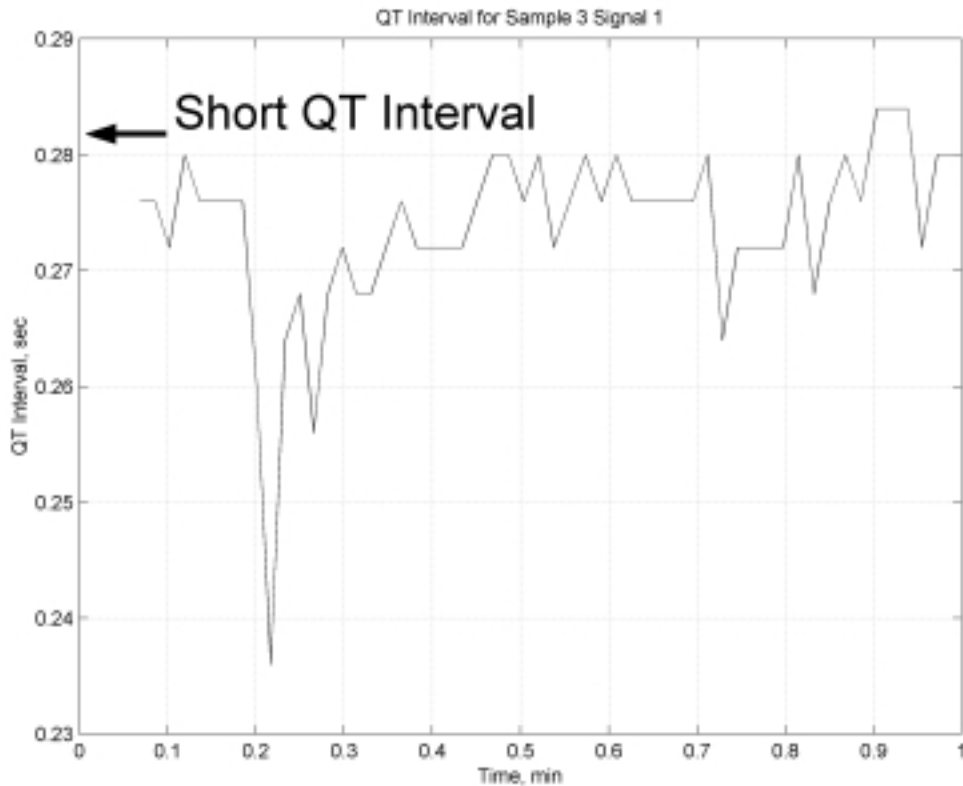


Figure 4-3. ECG Sample 3 Signal 1 QT Interval

The short interval was caused in part by the Q-wave timing determination. The first time epoch when the QRS complex hypothesis was declared correct was stored as

the Q-wave time. Visual Q-wave analysis showed that the declaration was approximately 0.01 seconds late. While this did not account for the 0.10 seconds difference between the average QTc interval and the QTc interval shown in Figure 4-3 and Figure 4-4, it did reveal a small error in the determination of the exact Q-wave time. The QTc was consistently short for all cases. In all signals, the QT interval was 0.01-0.05 seconds short because the QRS complex declaration actually occurred at the R-wave onset. However, if the QRS complex declaration is consistently a set number of samples late, it is plausible to simply declare the Q-wave the proper number of samples early.

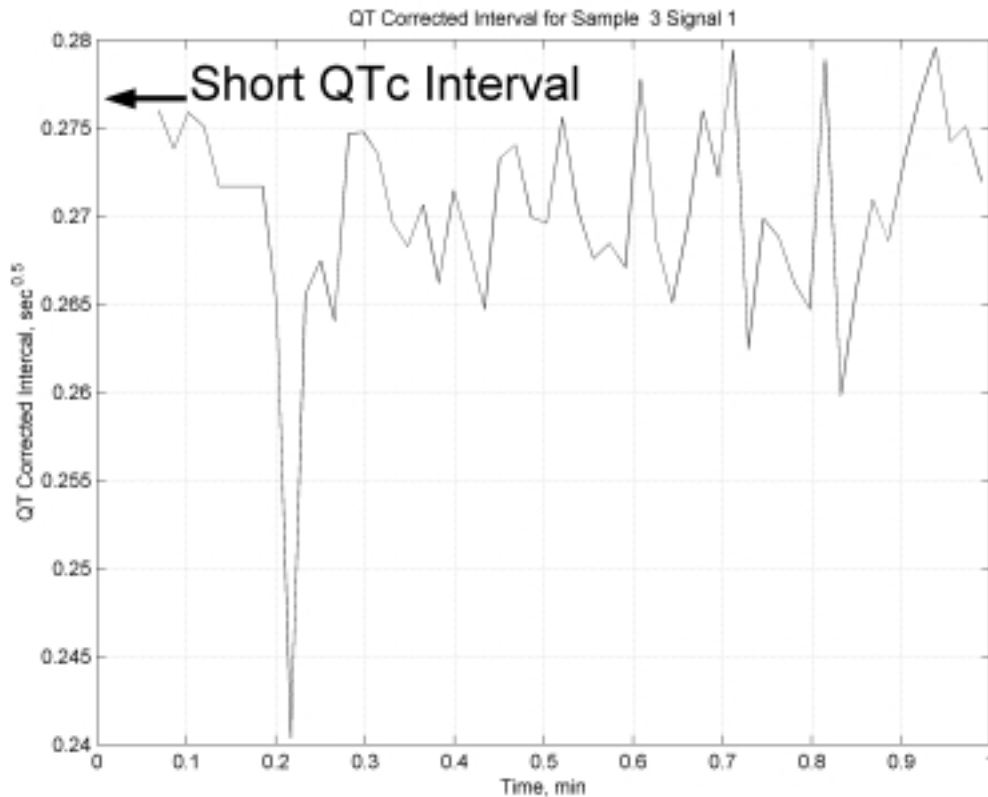


Figure 4-4. ECG Sample 3 Signal 1 QTc Interval

The PR interval was found accurately for all but five intervals, as shown in Figure 4-5. These intervals, two of which are shown in Figure 4-5 at 0.21 and 0.25 min, were

approximately 0.02 seconds shorter than the true PR interval. This shortening was due to P-wave hypothesis being declared correct after the P-wave peak had occurred. Note the shortening effects on the interval as shown in Figure 4-5 with the sharp negative dips occurring at 0.13, 0.21, 0.25, 0.65, and 0.89 min.

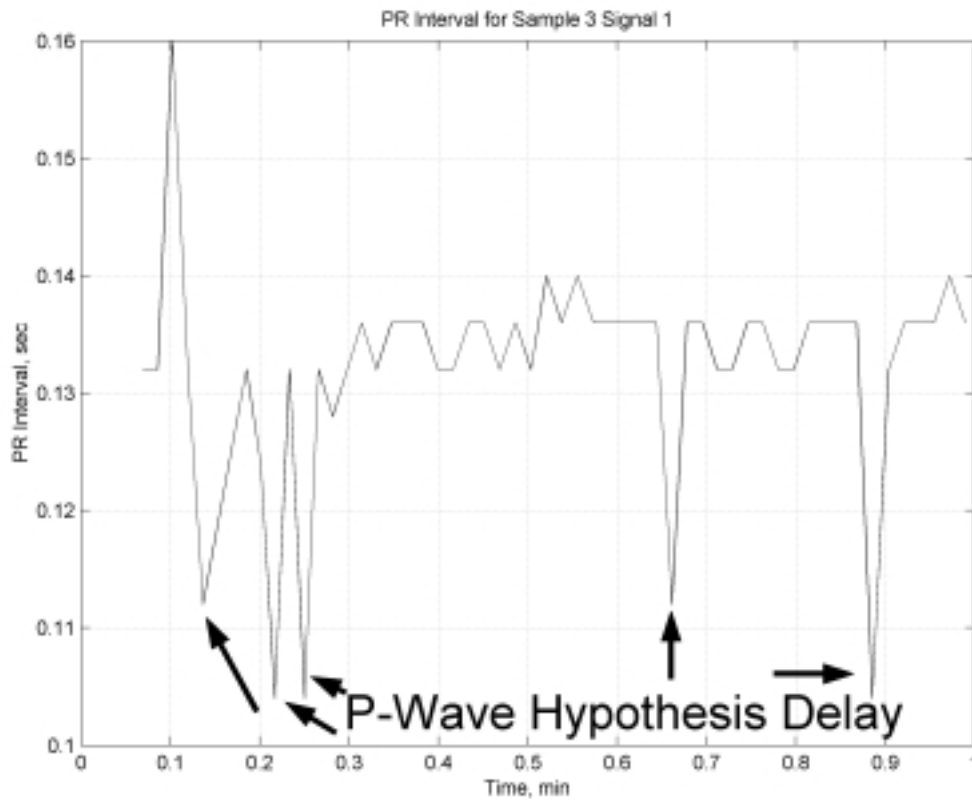


Figure 4-5. ECG Sample 3 Signal 1 PR Interval

The PR interval was short in other signals as well. A QT and PR interval summary is shown in Table 4-2. Note that ECG 3 signal 2, ECG 5 signal 2, ECG 11 signal 1, and ECG 13 signal 1 were not analyzed because their QRS complex detection accuracy was below 0.60. Recall that the MMAE algorithm hinges on correctly identifying the distinct QRS complex. Therefore, it was not useful to evaluate the

accuracy of the subsequently determined intervals if this most important first interval was not determined correctly. Note in Table 4-2 that the QT and PR interval accuracies were not analyzed if the signal did not have an accuracy score over 0.60, signified by the “N/A” designation.

Table 4-2. QT and PR Interval Accuracy for Accurately Detected R-wave

Sample	Signal	Q-Wave Delay	P-Wave Delay	P-Wave Detected	Late Declaration	Accuracy
ECG 3	1	0.01	0.025	55	5	91.67%
	2	N/A	N/A	N/A	N/A	N/A
ECG 5	1	0.025	-0.40	52	52	50.00%
	2	N/A	N/A	N/A	N/A	N/A
ECG 11	1	N/A	N/A	N/A	N/A	N/A
	2	0.02	0.01	56	16	77.78%
ECG 13	1	N/A	N/A	N/A	N/A	N/A
	2	0.015	0	60	0	100.00%
ECG 19	1	0.015	0	57	0	100.00%
	2	0.035	0.01	56	16	77.78%
ECG 21	1	0.02	0	72	0	100.00%
	2	0.025	0.01	66	32	67.35%
ECG 23	1	0.02	0.025	70	23	75.27%
	2	0.05	0	70	0	100.00%
ECG 25	1	0.015	0.03	68	18	79.07%
	2	0.03	0	67	0	100.00%
ECG 27	1	0.03	0.03	69	69	50.00%
	2	0.02	0	66	0	100.00%
ECG 39	1	0.04	0.2	66	66	50.00%
	2	0.03	0.03	74	74	50.00%

Every signal has a delay in the QRS complex declaration, which results in a Q-wave timing accuracy delay. Every signal except ECG 5 and ECG 39 had at least one lead for which the R-waves and the P-waves were found accurately. ECG 5 was a very good signal overall; however, in signal 1 the very prominent U-wave had a higher peak than the P-wave, accounting for the corresponding -0.40 sec P-wave declaration inaccuracy. ECG 39 had other abnormalities that caused the algorithm to find the P-wave peak incorrectly and will be discussed in Section 4.2.2.

Individual filter tuning would allow the P-waves peaks in ECG 5 signal 1, ECG 39 signal 2, and ECG 27 signal 1 to be found correctly. The P-wave hypothesis in these signals was consistently declared to be correct after the P-wave peak. While it may not be realistic to tune a filter to every signal in real-time, this may be applicable to post-processing ECG data. The tuning would be very slight and easy to accomplish, given that the R-wave performance was already very good and that the P-wave hypothesis was simply declared late. An online Q adaptation algorithm may also solve this problem. This algorithm would recognize that the intervals are most likely in a specified time range, assuming that the signal contains no arrhythmias or other irregularities. If the calculated interval is not in the proper range, the Q can be modified to improve performance.

4.2.2. Sample ECG 3 Signal 2 and Other Examples of Poor Performance

The ECG Sample 3 Signal 2 characteristics were very different from those of Signal 1, as shown in Figure 4-6. The modified Lead III signal had no QRS complex from the characteristic waveform. The R-wave was not present, slowing the center frequency of the QRS complex down because there was one fewer wave. Additionally, the T-wave was inverted and the algorithm was expecting a positive wave. The T-wave and the P-wave were lower in amplitude than in Signal 1, with the P-wave buried in the noise during the rest section. This noise causes severe problems for the hypothesis-swapping algorithm. Consequently, the accuracy score for Signal 2 was the second lowest compared to all other accuracy scores. The reason for the problems with the MMAE algorithm was very simple: the hypothesis banks did not model the signal well.

As stated in Chapter 2, when a hypothesis does not model the true system well, the performance of the algorithm is poor. Figure 4-6, Figure 4-7, Figure 4-8, and Figure 4-9 show the algorithm performance for a signal that contained waveforms not hypothesized in the filter bank. Note the restart at 0.23 minutes and the generally poor hypothesis swapping performance in Figure 4-6.

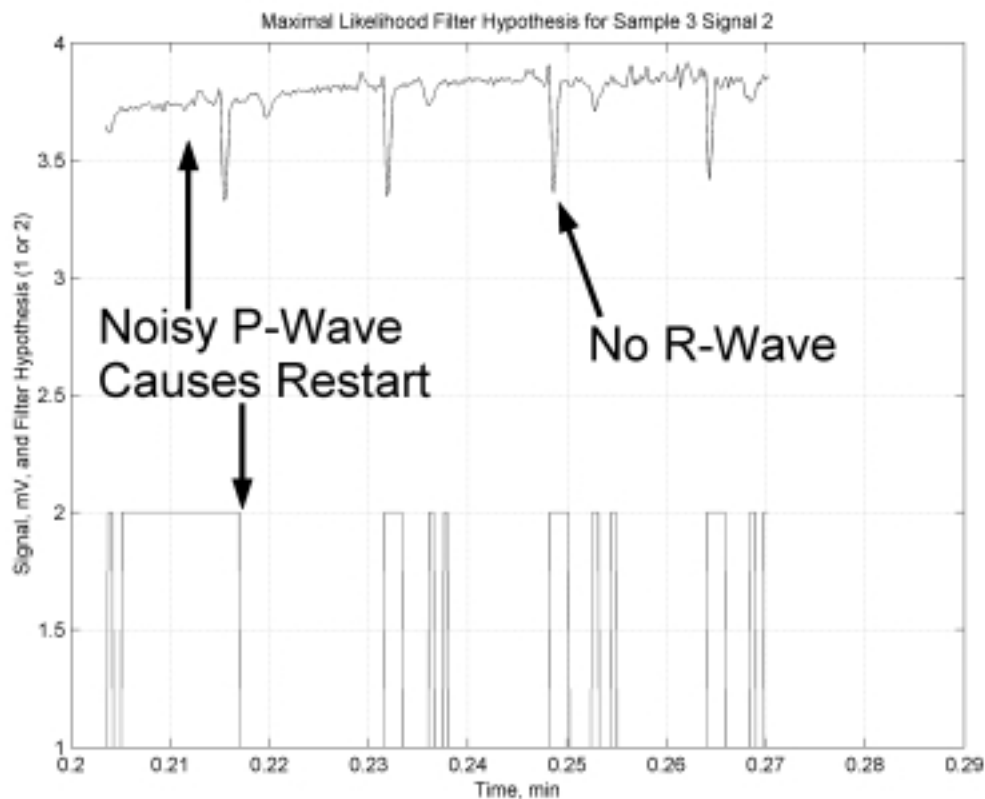


Figure 4-6. Maximal Likelihood Filter Hypothesis for Sample 3 Signal 2

The ECG 3 signal 2 shown in Figure 4-6 reveals other conditions in the signal that the algorithm cannot handle. There was no positive deflection after the Q-wave, making the QRS complex actually a QS complex. The algorithm identified the maximum value in the sample region where the QRS hypothesis was declared correct as opposed to a

wave minimum. Additionally the T-wave had a negative deflection as opposed to the characteristic positive deflection from the baseline. Again, the algorithm looks for the maximum in the sample area where the T-wave hypothesis was declared correct. Additional logic improvements in the MMAE algorithm can find the QS complex minimum and the T-wave minimum when necessary, as opposed to strictly finding a wave's maximum. Additionally, the algorithm could be improved by developing a hypothesis that recognizes when the P-wave is buried in noise, allowing the MMAE to continue processing the signal correctly.

Figure 4-7 shows the heart rate from modified Lead III. Compared to Figure 4-2, the information is not as dense, although it does give a heart rate indication.

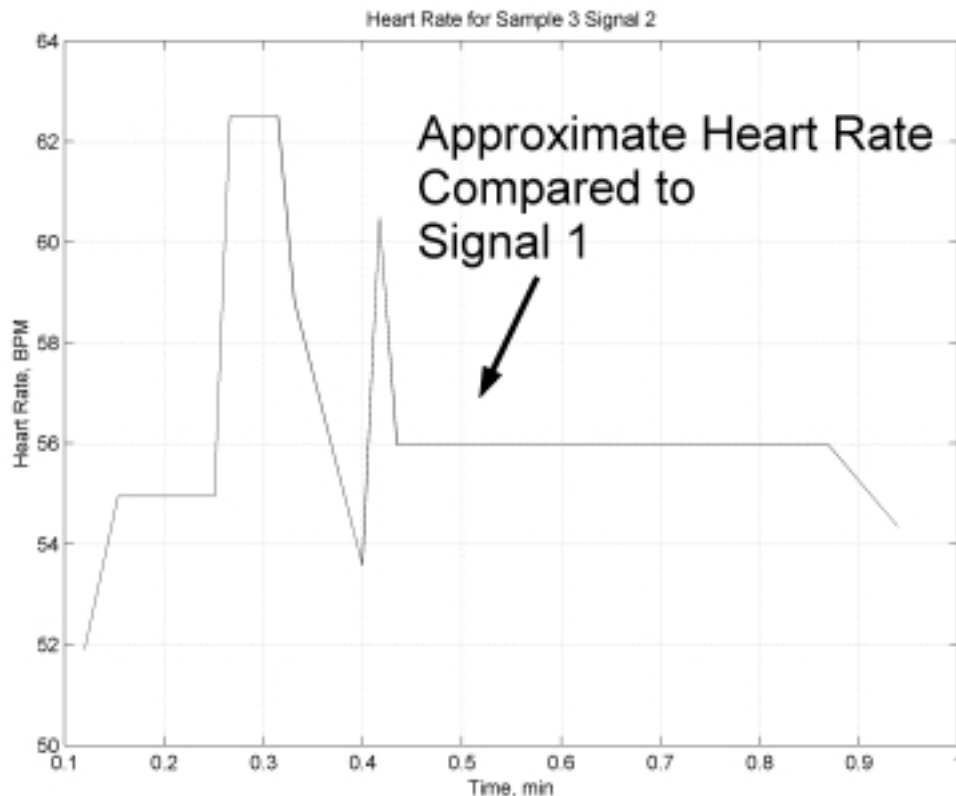


Figure 4-7. ECG Sample 3 Signal 2 Heart Rate

The heart rate from Signal 2 was also accurate compared to that of Signal 1, meaning that it provides a rough but not precise heart rate indication at 56 BPM compared to the 55-60 BPM shown in Figure 4-2. The QT and QTc intervals from Signal 2 compare similarly to those from Signal 1. The information contained in the algorithm output for the one-minute period provided a rough QT interval indication, as shown in Figure 4-8.

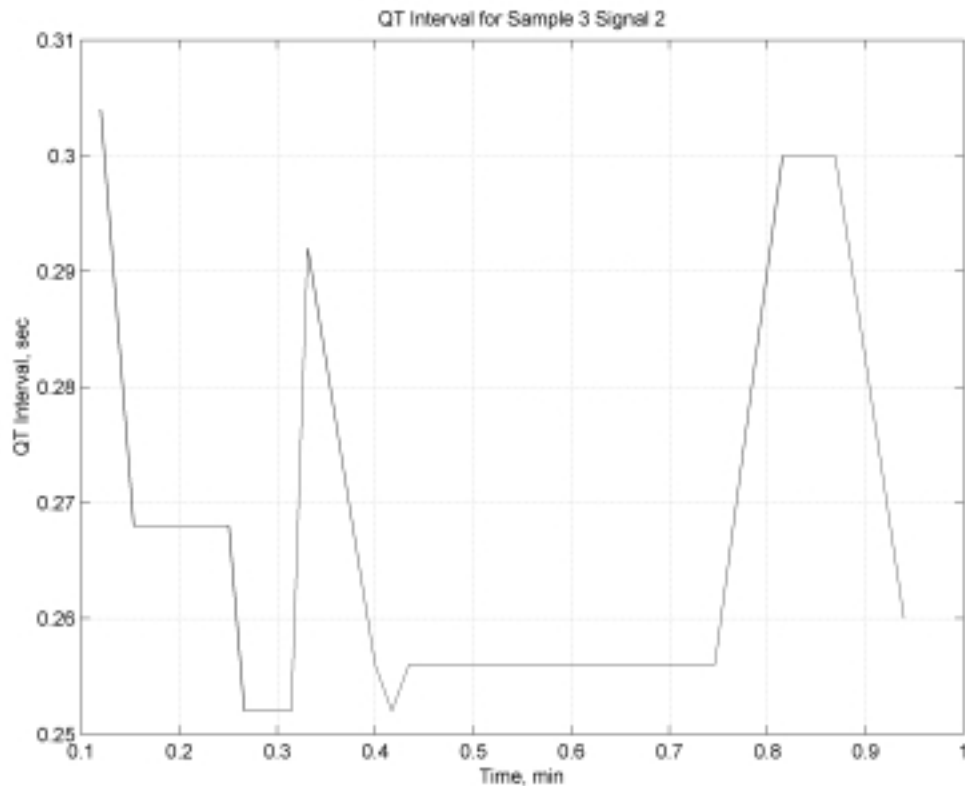


Figure 4-8. ECG Sample 3 Signal 2 QT Interval

When the QRS complex was correctly identified, the subsequent intervals could also be determined. Thus, the QT interval plot followed a similar profile to the heart rate plot. During signal sections where the QRS complex was not correctly identified, the QT plot showed a similar information shortage.

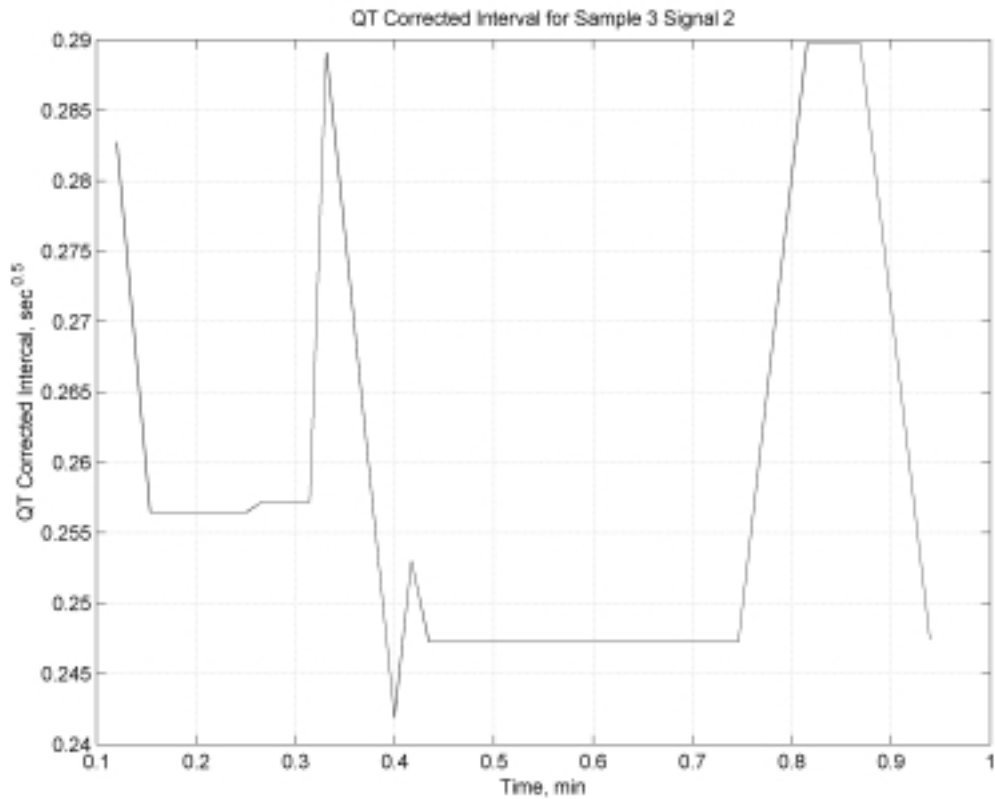


Figure 4-9. ECG Sample 3 Signal 2 QTc Interval

Figure 4-8 through Figure 4-10 clearly demonstrated that, if the QRS complex (and thus the heart rate) was not correctly identified by the algorithm, the QT and PR intervals were not found correctly. As a result, the QT and QTc plots contained the same low information density as the heart rate plots.

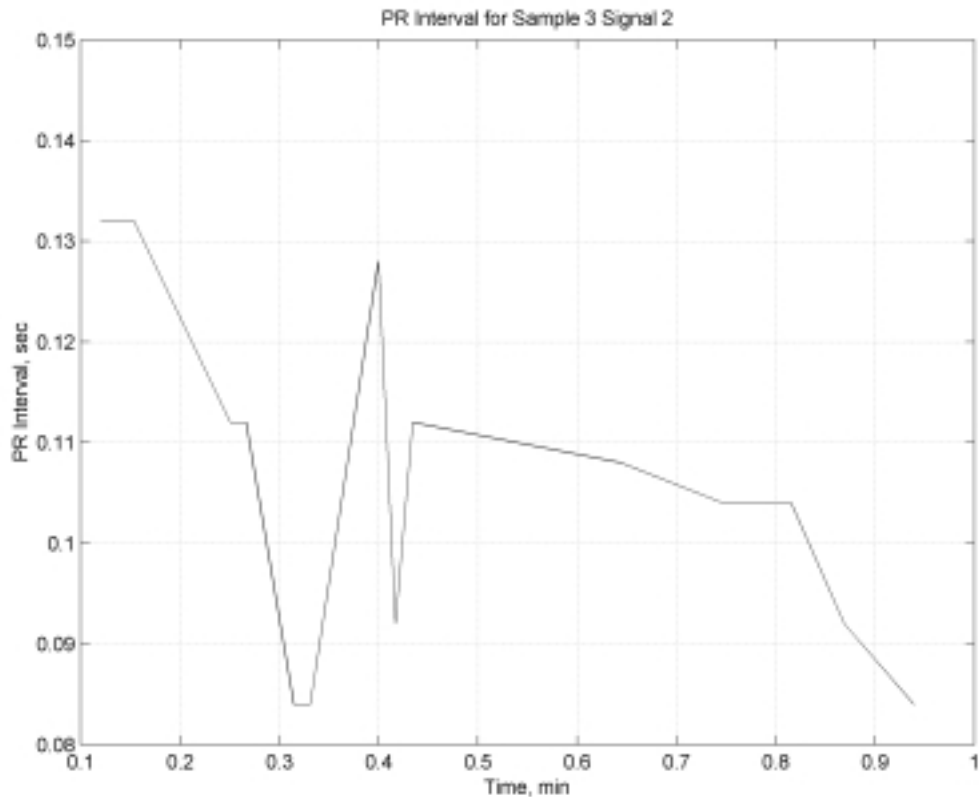


Figure 4-10. ECG 3 Signal 2 PR Interval

Signal and maximal probability analysis revealed why the MMAE algorithm did not process this signal well. The P-wave signal strength was almost indistinguishable from the noise in the signal between the R-waves. In addition, the filter was not tuned well for the small T-wave amplitude compared to the T-wave amplitude seen in Signal 1.

The other signals where the MMAE algorithm did not perform well each have waveforms or irregularities in the signal that were not modeled. Table 4-3 lists the various irregularities present in each signal. The algorithm is expecting a positive, distinct QRS complex, along with positive, distinct T-waves and P-waves, and it does not have models to process irregularities in the signal.

Table 4-3. ECG Sample Differences from Characteristic Waveform

Sample	Signal	QRS Complex	T-wave	P-wave	Irregularities
ECG 3	2	Negative	Negative	Low strength	None
ECG 5	2	Positive	Low strength	Low strength	None
ECG 11	2	Positive	ST Depression	Positive	R'-wave
ECG 13	1	Positive	Positive	Positive	None
ECG 19	2	Positive	Negative	Positive	None
ECG 21	2	Positive	Negative	Positive	None
ECG 23	1	Positive	Dip	Positive	None
ECG 25	1	Positive	Dip	Positive	None
ECG 27	2	Negative	ST Depression	Positive	None
ECG 39	1	Positive	ST Depression	Positive	R'-wave
ECG 39	2	Positive	ST Depression	Positive	None

Note that Table 4-3 does not show a medial diagnosis based on the ECG signal but rather identifies characteristics in the signal that did not fit the hypothesized ECG segment models. These irregularities can be processed using the MMAE with additional specifically tuned ECG segment models. Specifically, the QRS complex may be positive or negative depending on the lead used, and may be a warning indicator that can be used in future models, as will be discussed in Section 4.3.3. Conversely, a depressed ST segment is an indicator of cardiac ischemia, or lack of oxygen in an area of the heart muscle. An R'-wave, or a second R-wave, is also an indicator that can be used for medical condition diagnosis.

4.3 Animal Exsanguination ECG Data

The animal exsanguination ECG data obtained from Qualia Computing, Inc. [1] was especially difficult to process due to the changing heart rate, changing waveform, and changing signal to noise ratio. The MMAE algorithm's accuracy based on 400-second intervals is shown in Table 4-4.

Table 4-4. MMAE ECG Processing Score for Exsanguination Data

Sample	Signal Time, min	R-Wave Detected	Restarts	Accuracy
Q 1	0-6.67	865	10	98.86%
Q 2	6.67-13.33	816	23	97.26%
Q 3	13.33-20.00	790	137	85.22%
Q 4	20.00-26.67	699	132	84.12%
Q 5	26.67-33.33	692	35	95.19%
Q 6	33.33-40.00	729	2	99.73%
Q 7	40.00-46.67	756	3	99.60%
Q 8	46.67-53.33	792	15	98.14%
Q 9	53.33-60.00	722	123	85.44%
Q 10	60.00-66.66	814	7	99.15%
Q 11	66.66-73.33	880	0	100.00%
Q 12	73.33-80.00	945	1	99.89%
Q 13	80.00-86.67	1157	31	97.39%
Q 14	86.67-93.33	1105	126	89.76%
Q 15	93.33-100.00	1306	90	93.55%
Q 16	100.00-106.67	932	536	63.49%
Q 17	106.67-113.33	994	502	66.44%
Q 18	113.33-120.00	1085	510	68.03%

Note from Table 4-4 that the MMAE algorithm has an accuracy score above 0.90 in 12 out of the 18 signal sections. The score rises and falls in Samples 1 through 9 due to the changing waveform. The score drops again in Samples 14 to 18 because of declining signal amplitude and increased noise on the characteristic waveform. Although the accuracy scores drop during segments of the signal, the heart rate was still determined very well. As shown in Figure 4-11, until the 86-minute mark in the data set, the heart rate was tightly packed, except every 20 minutes from the 16-minute mark onwards. The seemingly incorrect heart rate data at approximately 38 and 78 minutes was correct. Visual confirmation of these heart rates showed that the algorithm correctly tracked the quickly decreasing and increasing heart rate. The processing results are shown in Figure 4-11 through Figure 4-14.

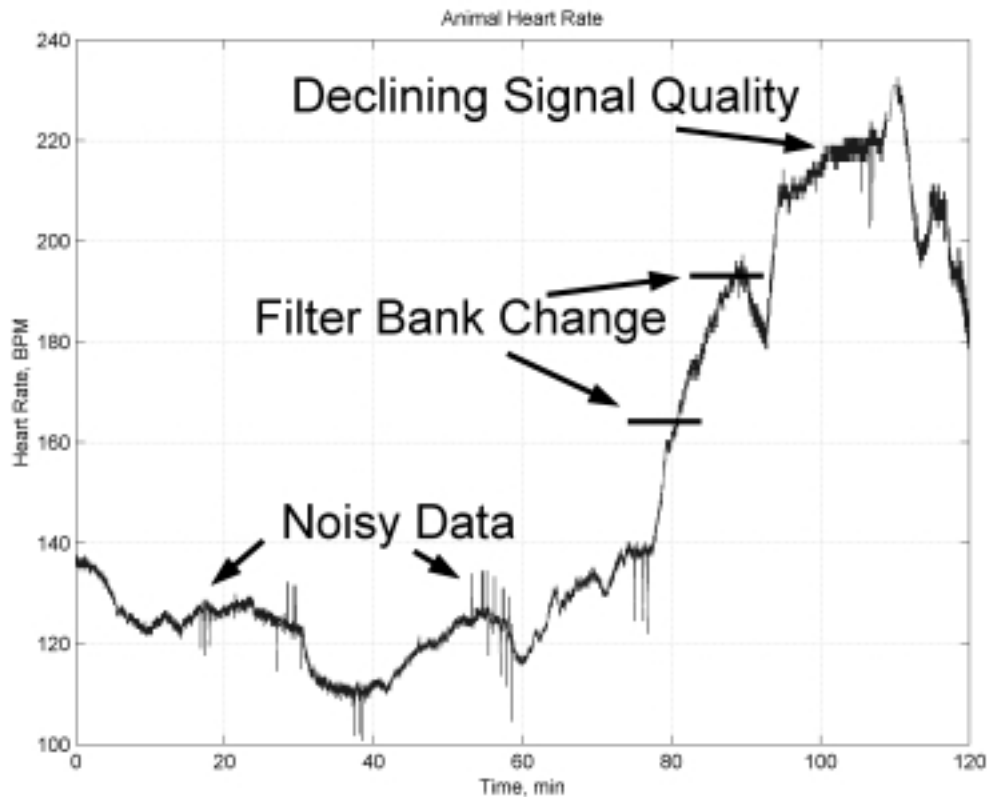


Figure 4-11. Animal Heart Rate During Exsanguination

Note the seamless transition between filter bank models at 165 BPM and again at 195 BPM, which were brought online by simply changing the bank used to select the two online hypotheses.

While the heart rate plot does not show significant noise, the QT interval and the QTc interval both display significant noise, as shown in Figure 4-12 and Figure 4-13.

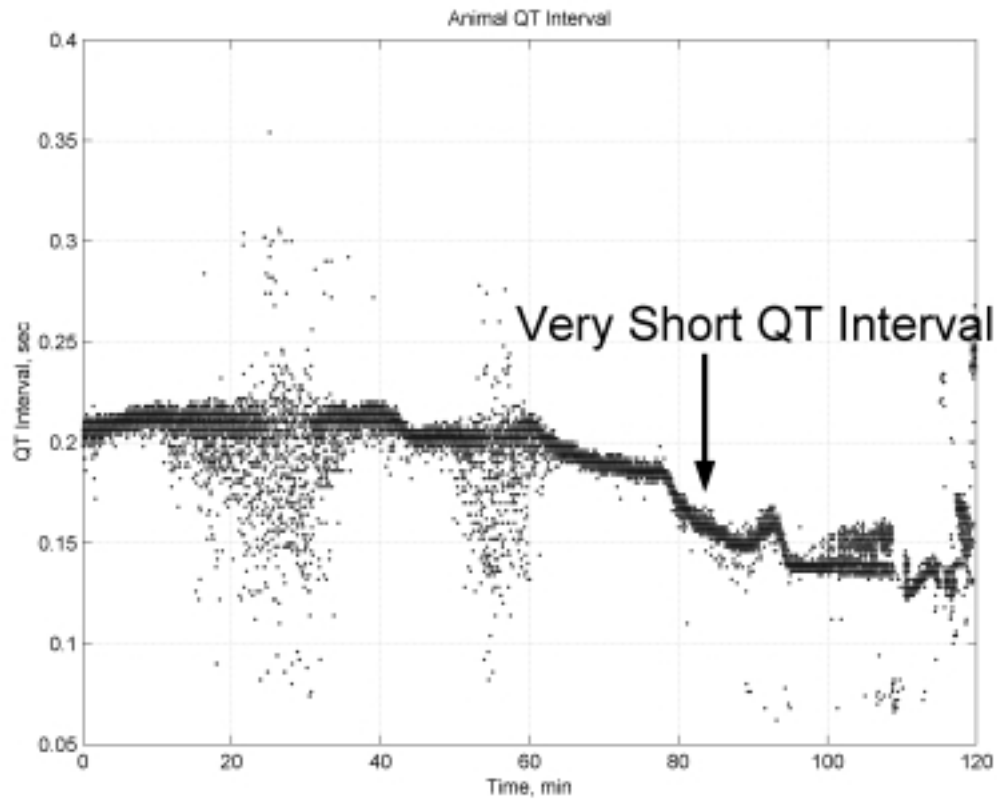


Figure 4-12. Animal Exsanguination QT Interval

Note in Figure 4-12 how the QT interval starts out very short compared to an average QT interval and then get significantly shorter as the heart rate increases. This effect is also shown in the QTc interval plot in Figure 4-13. The QTc interval starts out at approximately 0.31 seconds, significantly shorter than the normal 0.40 second corrected interval and then continues to decline.

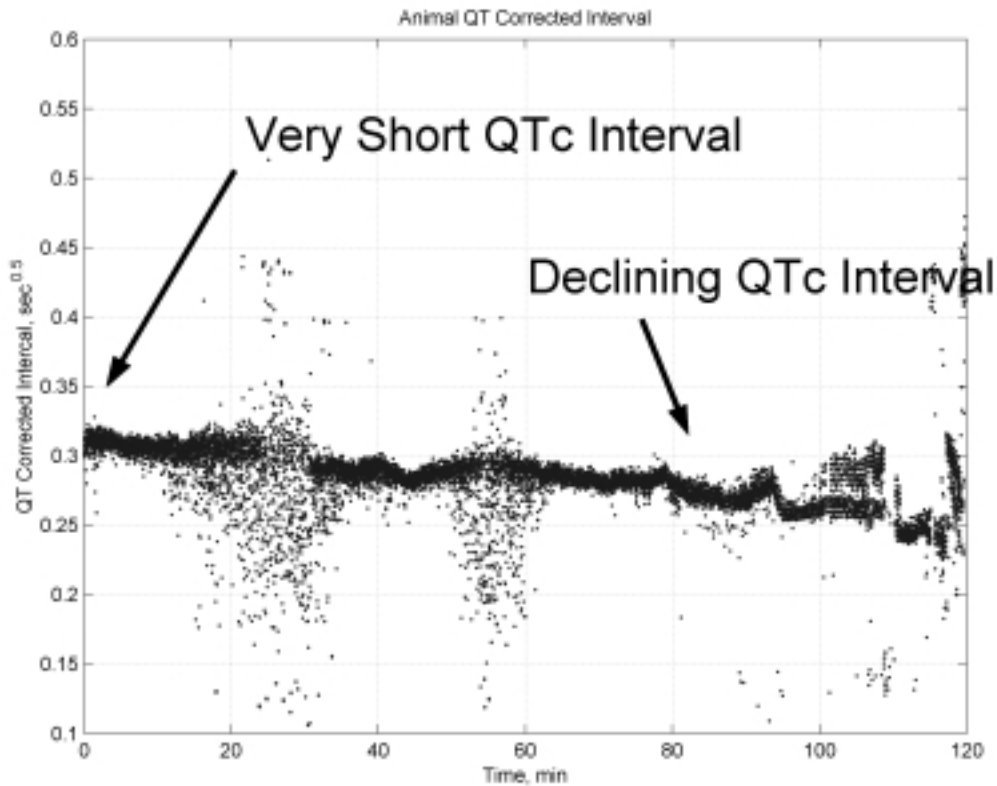


Figure 4-13. Animal Exsanguination QTc Interval

As noted in Section 4.2.1, the Q-wave determination was questionable with the MMAE algorithm. While most of the noise stems came from the noisy signal and poor accuracy in determining the T-wave peak amidst the other extraneous peaks, some inaccuracies stem from the Q-wave determination. Note that, even when the QT interval was corrected for heart rate, it was still falling throughout the experiment. The PR interval was also noisy in several signal segments, as shown in Figure 4-14. Figure 4-14 also shows the PR interval variance. This variance is related to the RR interval variance and shows the balance between the PNS and the SNS (see Section 2.2.1.2). Note that the variance initially increases dramatically, then decreases.

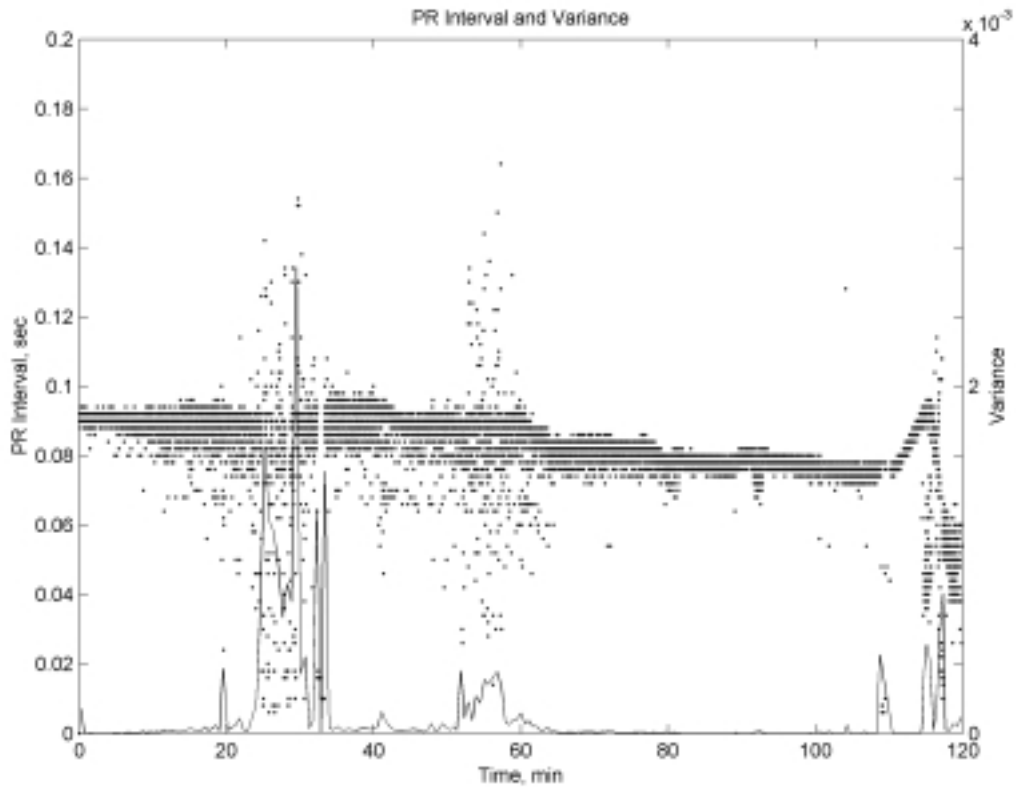


Figure 4-14. Animal Exsanguination PR Interval and PR Interval Variance

The PR interval determination results did not have the problem noted in some MIT signals, namely the shortened interval. Visual signal inspection confirmed that the PR interval determination was accurate with few late P-wave hypothesis declarations. However, in sections where the signal was noisy and the R-wave determination was difficult, the P-wave determination was even more difficult. Note the sampling effects on the PR interval, shown by the discretized PR interval values. A correct QRS complex hypothesis did not guarantee the P-wave peak accuracy due to the other spikes or peaks in the signal. The next sections will analyze the problem areas in the signal, specifically samples Q 4 and Q 9, Q 14, and Q 16, Q 17, and Q 18.

4.3.1. Analysis of Problem Samples Q4 and Q9

The first challenge for the MMAE ECG processing algorithm came from data set Q 4. Physiological changes within the animal caused large amounts of electrical noise between R-waves. As shown in

Figure 4-15, the T-waves and the P-waves were indistinguishable from the other peaks between R-waves. This caused havoc for the hypothesis-swapping algorithm and resulted in degraded performance, as the accuracy score for sample Q 4 in Table 4-4 reflects. Note that, while the performance did degrade, the MMAE ECG processing algorithm was able to handle this noisy signal and give an adequate, although not perfect, processing output in the form of heart rate, QT interval, and PR interval.

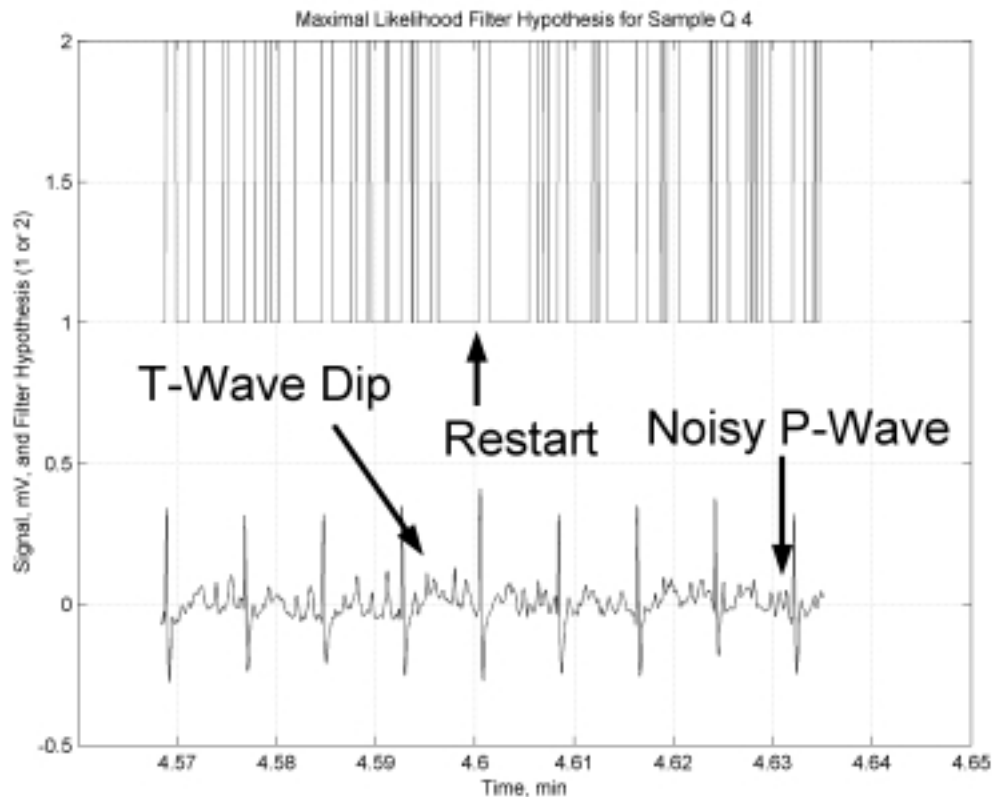


Figure 4-15. Representative ECG Sample from Q 4 with MAP Hypothesis

Note in Figure 4-15 that the noise level made the T-wave and P-wave almost indistinguishable in most cases. While in some cases the algorithm was able to continue switching the online hypotheses and maintaining lock with the QRS complex, such as the RR interval centered at 4.58 minutes, at other times the algorithm was confused by the many signal spikes. While these spikes may have had both the frequency content and amplitude consistent with the hypothesized T-wave or P-wave, the MMAE algorithm's accuracy in determining these waveforms is questionable at best in the presence of severe noise.

Data sample Q 9 had similar problems to Q 4 due to increased noise between the R-waves. Another noisy signal MAP hypothesis output example is shown in Figure 4-16.

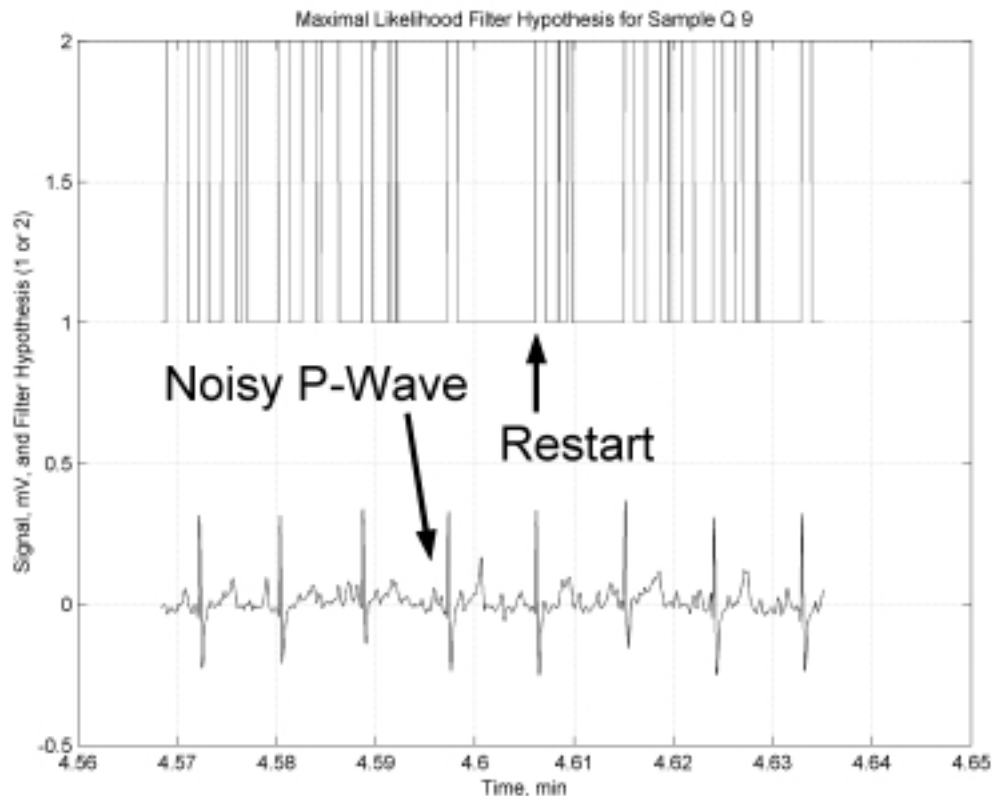


Figure 4-16. Representative ECG Sample from Q 9 with MAP Hypothesis

The shape of the T-waves and P-waves was distinguishable from the noise. However, as in Q 4, the MMAE ECG processing algorithm was able to output valuable information even with a noisy signal. While the algorithm did not catch every R-wave, T-wave and P-wave correctly, it was still able to extract 85% of the R-waves, as denoted by its accuracy score. Note the extraneous noise spikes in the signal between the R-waves and the corresponding hypothesis swapping algorithm incapacitation at approximately 4.6 minutes. At other times, such as at the RR interval starting at 4.58 minutes, the MMAE algorithm was robust in handling the lower noise level. An alternative hypothesis can be developed for this case focusing only on the QRS complex, while not hypothesizing the T-wave or P-wave. Logic can also be developed to switch to a filter bank that looks for the QRS complex only. While this does not extract all the signal information, it does allow the algorithm to continue processing and extracting heart rate information.

4.3.2. Analysis of Problem Sample Q 14

While the performance in Q 14 was very good overall with an accuracy score of 0.90, this signal provides challenges for the MMAE ECG processing algorithm because it was actually between filter banks. The signal strength was decreasing and, while the hypothesis filter banks could account for this change, the signal strength was not high enough for the first bank and was too high for the second bank that was switched to at a 165 BPM heart rate. The filter bank was better matched to the signal strength in middle to end of Q 15. Note that most of the restarts in Q 15 came during the first 2 minutes.

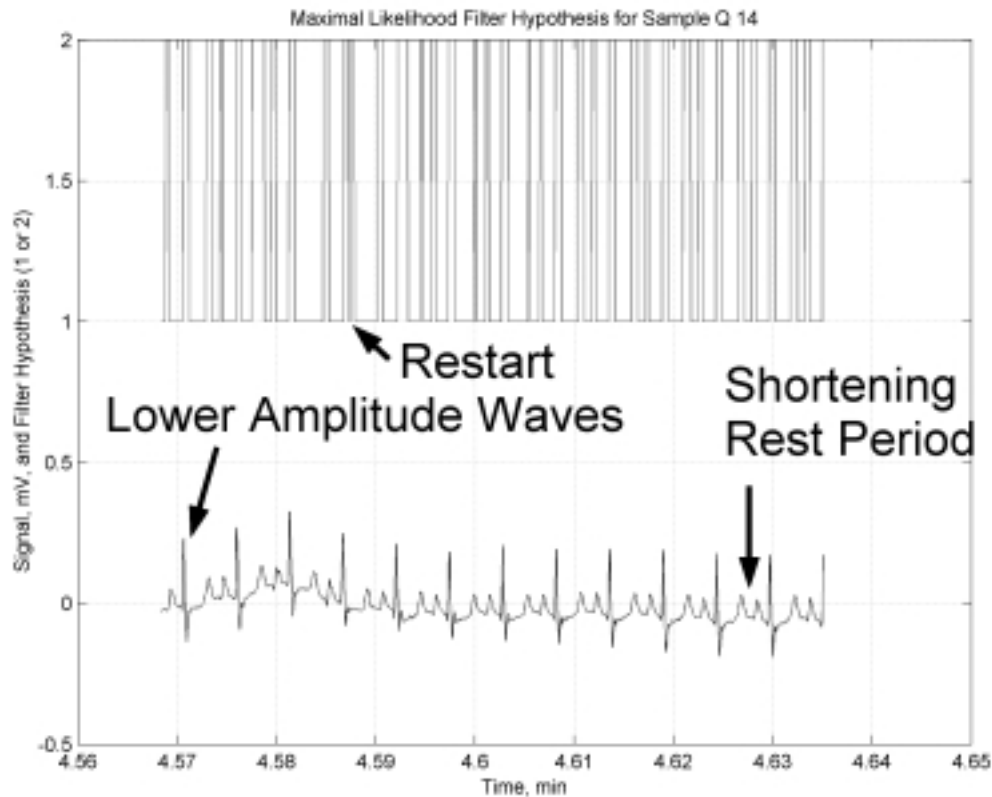


Figure 4-17. Representative ECG Sample from Q 14 with MAP Hypothesis

The filter bank was switching hypotheses very rapidly as shown in Figure 4-17. The heart rate was increasing above 180 BPM, or three beats per second. This means that the hypothesis-swapping algorithm must correctly declare a hypothesis to be correct 18 times in one second. While the QRS complex width stayed approximately the same width as at the data set start, the T-wave width was approximately half its original width. The T-wave was also not as steep or pronounced as the T-waves at the signal start. Moreover, the T-wave and the P-wave were getting consistently closer together, indicating that the filter models were becoming inadequate for this high-speed signal.

Again, the performance was very good overall. However, the performance could be improved by looking at other modeling options for this signal type.

4.3.3. Analysis of Problem Sample Q 16, Q 17, Q 18

Samples Q 16, Q 17, and Q 18 at the end of the data file were extremely weak. Comparing the signal amplitudes, the R-wave was as big as the T-wave before it disappeared and the S-wave dominated the signal. When the R-wave was so small, the filter could distinguish the R-wave from the other peaks based solely on the signal frequency content. The R-wave is a much higher frequency signal than the T-wave or P-wave, as shown in Chapter 3. However, much of the success of the R-wave determination has been based on both its very distinguishable amplitude and frequency content. When the R-wave disappeared completely in sample Q 18, the signal no longer fit the characteristic ECG waveform as expected by the hypothesis filter bank. This change in the QRS complex is different from ECG 3 Signal 1 and ECG 27 Signal 2 because this lead used previously had an R-wave. ECG 3 Signal 1 and ECG 27 Signal 2 used leads that may not show the positive R-wave. This change in QRS complex shape may be a warning indicator that the MMAE can generate. Note also that the extremely high, over 200 BPM heart rate significantly shortened the interval between the T-wave and the P-wave. In some cases, this resulted in a continuous curve between the two waves, without the “rest” period as required in the hypothesis model. Note in Figure 4-18 how the T-waves and P-waves were essentially one dynamic segment.

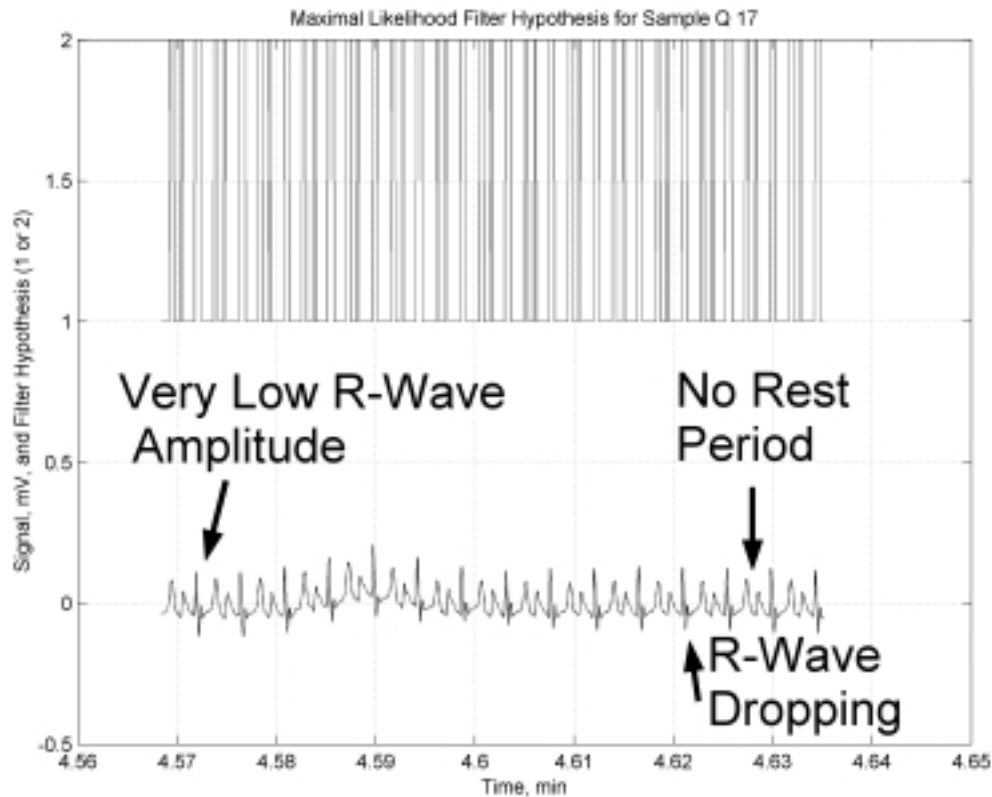


Figure 4-18. Representative ECG Sample from Q 17 with MAP Hypothesis

The high heart rate caused the filter probabilities to flow very quickly. A better representation for this signal type may use fewer hypothesis models allowing the hypothesis declaration to stay constant for more samples. This may aid the filter-swapping algorithm and improve performance in high heart rate cases.

4.4 Summary

This chapter presented the MMAE ECG processing test results. The algorithm was tested on 20 signals from the MIT ECG database and animal exsanguination data. Test parameters included the algorithm's identification accuracy for the R-wave, P-wave,

and T-wave. An accuracy score was assigned to each processed signal based on the number of R-waves detected and number of restarts in the algorithm during the processing. This score was most important because, if this score was not high, the other intervals could not accurately be determined based on the algorithm flow.

MIT ECG database signals generally fell into two categories: those that the algorithm processed well and those that the algorithm processed poorly. The reasons for this generalization were also investigated. It was found that, when the electrode lead measured a signal that was accurately modeled in the hypothesis filter banks, the MMAE could accurately calculate the conditional probability for each segment's hypothesis model. The MMAE could handle noisy signals to some extent. However, the ECG characteristic waveform needed to be distinguishable from other signal segments in these cases. The T-wave peak was determined precisely if the QRS complex could be accurately determined. The P-wave peak was more difficult to determine, mainly due to its lower amplitude or noise during the rest period. In some signals, the P-wave hypothesis was declared correct after the P-wave peak, causing a PR interval shortening, erroneously representing the true signal by approximately 0.01 to 0.03 seconds. Specifically tuning the hypothesis banks to the individual signal would solve this problem and make the MMAE algorithm more robust. The QT interval was shortened because the QRS complex hypothesis was declared correct at the R-wave onset, approximately 0.01 to 0.05 seconds after the Q-wave onset.

In contrast, the algorithm did not work well when the signal was not well modeled in the hypothesis filter banks mainly due to the electrode lead placement. Two signals had two R-waves in the QRS complex, four signals had an ST segment depression, and

one signal did not have a P-wave. The algorithm was still able to give a heart rate, QT interval, and PR interval indication. Additional models can be created for these signal types to allow the MMAE to process signals with these characteristics.

Data from an animal exsanguination was also tested with the processing algorithm. This signal presented a varying heart rate, changing waveforms, and changing signal strength to challenge the MMAE. The algorithm performed well when the signal was well modeled in the hypothesis bank, and was robust when processing noisy samples that did not make the T-waves or P-waves indistinguishable from other spikes. The filter bank seamlessly switched at 165 BPM which corresponded with decreasing signal strength, demonstrating that other filter banks can be easily brought online if required. The MMAE did have problems in four sections of the signal where noise and buried P-waves became a problem.

Overall, this algorithm worked exceptionally well considering that no individual tuning was required for each signal after the models were developed. Improvements to the algorithm are possible, allowing the MMAE to be robust in its capabilities.

5. Conclusions and Recommendations

5.1 Overview

The research presented in this thesis sets the foundation for the long-term research goal to build a real-time personnel navigation and physiological monitoring system. The system will contain four components: (1) physiological sensors including respiration sensors and ECG sensors, (2) personal navigation using GPS, (3) wireless transmission capabilities, and (4) physiological data processing and warning software. The physiological sensor theory was presented in detail, including ECG and pulse oximetry theory, in Chapter 2. It was shown that the ECG signal not only provides information about the activities in the heart, but also provides information about the autonomic nervous system (ANS), which controls many of the automatic activities in the body. From the relationships in the characteristic ECG waveform timing, it is possible to gain insight into ANS activity. Additionally, a GPS overview and its benefits to the overall system were presented. Finally, Kalman filtering and MMAE theory was shown to provide a basis for the ECG processing algorithm.

This research focused on developing an ECG processing algorithm capable of determining the heart rate, QT interval, and PR interval. This is the first known research effort using adaptive estimation to attempt to segment the ECG signal using a Kalman filter or MMAE. The MMAE is robust in that it calculates a conditional probability for each model in the filter bank, assessing as to which model best represents the true system as seen from the measurements. The system models were based on the QRS complex, T-wave, and P-wave power spectral density estimates. Hypothesis filter banks were

developed based on the signal strength and the bandpass filter center frequency. The MMAE generates a conditional probability for each model, with the highest probability corresponding to the filter hypothesis with the closest characteristic ECG signal segment. An additional algorithm was developed using the characteristic ECG waveform event order to reduce the number of online filters from four hypotheses to two hypotheses. In addition, a probability-smoothing algorithm was developed based on the knowledge that the signal segments do not typically change in a short number of samples. The algorithm was then tested against 20 signals from the MIT ECG database and 18 signals from the animal exsanguination data, totaling approximately 140 minutes in duration.

5.2 Conclusion

The MMAE ECG processing algorithm developed in this research performed extremely well when the signal of interest contained the ECG characteristic waveform components. It was shown that the electrode lead placements measured different heart events and very clearly affected the MMAE algorithm's performance. In 12 out of the 38 signals, 32 minutes of data, the ECG processing algorithm did not have a restart and perfectly found the heart rate. Moreover, in 26 out of the 38 signals, the algorithm had an accuracy score over 0.90. The overall MMAE ECG processing algorithm accuracy is shown in Table 5-1. The accuracy score was broken up into all data sets processed (denoted "all"), those that fit the characteristic ECG waveform, but may have not fit it well (denoted "fit"), and those that fit the expected waveform well (denoted "best").

Table 5-1. Overall Algorithm Accuracy

Data Set	R-wave	Restart	Accuracy
MIT-all	1121	178	86.30%
MIT-fit	958	28	97.16%
MIT-best	633	10	98.44%
Animal-all	16079	2283	87.57%
Animal-fit	13068	735	94.68%
nimal-best	10542	354	96.75%
Total-all	17200	2461	87.48%
Total-fit	14026	763	94.84%
Total-best	11175	364	96.85%

The first row in Table 5-1 shows the accuracy score for all MIT ECG signals processed including the lead III signals that tended not to contain the characteristic ECG waveform. The 86.3% accuracy score is not the MMAE’s best performance because the models were not built to handle the varying waveforms seen in these signals. When the signal set was reduced to those that contained only the characteristic ECG waveform, including some from lead III, the accuracy score jumped dramatically to 97.2%. Additionally, when the data set is reduced even further to include signals from just lead V4, the accuracy is 98.4%.

The MMAE algorithm processed the animal ECG data with 87.5% accuracy for the whole data set. Because the signal strength during the last three signal segments is very low, these last segments can be removed to form a data set that generally fits the MMAE models. The accuracy score for the combined first 15 data sets was 94.7%. Finally, three noisy data segments where the T-wave or P-wave was indistinguishable from other extraneous signal peaks can also be removed. The accuracy score for these “best” fit signal segments was 96.8%.

Finally, the combined total scores are also shown in Table 5-1. For all data sets processed, the MMAE algorithm had an accuracy of 87.5%. Again, this is a low number because many signal segments were from leads that did not contain the characteristic ECG waveform, were very noisy, or had low signal strength. If the data sets are restricted to those containing the characteristic ECG waveform, the accuracy jumps to 94.8%. In addition, if the animal exsanguination signals that were very noisy were taken out, the accuracy would jump to 96.8%. When the algorithm correctly found the QRS complex, it subsequently could find the T-wave peak and the P-wave peak with high probability. The PR interval was at times shortened because the P-wave hypothesis was declared correct after the P-wave peak. Additionally, it was shown that the Q-wave timing was consistently biased approximately 0.02 to 0.05 seconds after the true Q-wave onset. However, the Q-wave marker can simply be placed back in time the appropriate number of samples.

The algorithm's weaknesses were also identified by the signals that it could not process with high accuracy. The 12 signals where the algorithm did not perform well represent signals where the algorithm could not identify the T-waves or P-waves in the signal due to excess noise or the lead placement choice. However, it is important to note that the hypothesis models were not developed based on these types of signals. It was pointed out that additional models could easily be developed and integrated into the MMAE filter banks to make the MMAE ECG processing algorithm more robust.

Using this unique technique, it has been exhibited for the first time, the temporal sequence of beat-to-beat time variation during severe blood loss over a period of several hours. Such data should make possible the early detection of the cascade of events that

leads to fatal irreversible shock in severe injury accidents. Such shock is the cause of death in 40% of civilian accident injury and 66% of wartime injury [25]. This analyzer could be easily added as a software update to the standard physiological monitors universally used in emergency vehicles and treatment facilities.

5.3 Recommendations

The MMAE ECG processing algorithm developed in this research showed promising results, and with further research will provide a firm foundation for a real-time personnel navigation and physiological monitoring system. There are numerous recommendations for further research with the MMAE ECG processing algorithm. The first area deals with the algorithm's robustness, whereas the second area deals with the physiological warning system development.

1. Developing a robust algorithm:

- a. The hypothesis-swapping algorithm is very similar to a hidden Markov model. The MMAE can readily incorporate transition probabilities, clearly indicating the expected transition order such as QRS complex to T-wave, T-wave to rest, and rest to P-wave. Thus, the probability flow is controlled by the transition probabilities rather than the hypothesis-swapping algorithm.
- b. The MMAE can be implemented in a hierarchical structure when more models are added to extract other information from the ECG signal. Many research efforts involving multiple failures and reconfigurable flight control system using the MMAE have

exploited the hierarchical structure [8, 11, 20, 31]. This theory can also be applied to the ECG segmentation algorithm to make the hypothesis swapping a parallel implementation as opposed to this algorithm's sequential nature.

- c. The algorithm currently switches filter banks based on heart rate, if the algorithm has to restart three times in a row at the beginning of a data set, or by manually giving the MMAE a different filter bank. While this worked well in the animal exsanguination data sets where lower signal levels coincided with an increased heart rate and the MIT data sets where the filter bank did not have to change, during long duration processing this may not be the case. Thus, it would be advantageous to develop an algorithm to switch the proper filter banks into the MMAE.
- d. When the MMAE filter banks can be switched in and out automatically, additional banks can be created with hypothesized arrhythmias. This bank can run in parallel to the other banks, looking just for the arrhythmias. An additional conditional probability calculation can be made to determine if an arrhythmia occurred.
- e. Additional hypothesis models can be developed based on the RR, PR, and QT intervals. The statistics of these intervals may contain valuable information, as researched in Chapter 2. Gustafson and Willsky [17] have already done work in this area to detect

arrhythmias. However, these models can be developed to detect other physiological problems.

- f. The filter banks were originally tuned and developed based on the QRS complex. The QRS complex was readily distinguishable from the other waveforms and its model was significantly different from the other models. This motivates online Q adaptation for the QRS complex hypothesis. The stronger the signal, the higher the QRS complex model scalar likelihood quotient. Thus, an online tuning algorithm can be developed to keep the likelihood quotient in a pre-specified range.
- g. Online Q adaptation can also be applied to the entire filter bank. The MMAE algorithm works best when the two online filters are significantly different. The dichotomy between the hypotheses aids the hypothesis-swapping algorithm, allowing it to switch the filter banks at the correct position in the ECG characteristic waveform. The distinction is best seen in the scalar likelihood quotient. The likelihood quotient for the QRS complex hypothesis should be on the order of the number of measurements. However, when the algorithm performed well, the likelihood quotient for the hypotheses before or after the QRS complex hypothesis was consistently an order of magnitude higher than during the QRS segment.

- h. The MMAE filter bank assumes that the signal follows the characteristic ECG waveform. If the signal between the R-waves is extremely noisy or a waveform is missing, another filter bank can be brought online capable of handling these cases.
- i. The ST segment was not calculated in this algorithm. The ST segment can also contain valuable information, as an ST segment below a baseline is a cardiac ischemia indicator. This was seen in some of the MIT ECG samples, most significantly in ECG 39. Note that the MMAE had trouble with this signal. Another bank can be brought online to process the ECG signal if this waveform change is detected.

2. Physiological warning system development

- a. The physiological warning system must be developed based on actual doctor-verified dangerous physiological conditions. AFRL/HE has ECG data [59] from subjects in a centrifuge who have blacked out or undergone Gravity induced Loss of Consciousness (GLOC). This data can be used for predicting a pilot's black out during high intensity flying maneuvers and ultimately be incorporated into the flight control system. GLOC is in many ways similar to severe internal bleeding such as the fact that blood is taken away from the brain and it pools in a section of the body, not allowing it to be pumped by the heart. Thus, this

data may also be used to develop a warning system for severe injury.

- b. Verified data can also come from animal exsanguination data. Research is currently being done [1, 26] to investigate when the critical point occurs in the physiological signals of an exsanguinated animal. After the critical point is reached, it may become extremely difficult to save the animal. This data can be applied to a triage situation on the battlefield. Triage is typically done by quickly determining both the heart rate and the blood pressure. Additional information from the ECG signal can be used to triage battlefield casualties accurately.
- c. ECG data can be recorded with the LifeShirt[®] [62] using a human test protocol. The protocol very rigorously specifies the test procedures and ensures that proper precautions are taken as not to injure the subjects. The test can be conducted during flights in fighter aircraft, during fire-fighter training scenarios, or during military training exercises.
- d. Develop means to deal with motion artifacts during exercise or physical activity. Many algorithms already exist to remove these artifacts, especially ECG units developed for exercise stress tests conducted in hospitals. These algorithms can be used to preprocess the signal, or a model of the motion artifacts can be incorporated into the MMAE filters.

- e. The code must be written in another language to speed up processing time for online use. The code currently runs about half the speed of real-time because of the many matrices that are saved for post-processing. Many of these matrices are not needed for online implementation and thus can be taken out of the code. Languages, particularly compiled languages other than MATLAB[®] (i.e. Fortran, C, Basic) may run faster allowing the code to run in real-time
- f. Code must be written to display the important physiological data to the monitoring base station personnel. The data displayed must balance the ability to understand the information by the monitoring personnel for quick interpretation, and the minimum data amount required to convey the person's physiological health estimate.

5.4 Summary

The MMAE ECG processing algorithm performed exceptionally well when the “tool” was used as designed. The algorithm's performance depends greatly on the lead choice, as demonstrated with the MIT ECG signals. The algorithm can also process data from very challenging experiments with high accuracy. The MMAE ECG algorithm provides a firm foundation for future research, including a physiological warning system.

Appendix A. MIT ECG Figures

This appendix gives all figures generated when processing the MIT ECG data. Several representative examples were shown in Chapter 4.

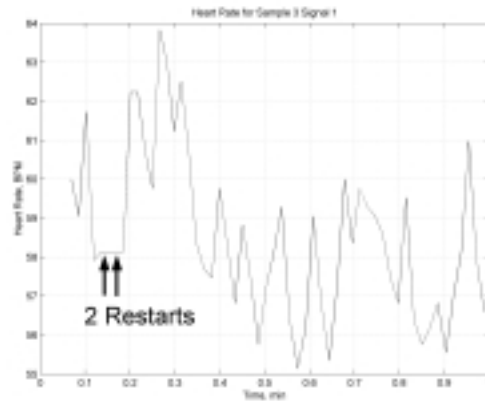


Figure A-1. ECG Sample 3 Signal 1 Heart Rate

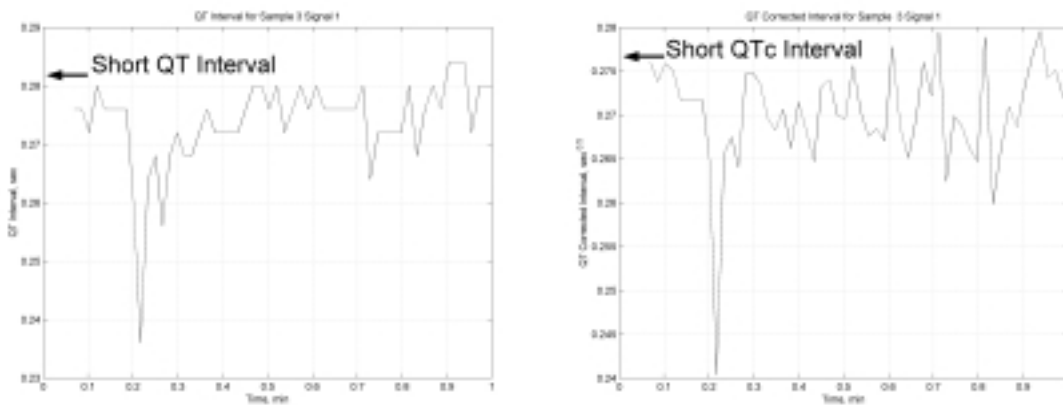


Figure A-2. ECG Sample 3 Signal 1 QT Interval and QTc Interval

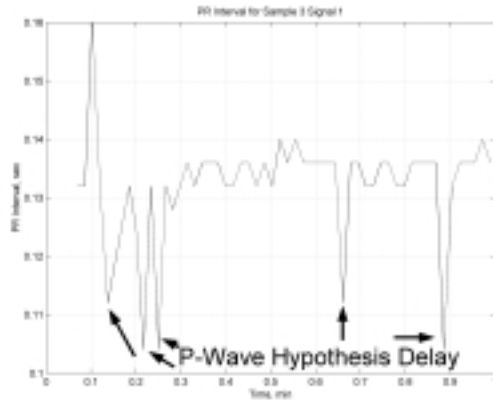


Figure A-3. ECG Sample 3 Signal 1 PR Interval

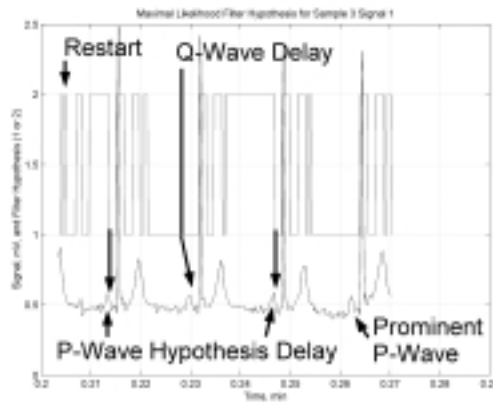


Figure A-4. Maximal Likelihood Filter Hypothesis for Sample 3 Signal 1

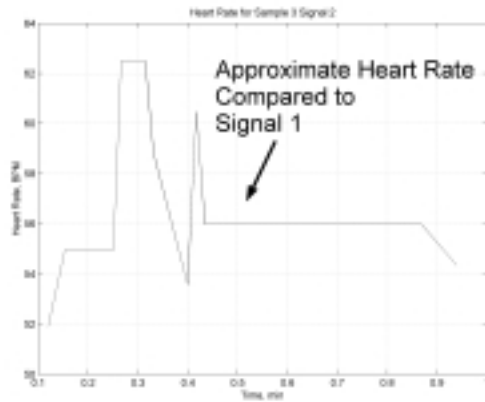


Figure A-5. ECG Sample 3 Signal 2 Heart Rate

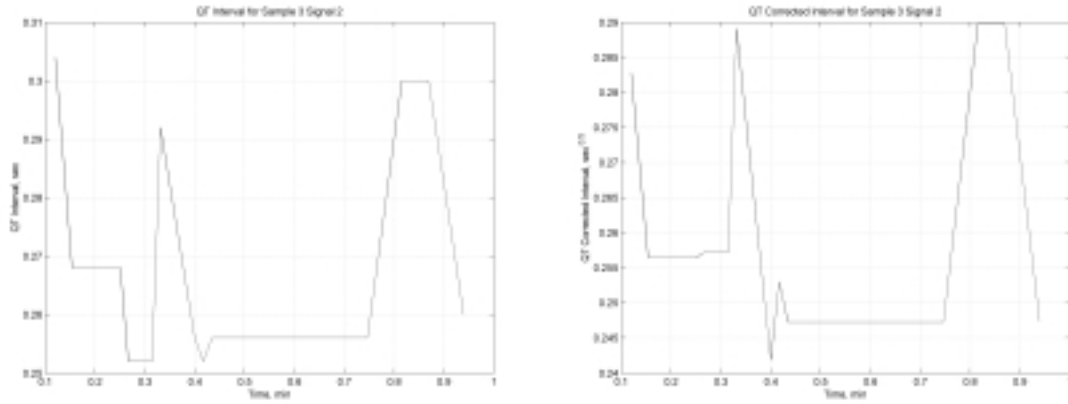


Figure A-6. ECG Sample 3 Signal 2 QT Interval and QTc Interval

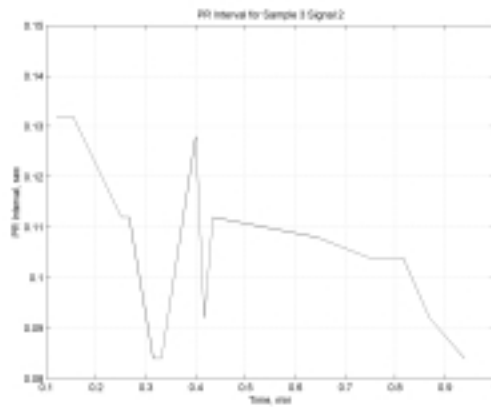


Figure A-7. ECG 3 Signal 2 PR Interval

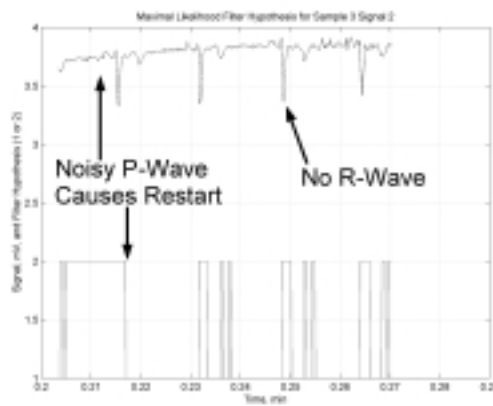


Figure A-8. Maximal Likelihood Filter Hypothesis for Sample 3 Signal 2

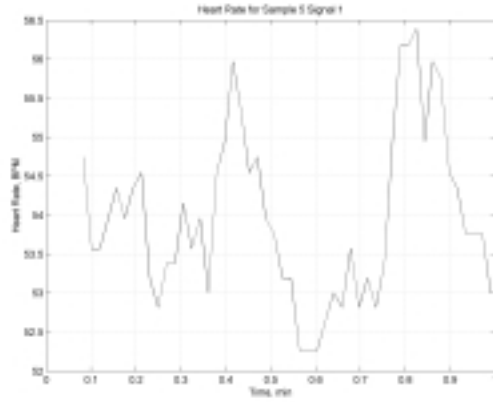


Figure A-9. ECG Sample 5 Signal 1 Heart Rate

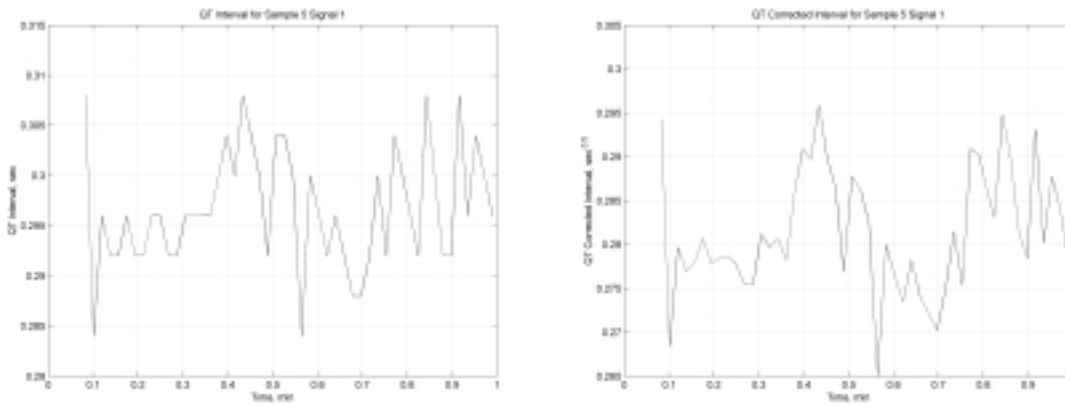


Figure A-10. ECG Sample 5 Signal 1 QT Interval and QTc Interval

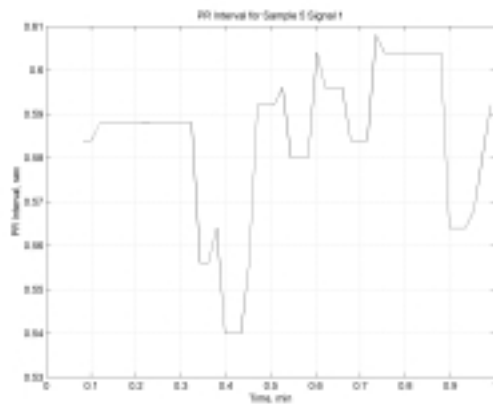


Figure A-11. ECG Sample 5 Signal 1 PR Interval

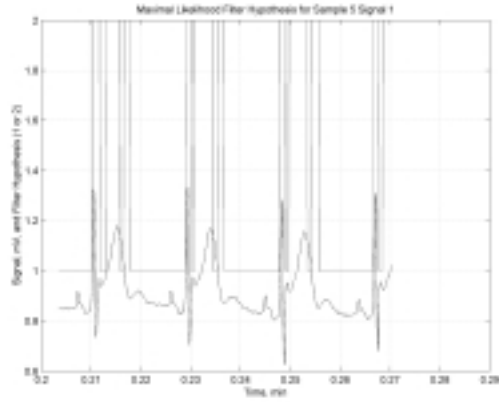


Figure A-12. Maximal Likelihood Filter Hypothesis for Sample 5 Signal 1

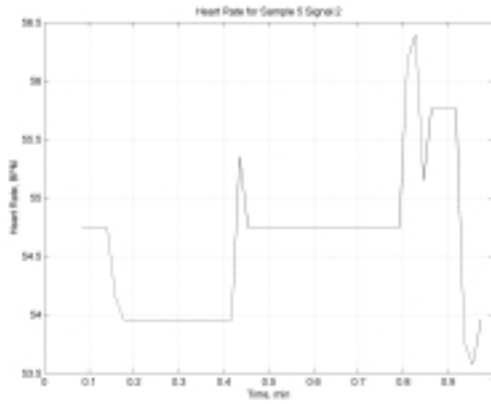


Figure A-13. ECG Sample 5 Signal 2 Heart Rate

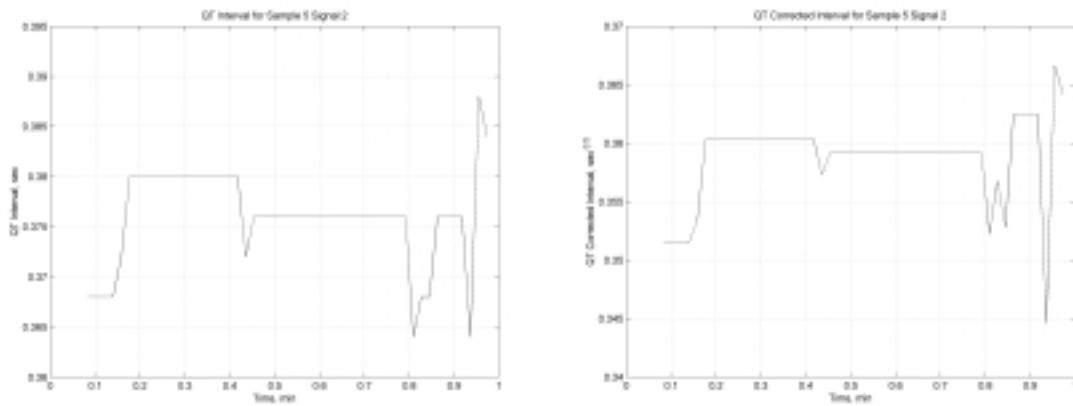


Figure A-14. ECG Sample 5 Signal 2 QT Interval and QTc Interval

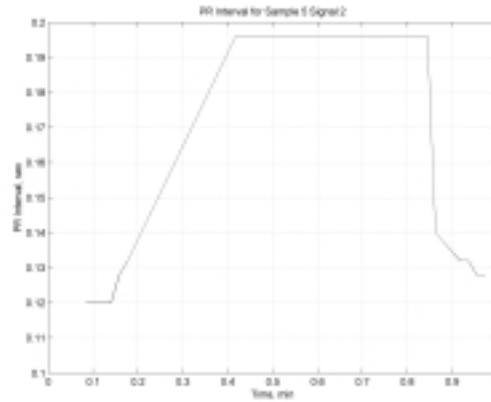


Figure A-15. ECG Sample 5 Signal 2 PR Interval

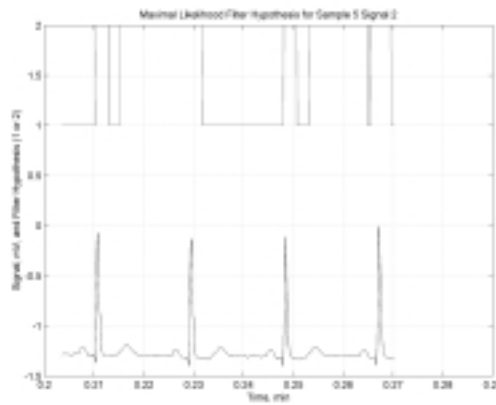


Figure A-16. Maximal Likelihood Filter Hypothesis for Sample 5 Signal 2

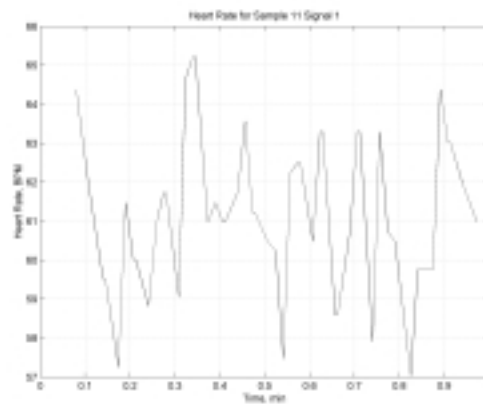


Figure A-17. ECG Sample 11 Signal 1 Heart Rate

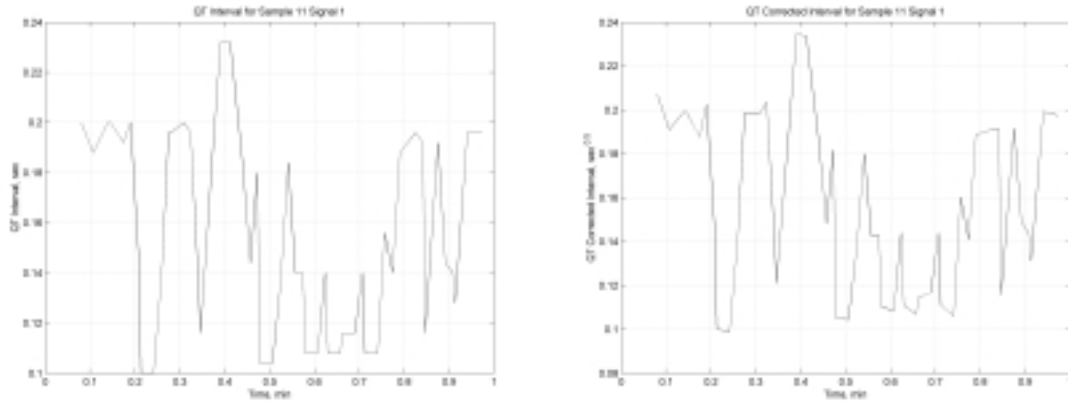


Figure A-18. ECG Sample 11 Signal 1 QT Interval and QTc Interval

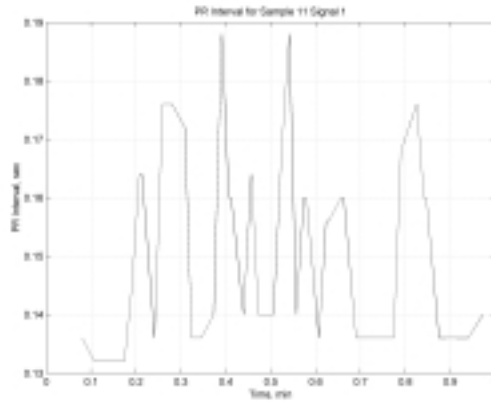


Figure A-19. ECG Sample 11 Signal 1 PR Interval

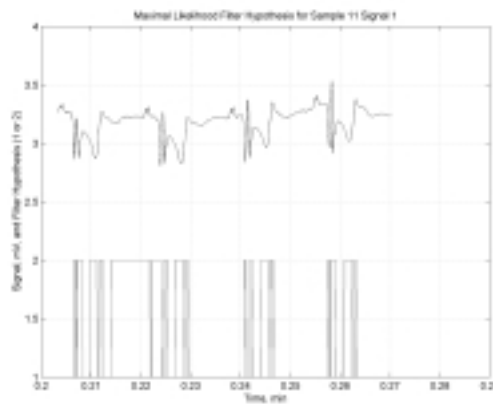


Figure A-20. Maximal Likelihood Filter Hypothesis for Sample 11 Signal 1

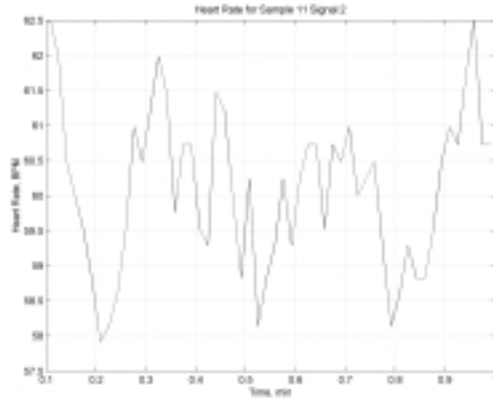


Figure A-21. ECG Sample 11 Signal 2 Heart Rate

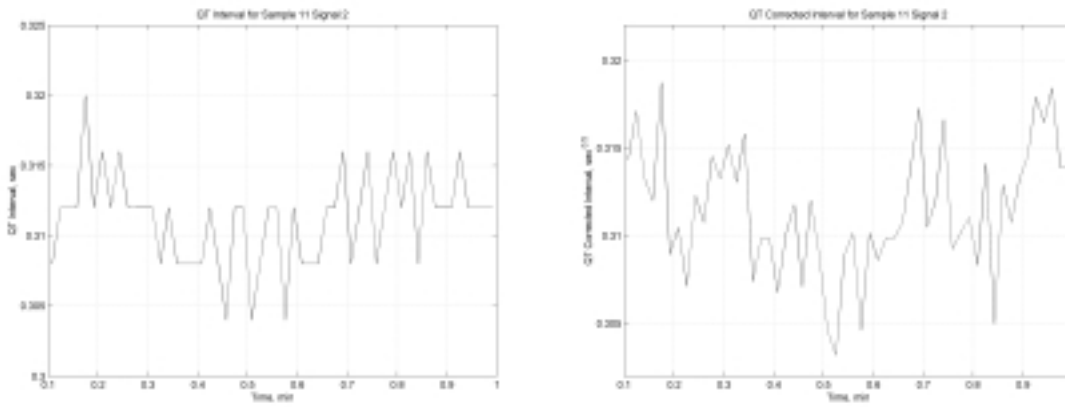


Figure A-22. ECG Sample 11 Signal 2 QT Interval and QTc Interval

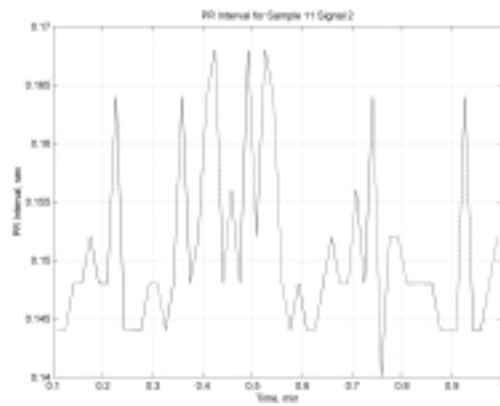


Figure A-23. ECG Sample 11 Signal 2 PR Interval

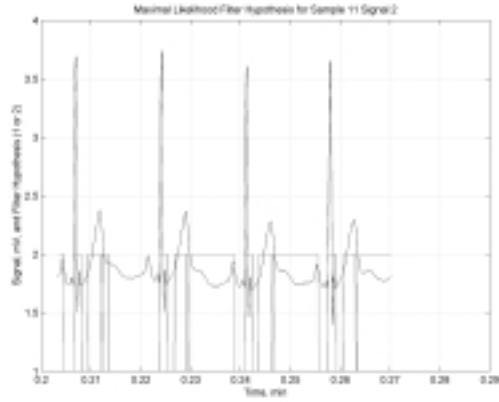


Figure A- 24. Maximal Likelihood Filter Hypothesis for Sample 11 Signal 2

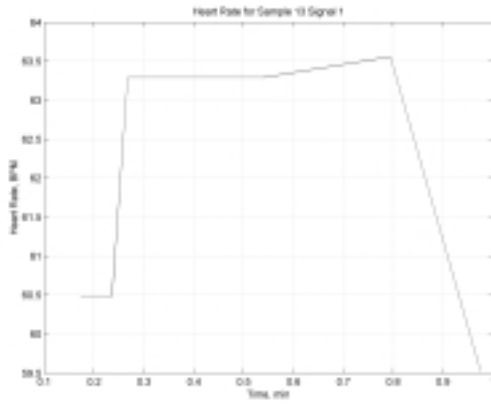


Figure A-25. ECG Sample 13 Signal 1 Heart Rate

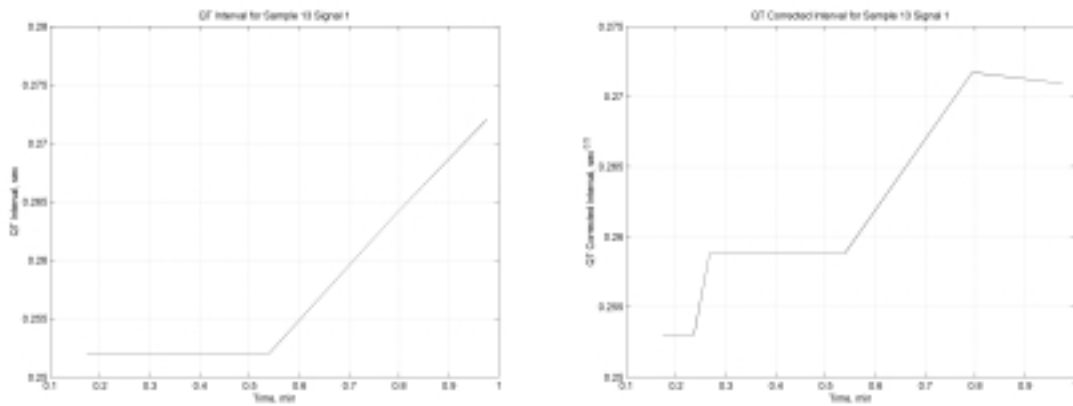


Figure A-26. ECG Sample 13 Signal 1 QT Interval and QTc Interval

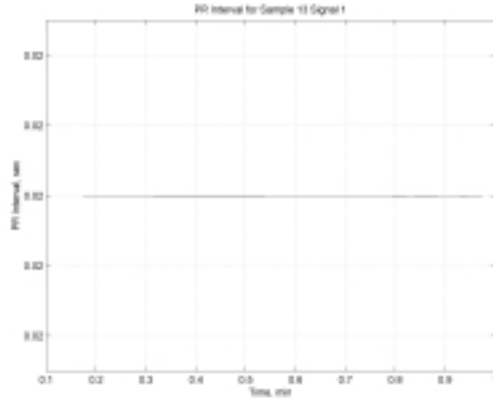


Figure A-27. ECG Sample 13 Signal 1 PR Interval

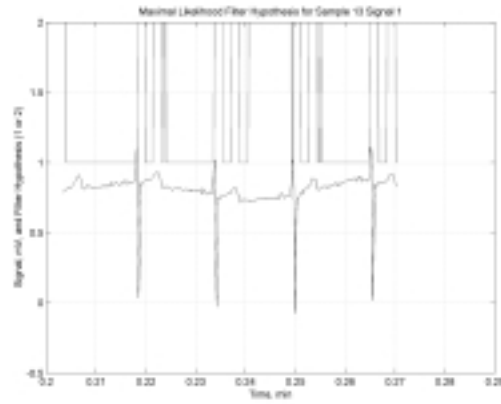


Figure A-28. Maximal Likelihood Filter Hypothesis for Sample 13 Signal 1

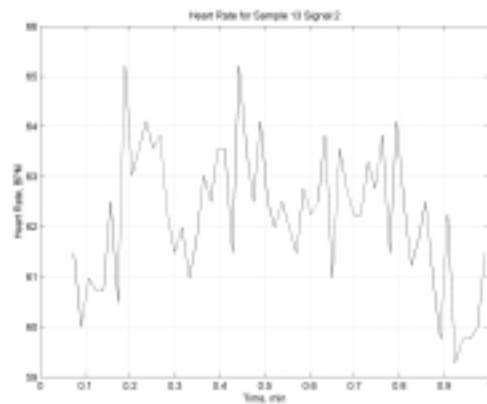


Figure A-29. ECG Sample 13 Signal 2 Heart Rate

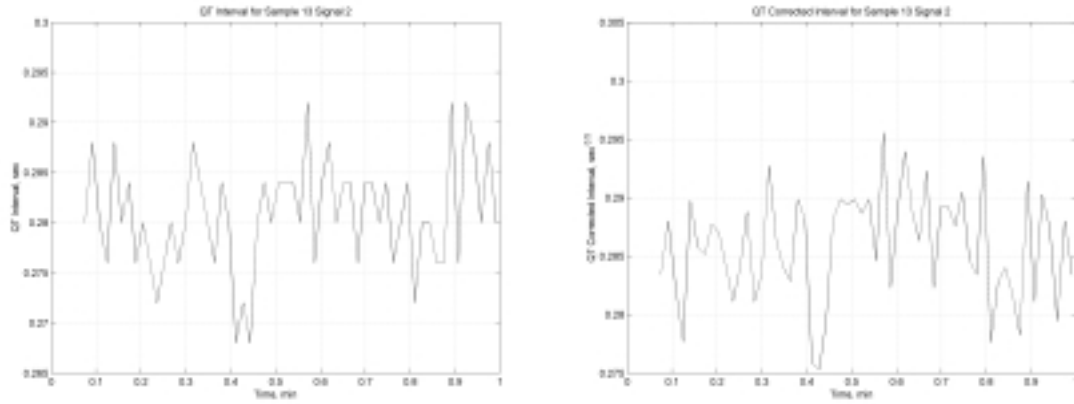


Figure A-30. ECG Sample 13 Signal 2 QT Interval and QTc Interval

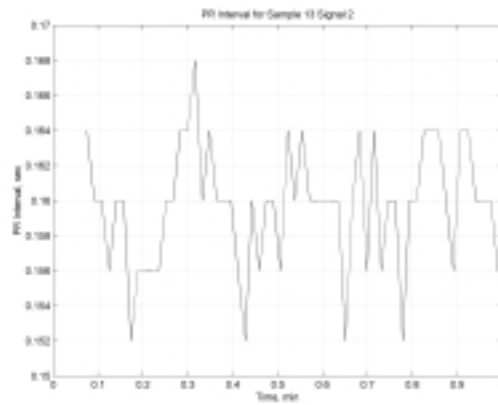


Figure A-31. ECG Sample 13 Signal 2 PR Interval

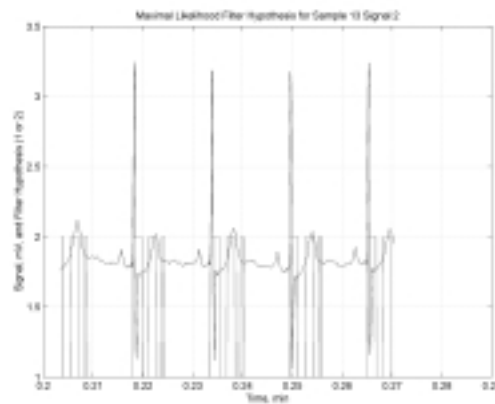


Figure A-32. Maximal Likelihood Filter Hypothesis for Sample 13 Signal 2

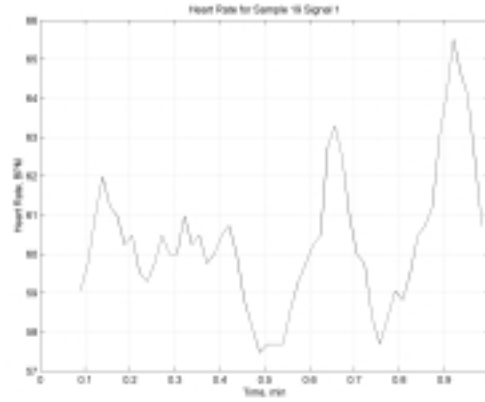


Figure A-33. ECG Sample 19 Signal 1 Heart Rate

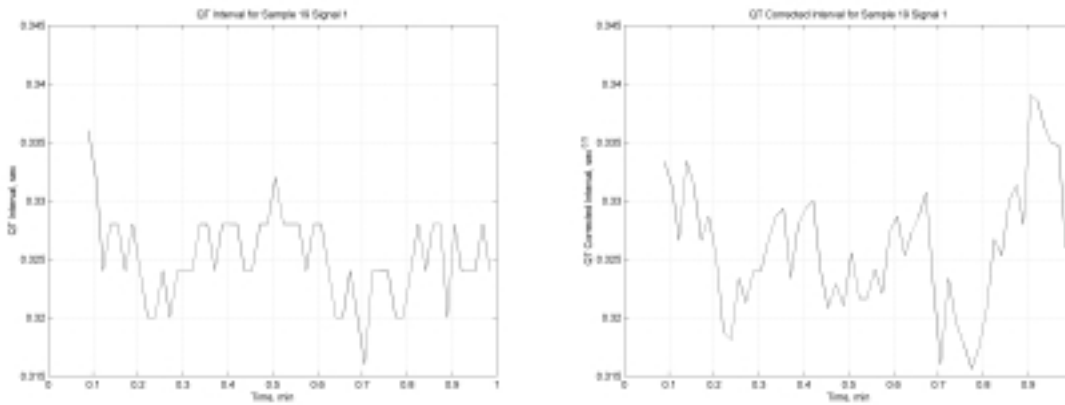


Figure A-34. ECG Sample 19 Signal 1 QT Interval and QTc Interval

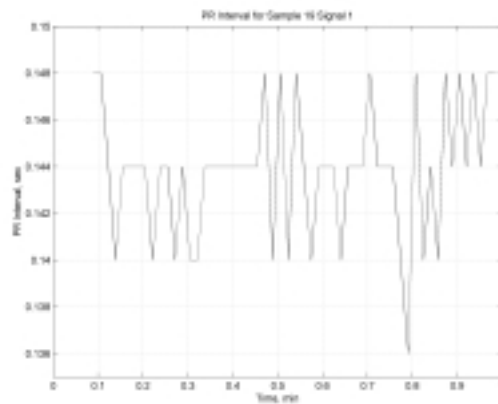


Figure A-35. ECG Sample 19 Signal 1 PR Interval

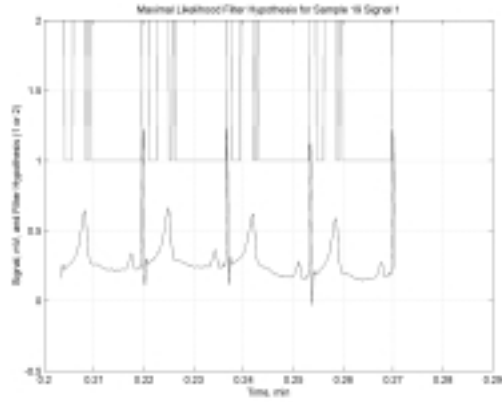


Figure A-36. Maximal Likelihood Filter Hypothesis for Sample 19 Signal 1

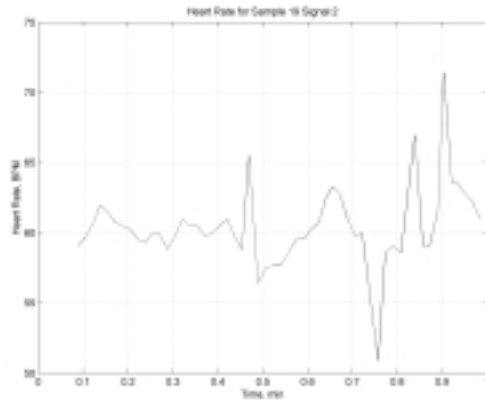


Figure A-37. ECG Sample 19 Signal 2 Heart Rate

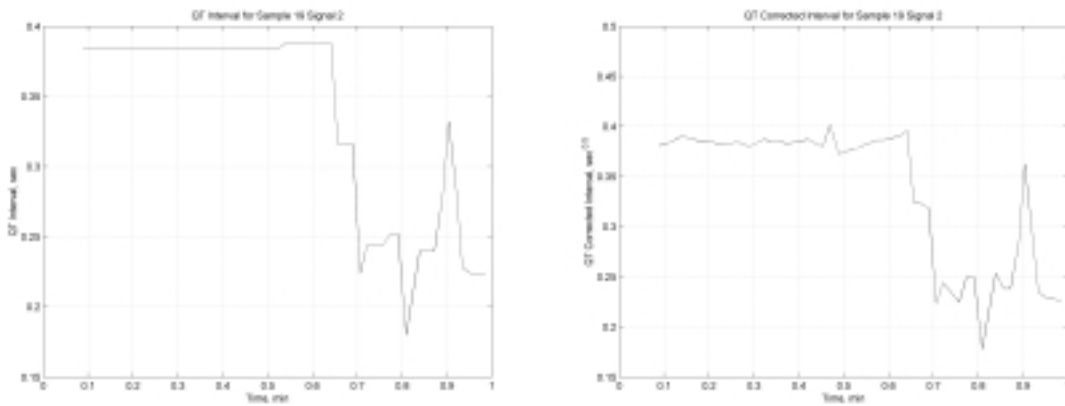


Figure A-38. ECG Sample 19 Signal 2 QT Interval and QTc Interval

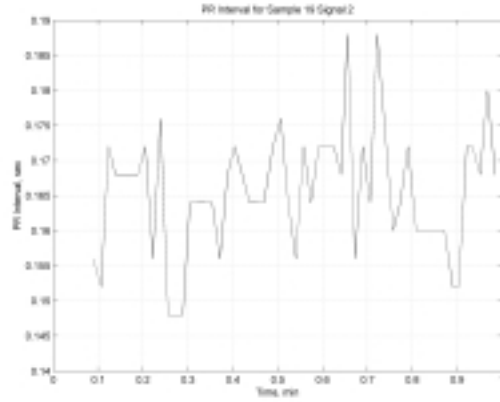


Figure A-39. ECG Sample 19 Signal 2 PR Interval

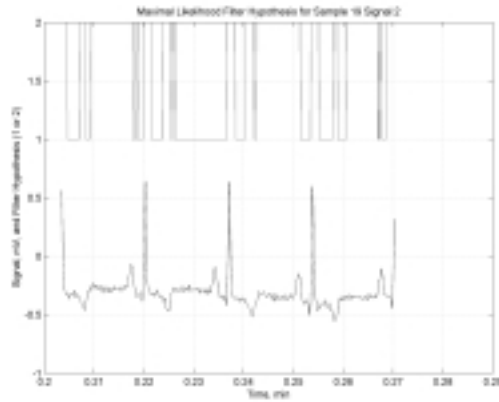


Figure A-40. Maximal Likelihood Filter Hypothesis for Sample 19 Signal 2

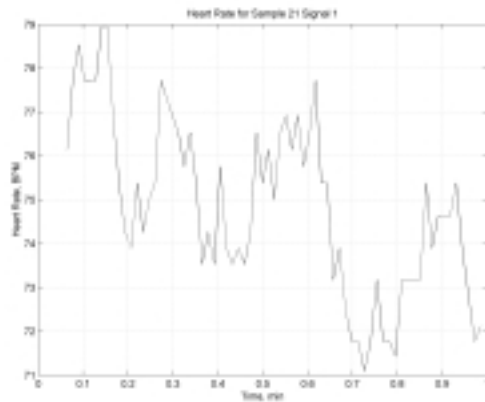


Figure A-41. ECG Sample 21 Signal 1 Heart Rate

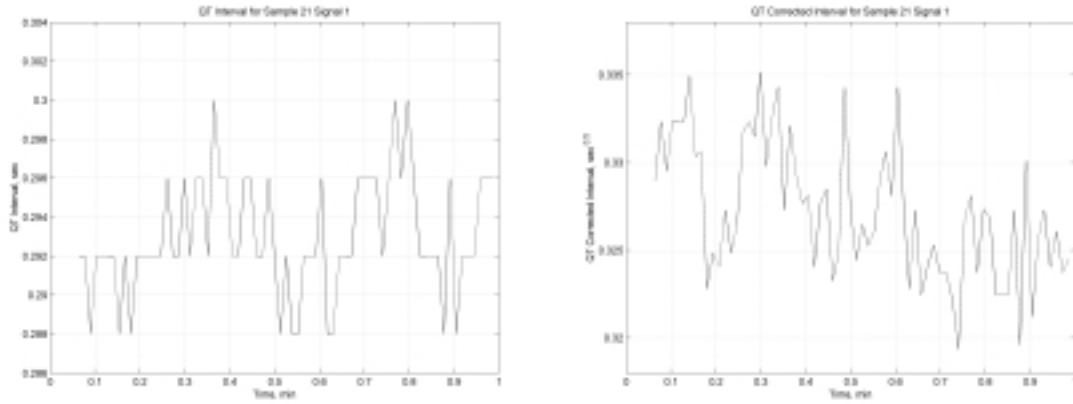


Figure A-42. ECG Sample 21 Signal 1 QT Interval and QTc Interval

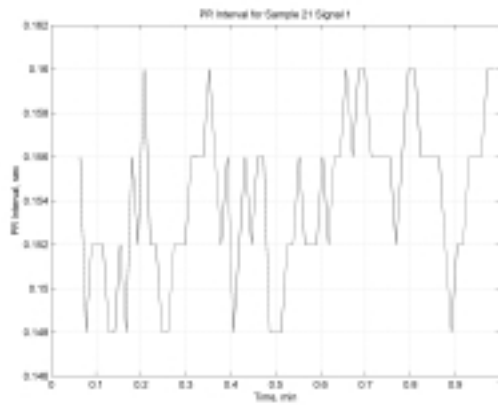


Figure A-43. ECG Sample 21 Signal 1 PR Interval

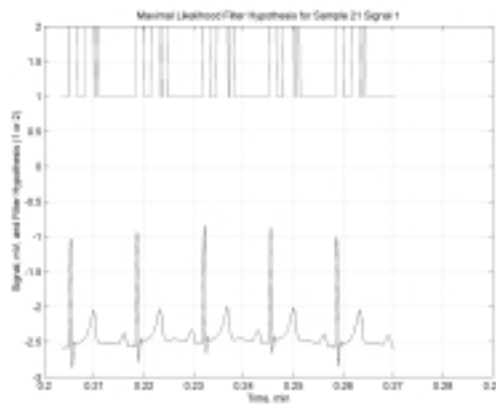


Figure A-44. Maximal Likelihood Filter Hypothesis for Sample 21 Signal 1

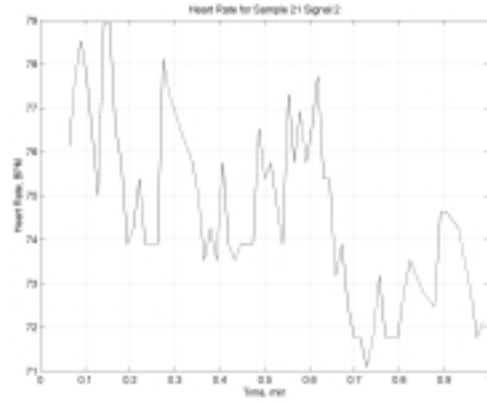


Figure A-45. ECG Sample 21 Signal 2 Heart Rate

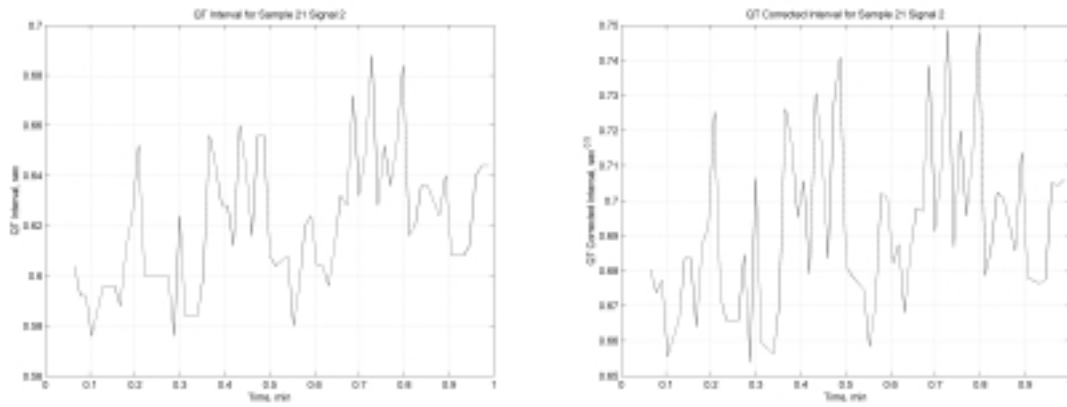


Figure A-46. ECG Sample 21 Signal 2 QT Interval and QTc Interval

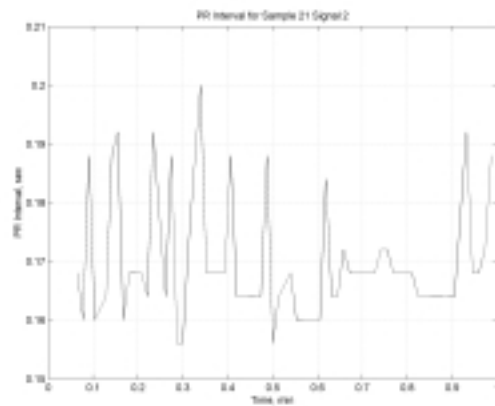


Figure A-47. ECG Sample 21 Signal 2 PR Interval

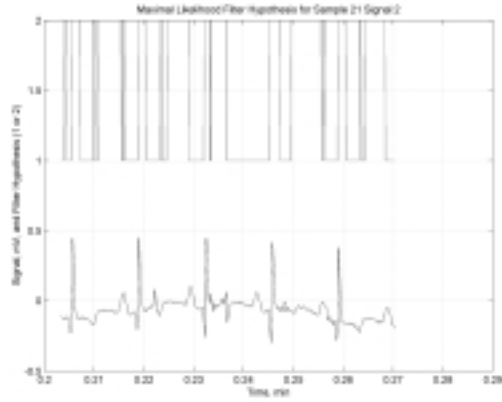


Figure A-48. Maximal Likelihood Filter Hypothesis for Sample 21 Signal 23

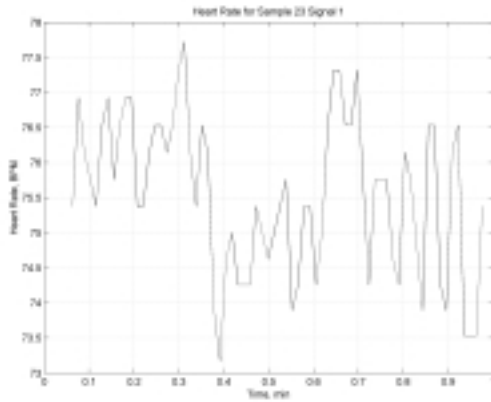


Figure A-49. ECG Sample 23 Signal 1 Heart Rate

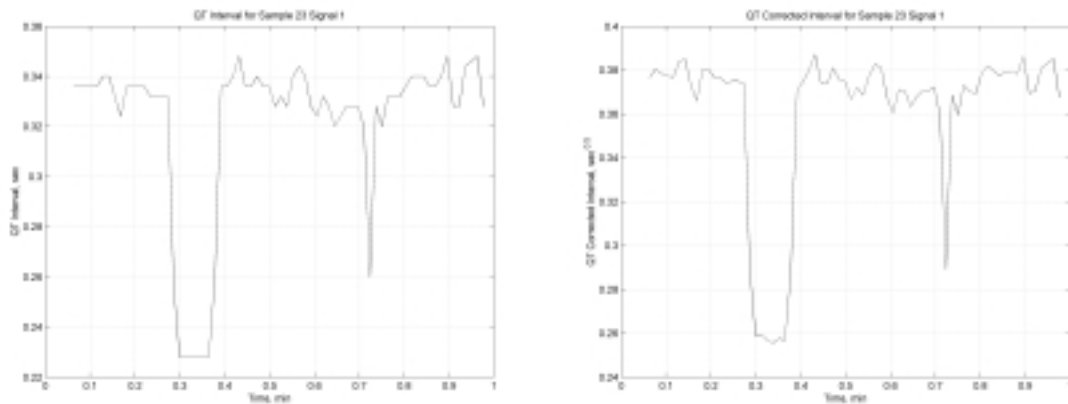


Figure A-50. ECG Sample 23 Signal 1 QT Interval and QTc Interval

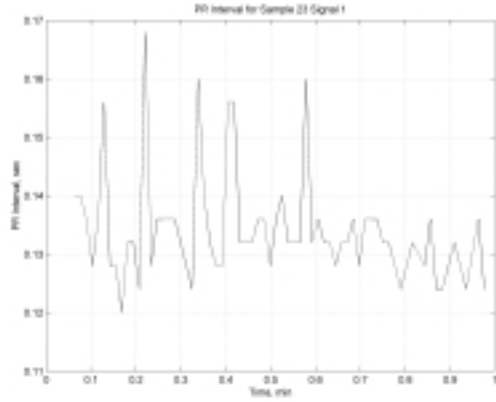


Figure A-51. ECG Sample 23 Signal 1 PR Interval

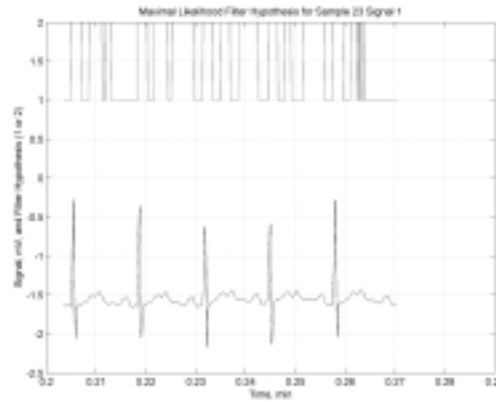


Figure A-52. Maximal Likelihood Filter Hypothesis for Sample 23 Signal 1

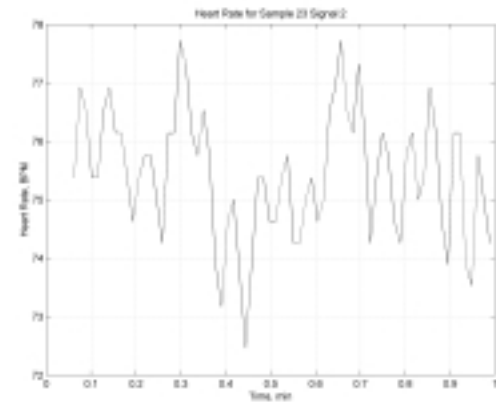


Figure A-53. ECG Sample 23 Signal 2 Heart Rate

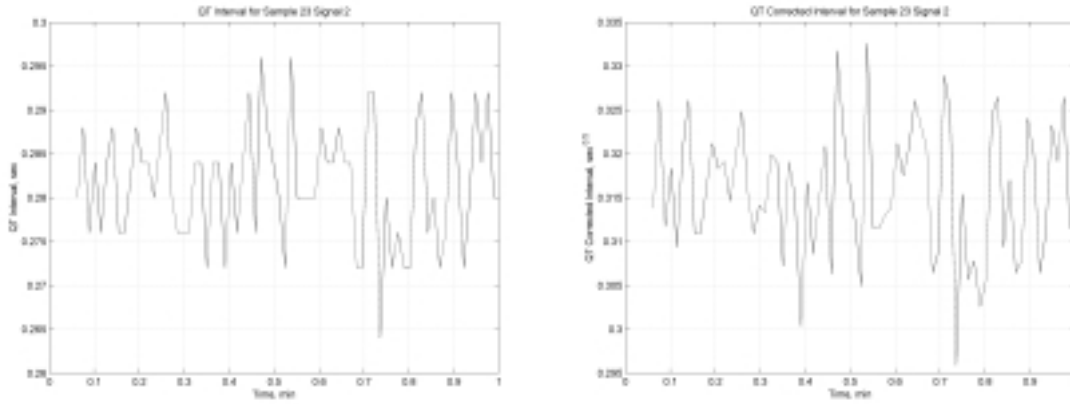


Figure A-54. ECG Sample 23 Signal 2 QT Interval and QTc Interval

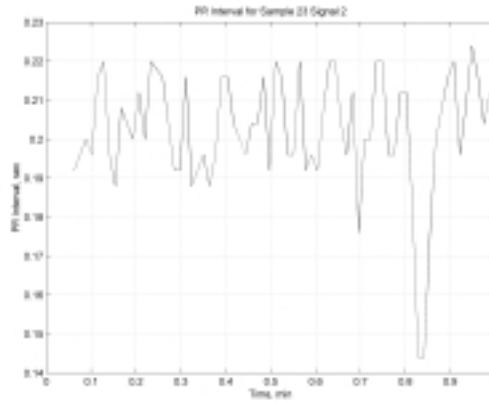


Figure A-55. ECG Sample 23 Signal 2 PR Interval

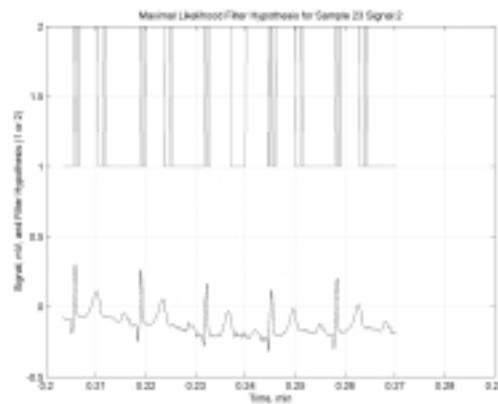


Figure A-56. Maximal Likelihood Filter Hypothesis for Sample 23 Signal 2

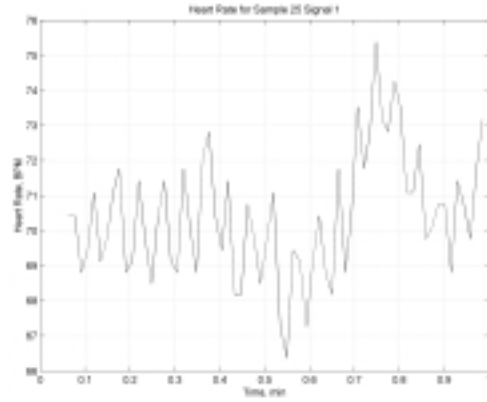


Figure A-57. ECG Sample 25 Signal 1 Heart Rate

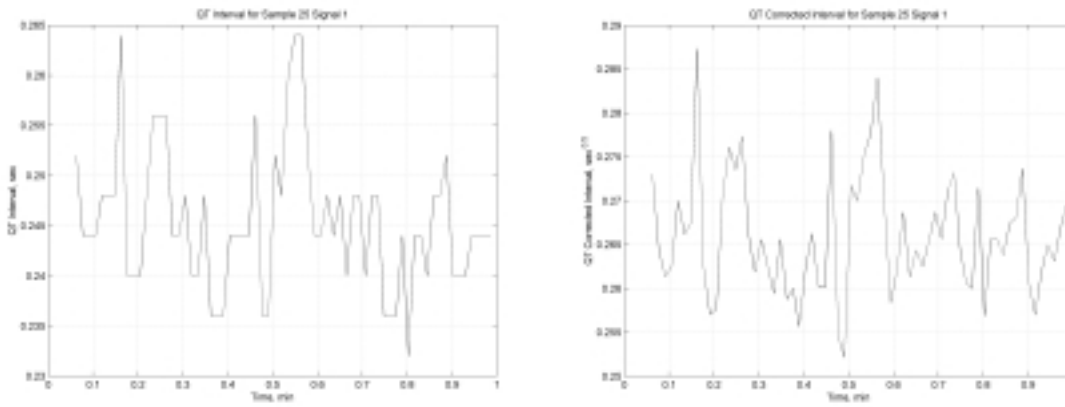


Figure A-58. ECG Sample 25 Signal 1 QT Interval and QTc Interval

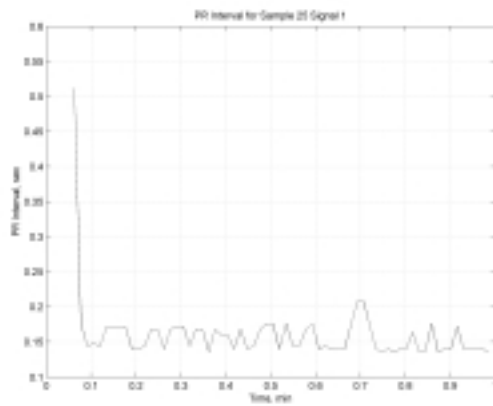


Figure A- 59. ECG Sample 25 Signal 1 PR Interval

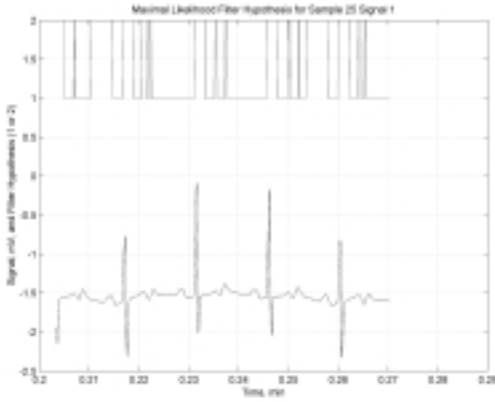


Figure A-60. Maximal Likelihood Filter Hypothesis for Sample 25 Signal 1

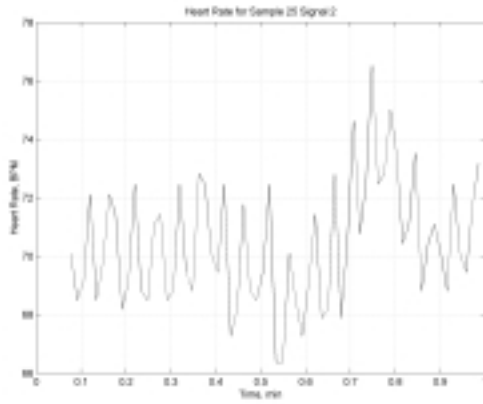


Figure A-61. ECG Sample 25 Signal 2 Heart Rate

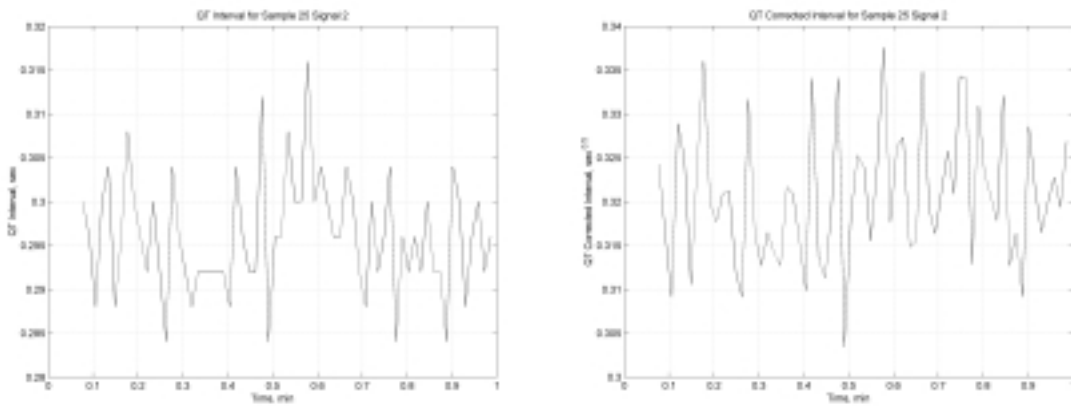


Figure A-62. ECG Sample 25 Signal 2 QT Interval and QTc Interval

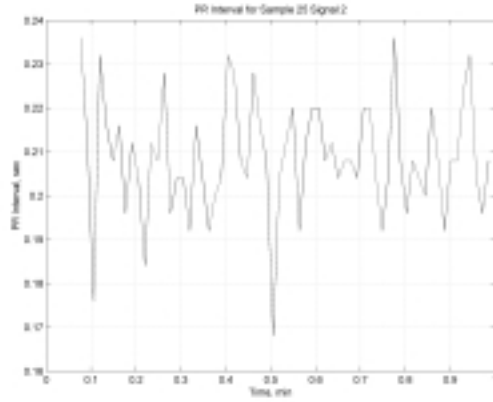


Figure A-63. ECG Sample 25 Signal 2 PR Interval

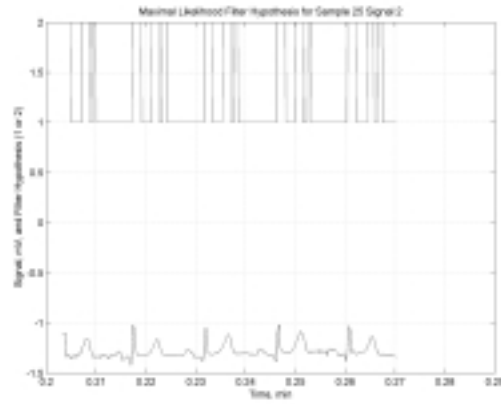


Figure A-64. Maximal Likelihood Filter Hypothesis for Signal 25 Sample 2

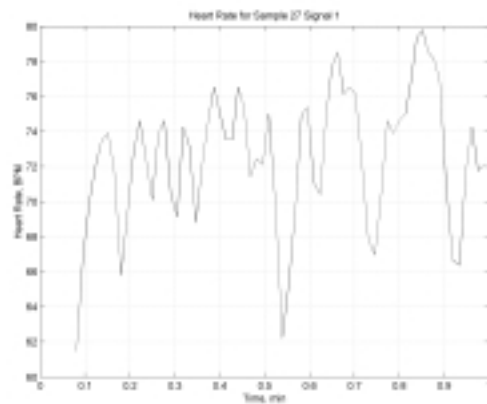


Figure A-65. ECG Sample 27 Signal 1 Heart Rate

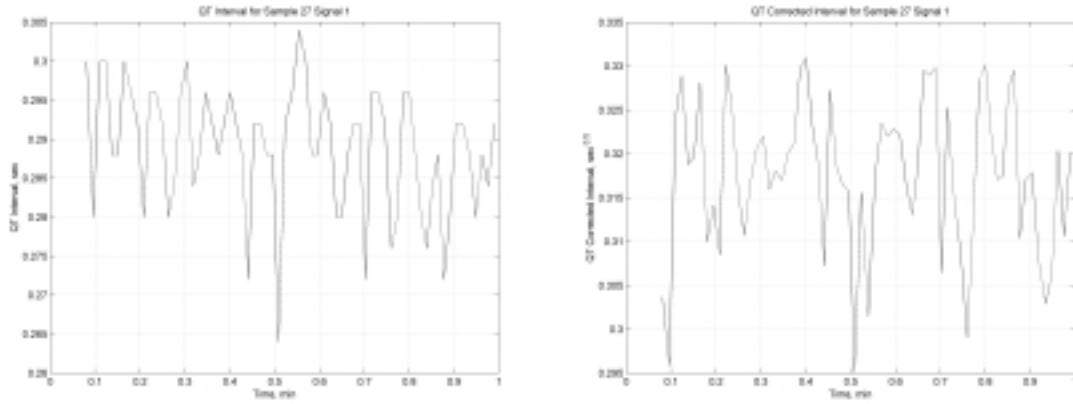


Figure A-66. ECG Sample 27 Signal 1 QT Interval and QTc Interval

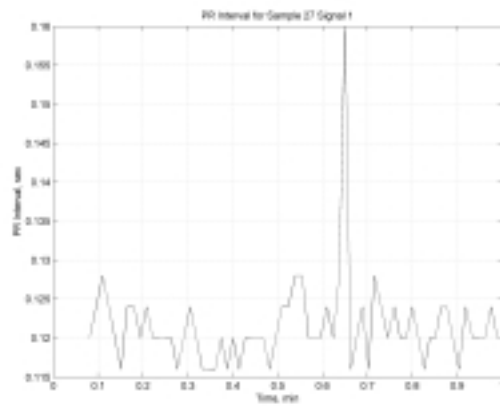


Figure A-67. ECG Sample 27 Signal 1 PR Interval

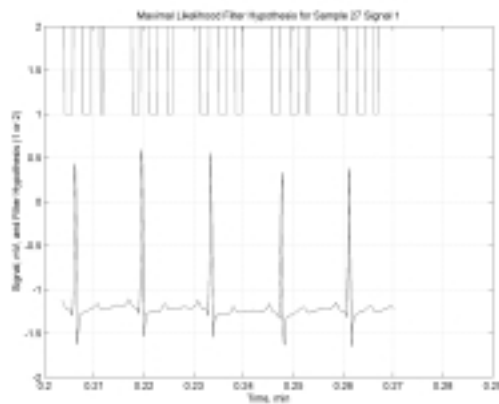


Figure A-68. Maximal Likelihood Filter Hypothesis for Sample 27 Signal 1

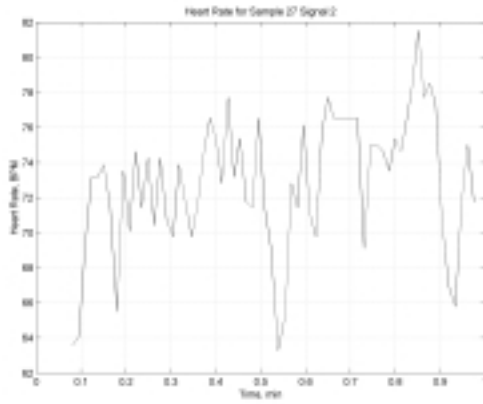


Figure A-69. ECG Sample 27 Signal 2 Heart Rate

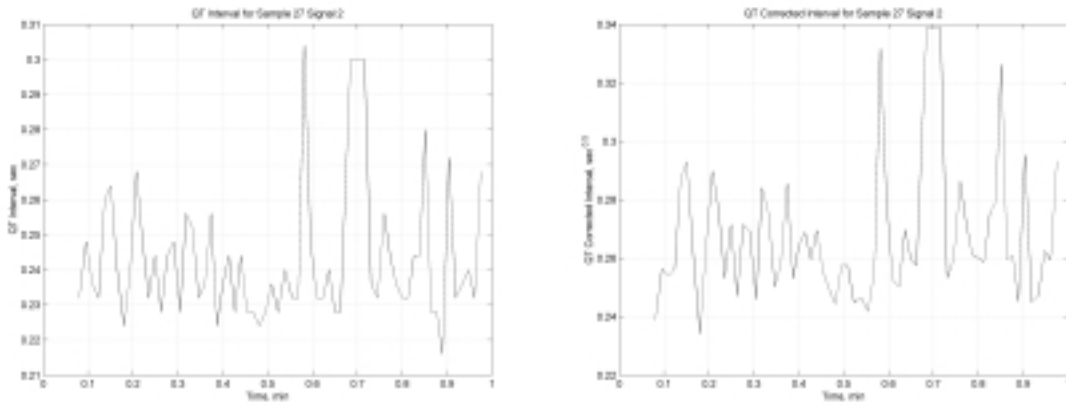


Figure A-70. ECG Sample 27 Signal 2 QT Interval and QTc Interval

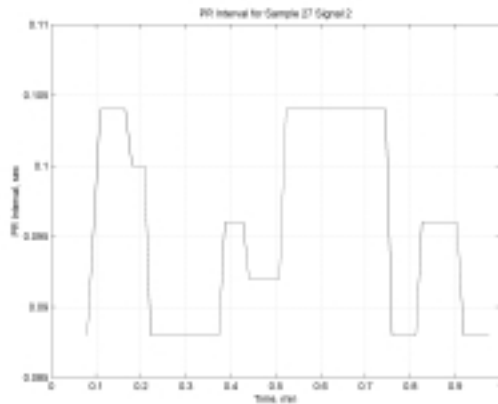


Figure A-71. ECG Sample 27 Signal 2 PR Interval

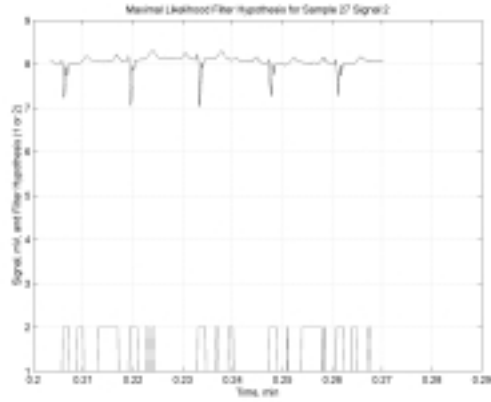


Figure A-72. Maximal Likelihood Filter Hypothesis for Signal 27 Sample 2

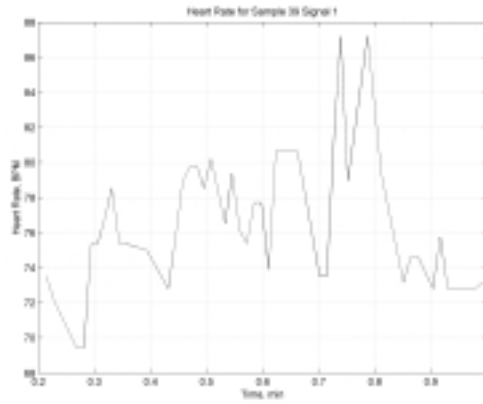


Figure A-73. ECG Sample 39 Signal 1 Heart Rate

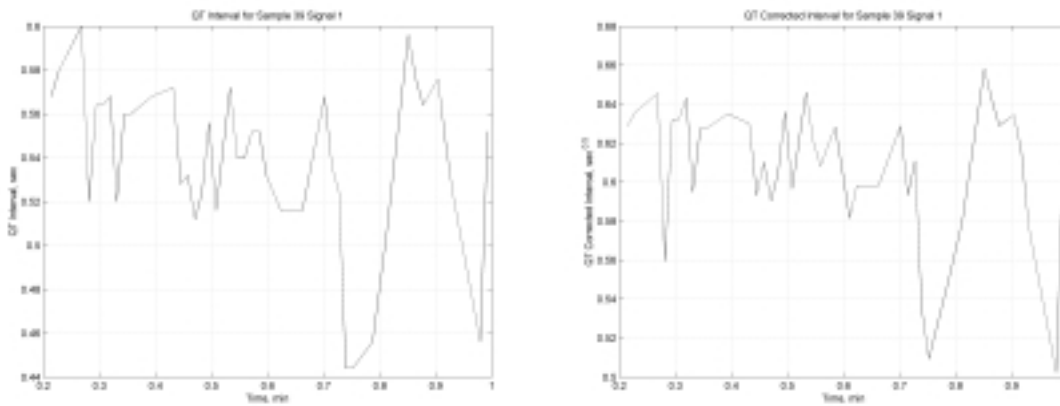


Figure A-74. ECG Sample 39 Signal 1 QT Interval and QTc Interval

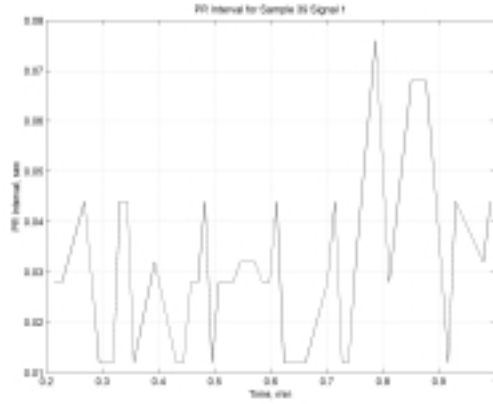


Figure A-75. ECG Sample 39 Signal 1 PR Interval

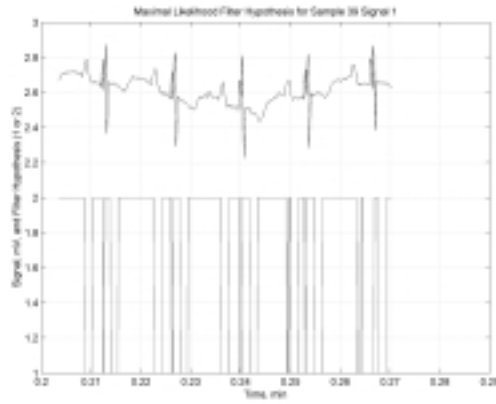


Figure A-76. Maximal Likelihood Filter Hypothesis for Sample 39 Signal 1

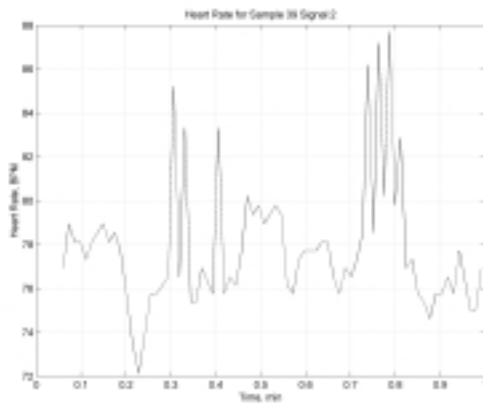


Figure A-77. ECG Sample 39 Signal 2 Heart Rate

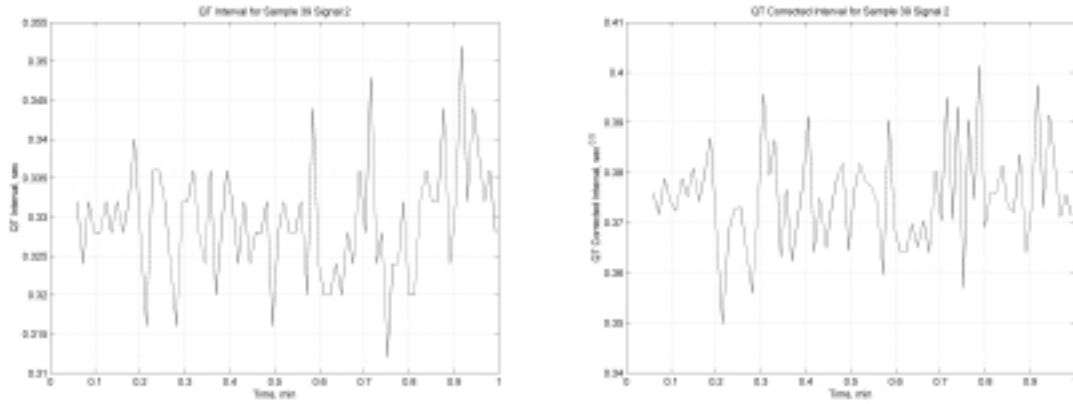


Figure A-78. ECG Sample 39 Signal 2 QT Interval and QTc Interval

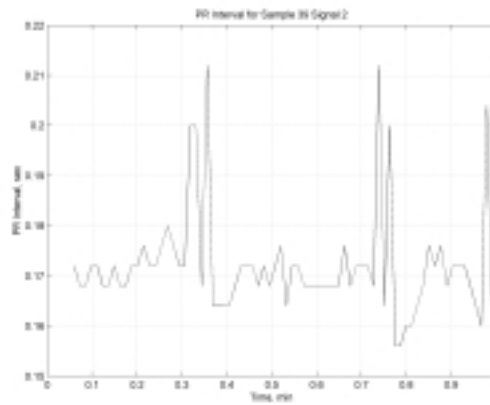


Figure A-79. ECG Sample 39 Signal 2 PR Interval

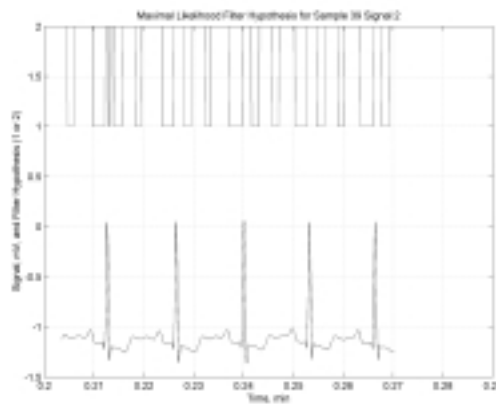


Figure A- 80. Maximal Likelihood Filter Hypothesis for Signal 39 Sample 2

Appendix B. ION GPS-2001 Paper

This appendix is a paper written for the ION GPS-2001 Conference in Salt Lake City, UT in September 2001. This paper describes the long-term research goals for the personnel navigation and physiological monitoring system. This research lays a foundation for the physiological warning indication system that the base station personnel will use during the monitoring process.

Real Time Personal Positioning and Physiological Monitoring System

Hoffman, Gregory S., *Air Force Institute of Technology*
Miller, Mikel M., *Air Force Institute of Technology*

BIOGRAPHY

2Lt Gregory Hoffman is a Graduate Student at the Air Force Institute of Technology (AFIT). He graduated from the United States Air Force Academy in May 2000 with a bachelor's degree in Electrical Engineering.

Lt Col Mikel Miller is an Assistant Professor of Electrical Engineering at the Air Force Institute of Technology where he is responsible for teaching and research related to integrated GPS and inertial navigation systems. He has been involved with GPS testing and development since 1989.

ABSTRACT

An integrated system using a small, lightweight GPS receiver and physiological sensors is currently under development to monitor the health and performance of a team of outdoor workers, such as forest fire fighters, operating in hazardous situations. Knowing each team member's physiological status and location is critical in performing dangerous missions in as safe and effective manner as possible. By monitoring each team member's position and physical well being, the person coordinating a dangerous activity will be able to maximize the efficiency of the team from a location and performance standpoint.

This paper presents the preliminary design of a real-time, lightweight, non-intrusive, and wearable vest capable of monitoring a person's outdoor location and physiological well-being. An array of sensors including electrocardiography, blood volume pulse, skin temperature, and respiration rate are transmitted along with GPS position information to a remote base station. A mission coordinator can use a laptop computer for real-time processing and analysis of the physiological data for signs of performance degradation, that may signal a need for relief. Advanced software gives warning indications when physiological parameters are not in the proper range, making the job of monitoring large groups easier.

By showing the correlation between performance (work

quality), physiological data, and GPS provided position, one can effectively monitor a team member's well being and safety from a remote base station.

INTRODUCTION

Little research has been done correlating the vital sign parameters and job performance of people working in hazardous environments. Is it possible to predict performance to not allow a person to enter a dangerous situation if physiological parameters are not in required (safe) ranges? In addition, is it possible to monitor the vital signs and position of a person or team while they are working? A real-time system allowing the physiological and position monitoring of workers would create a safer work environment and may increase the efficiency of the work effort.

For example, a forest fire fighter battling a quickly moving brush fire may become fatigued. As dehydration and heat stress or other dangerous physical conditions set in, the person may dwell on job performance and not on the declining, and potentially dangerous decrease in physiological condition. Knowing the physiological health and position of the fire fighter, the fire chief can order a rested replacement to the precise location, ensuring both increased team efficiency and team safety.

In addition, combat requires precise situational awareness by a commander to ensure that the mission is accomplished quickly and efficiently while minimizing the loss of life. At times, key missions are given to Special Forces teams, hinging the mission outcome on the ability of the team to complete the assignment in the required timeline. If the team encounters unforeseen difficulties, a commander needs this information immediately. Thus, timely decisions can be made including reinforcing the team, sending in search and rescue personnel to extract the team, or letting the team continue without interference.

Other situations or jobs may also benefit from real-time monitoring from a central control station. Doctors could monitor patients who remain in the comfort of their own home, performing their daily routine. Coaches can tailor

training plans for athletes, given the immediate feedback of real-time monitoring. Combat pilots could wear a monitoring system that one day would be linked with the avionics package, ensuring that if the pilot loses consciousness, the aircraft can attempt to recover itself to a safe ejection altitude and attitude. Finally, real-time monitoring could aid the search and recover effort of downed aircrew members.

PHYSIOLOGICAL RESEARCH TO DATE

Extensive research at AFIT into motion sickness using electroencephalography (EEG) sets a precedent for physiological research at this institution [3], [50], [56], [63]. AFIT has worked with the Air Force Research Lab Human Effectiveness Directorate's (AFRL/HE) motion sickness research. AFRL/HE studies the effects of various levels of gravity (g's) in a centrifuge while using various techniques trying to overcome physical difficulties when flying.

The National Aeronautics and Space Administration (NASA) is very interested in the causes of motion sickness. Using non-invasive physiological monitoring, NASA has developed a biofeedback system that will train people to gain control of their physiological responses. The system is much more compact than the system used onboard the aircraft, using sensors attached to a shirt, a belt mounted recording device, and a wrist display unit. The system can measure ECG, electromyography (EMG) of leg and arm muscles, electroencephalography (EEG), electro-oculography (EOG), electrogastrography (EGG), skin temperature, blood volume pulse, blood pressure, and skin conductance levels. Also, tri-axial accelerometers are used to give the position of the head. The data recorder also includes electronic circuitry to process the data, batteries, and computer connections [47].

Relating physiological parameters to a person's work is also of interest. Nakra [46] created the Conductor's Jacket to measure physiological parameters and gestures of a symphony conductor during a performance. Essentially a tuxedo jacket with physiological sensors woven in, 16 different parameters were analyzed in real-time on a personal computer. The physiological parameters include respiration rate, heart rate, galvanic skin response (GVR), and muscle activity. Analysis of the physiological responses of the conductor and the music revealed strong correlation between the conductor's gestures, physiological responses, and tendencies with the dynamics of the music.

The Indy Racing League (IRL) is interested in using physiological monitoring to increase the safety of its drivers. Using the LifeShirt® by Vivometrics, an Indy car driver was monitored during the 2001 Indy 500. Dr. Steve Olvey, CART Racing Medical Director, suggests

that knowing the physiological parameters of the driver during race will help crews increase the safety of the driver and will allow medical teams to understand the severity of injuries immediately after a crash. Understanding how the body responds to the stress of a race can also lead to better training regimens [45].

Wearable sensor systems are also being developed by others. The Defense Advanced Projects Research Agency (DARPA) recently sponsored an initiative to develop a system that will enable the Medical Corps to perform "virtual triage." Designated the Georgia Tech Wearable Motherboard™ (GTWM), the creators suggest that for the first time there is a systematic way to monitor vital signs unobtrusively. Plastic fiber optic cords are woven into the shirt, which also allows the shirt to sense "projectile penetration." While the shirt was originally developed to minimize loss of life on the battlefield and to assist triage procedures, it also lends itself well to civilian healthcare scenarios. Much like the dental community has shifted its focus to preventative care, the GTWM could focus other health care communities from "treatment to prevention through wellness." Taking a virtual reality approach to health care, the GTWM could improve the quality of care while reducing costs [14].

The GTWM uses a flexible wiring bus to connect the sensors. It also incorporates DARPA's personnel status monitor (PSM) type of sensor connectors, enabling the shirt to include previously developed non-invasive sensor technology. While the shirt sounds intriguing, only respiration, ECG, and projectile monitoring have been tested [14]. The shirt has a capability to use other sensors such as environmental carbon dioxide (CO₂) sensors, useful in fire-fighting applications, voice monitors, and other physiological sensors. The shirt also has several other applications because of its configurable and tailored design. These applications include sports or performance, fire fighter, or law enforcement, specialized health care including telemedicine, and aircrew monitoring [14].

Other areas of interest are physiological responses to exercise, including the relationship of perceived work and performance. While heart rate monitors available today can tell a runner or biker his heart rate, and some can even store data, there is no correlation between the heart rate and position in a run or ride. For example, if a runner's heart rate increases rapidly over a 30 second interval, did the increase occur because he run up a hill or increase his pace? An intriguing new development is the ability to place a GPS receiver on a person and collect heart rate data at the same time. By using position, velocity, and heart rate information as another training aid in a coach's "tool box," racers will increase their performance. Using evaluation software on a personal computer (PC), GPS data and heart rate data were displayed in graph form showing heart rate, position and instantaneous velocity.

A second prototype will include a spread spectrum transceiver so that real-time monitoring can occur. Using an OEM GPS receiver card, batteries, a microcontroller, a 900 MHz transceiver system, and real-time software, a coach can monitor the pace and give instantaneous feedback if his runner or biker needs to speed up or slow down to meet training goals [42].

Finally, real time monitoring in perhaps the harshest of conditions was accomplished in 1999. Dr. Richard Satava at Yale University used a vital signs monitoring system (VSM) including ECG, heart rate and skin temperature sensors, a GPS receiver, and a transceiver, to monitor climbers on Mount Everest from a base station. FitSense Technologies designed the system which can be custom configured for other applications. Using radio frequency (RF) transmission, each of the sensors was connected to a data hub where the data was time stamped using GPS time. Up to 16 sensors can be supported by the VSM, with up to 16 people in the same area. Running for 10 days on two AA batteries, the system collected data every 15 seconds and transmitted data every 5 minutes, although the transmission rate is adjustable. The system has a serial port for connection to a PC, Palm Pilot, or similar. From the base station, data was transmitted using a TCP/IP satellite connection and then onto the Internet. Data was then displayed on a graphical user interface (GUI), which easily allowed changing to different climbers. The authors remark that numerous applications of the VSM such as hospitals, nursing homes, space, and others are possible given that the VSM worked so well in extreme environments, and that as more non-invasive sensors are added to the system, the “physiologic cipher will become less of a mystery and more of a quality control asset” [53].

THE GPS ADVANTAGE

GPS provides an information advantage previously not attainable when monitoring patients. Position anywhere on the Earth can now be determined very precisely with a GPS receiver. Using GPS, correlation between physiological “events” and position give new insights into the physiological response of the body at a given instant in time and a given location. This correlation will lead to new training methods for athletes, increased job safety in dangerous working environments, increased information for commanders of military forces, law enforcement, or public safety personnel.

GPS currently uses a constellation of 31 satellites in a medium earth orbit of 10,900 nautical miles (26,560 km) or 20,200 km above the earth.

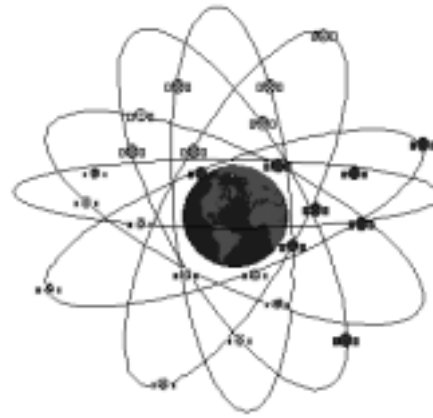


Figure B- 1. GPS Constellation

Each satellite in the constellation transmits two different codes: the coarse/acquisition code (C/A) and the precision (encrypted) [P(Y)] code. The chipping rate of the C/A code is 1.023MHz and repeats every 1 ms. The chipping rate of the P(Y) code is 10.23 MHz and repeats every seven days. The higher chipping rate of the P(Y) code results in more precise range measurements than for the C/A code. The C/A code is modulated on a 1575.42 MHz carrier frequency (L1) and the P(Y) code is modulated on the 1575.42 MHz carrier and a 1227.60 MHz carrier frequency (L2). An ephemeris message transmitted at 50 Hz includes satellite clock correction parameters, satellite position and velocity parameters, and an almanac for all satellites. The ephemeris message and clock parameters repeat every 30 seconds while the almanac repeats every 12.5 minutes [44].

A GPS receiver has five basic functions: 1. Receiver RF signals from each visible satellite; 2. Separate the signals from each satellite; 3. Determine signal transmit time and Doppler shift; 4. Decode navigation message to determine satellite position; 5. Estimate user position velocity, and time. When the receiver is first turned on, it must search through all of the possible satellites and determine which satellites are visible. Once all of the satellites in view are acquired and locked, the receiver can begin to estimate position, velocity, and time [44].

Because the transmit time is inherent in the GPS signal, when the receiver is locked onto a satellite, it knows when the signal was sent and where the satellite was in the orbit at time of transmission. Knowing, the transmit time (from the signal itself) and the receive time (from the receiver clock), a pseudorange between the receiver and the satellite can be calculated. Essentially, the receiver must solve a linear algebra problem with four unknowns: X receiver position, Y receiver position, Z receiver position, and receiver clock error. Thus, the receiver needs at least four satellites in view to estimate position, velocity, and time.

RESEARCH OBJECTIVES

This research focuses on a real-time monitoring system including wearable physiological sensors, a GPS receiver, wireless transmission capabilities, and monitoring software. Physiological sensor and GPS information of a team member will be transmitted to a base station where the control station personnel will visually inspect the vital signs and position parameters of each person for signs of physical impairment or other problems that may lead to a hindrance in completing the mission. The software will display information for any number of the team members, with the selectable vital signs of interest, in an organized and easy to interpret format. Residual monitoring and filtering algorithms, failure detection algorithms, or other software will alert the monitor to dangerous physiological parameters. Knowledge of an individual's precise location when dangerous parameters occur facilitates the process of immediately acting to remove the individual to safety where he may receive appropriate medical attention.

USER REQUIREMENTS

The users of this system will operate in extreme environments including extreme heat, rain, and dirt and dust. A person wearing this system will be very physically active, which may include running, crawling, rolling and climbing. Thus, the system needs to be lightweight and comfortable for the wearer. The system must be easy to don such that the sensors and other hardware are properly placed on the body. Correct placement of the sensors on the body is paramount to ensure that accurate monitoring occurs. The sensors need to be non-invasive, such that the wearer is not hindered by their presence.

The system needs to transmit the physiological and position information up to approximately 20 miles in an outdoor environment. (Future work will focus on integrating an indoor and outdoor transmission system capable of the physical location and physiological monitoring.) Secure communication is not required at this time, but may be apart of future work.

The sensors and other hardware worn by the user are only half of the system. Software and a graphical user interface (GUI) allow position and physiological information of a team to be viewed in real-time. The team coordinator can quickly switch between physiological parameters of interest or team members of interest. The software alerts the monitor to potentially hazardous physiological parameters. The monitoring personnel need not be medical practitioners to monitor the team. Any person, such as a fire chief or military commander, should be able to effectively use this software to ensure the safety and efficiency of the team after a short training course.

The following sensors are required for accurate estimation of physiological health: electrocardiogram (ECG or EKG), respiration, pulse oxygen saturation, and skin temperature. (Other sensors will be researched, including electroencephalography (EEG) and environmental CO₂ for certain applications). An EKG sensor measures the electrical activity of the heart. Useful information includes the heart rate and electrical waveform. The waveform should follow the standard "P, Q, R, S, T, U" distinct electrical events in the heart [29].

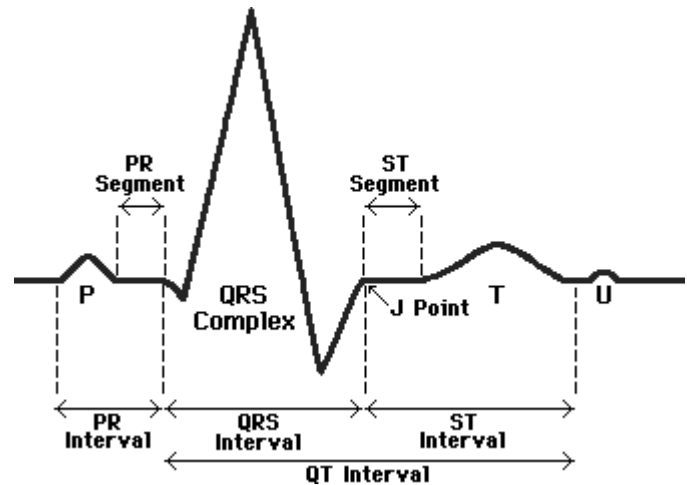


Figure B-2. ECG Characteristic Waveform [29]

The time between "R" events follows a periodic oscillation known as the sinus arrhythmia. A Fast Fourier Transform can show the degree of oscillation and can provide indications of dangerous physiological parameters if the normal sinus arrhythmia is not present [58].

The respiration sensor gives indications of respiration rate and insight into breathing quality. Two sensor locations are generally acceptable -- on the chest on the abdominal. One may wish to use both locations to get a better understanding of an individual's breathing pattern. Generally, one will see an increase in chest breathing when a person is excited, experiencing the effects of an aroused sympathetic nervous system. Oppositely, one will see abdominal breathing dominate chest breathing when a person relaxes.

A pulse oxygen sensor utilizes two wavelengths of light, one in the infrared spectrum (sensitive to oxy-hemoglobin) and another in the red spectrum (sensitive to de-oxy-hemoglobin). The amount of light passing through the tissue, to include blood vessels is measured using a photo detector. Thus, pulse oximetry gives indications of blood oxygen content and heart rate. The heart rate from the pulse oxygen sensor is a cross-check of the EKG heart rate. While the respiration sensor will give indications as to how fast and how deeply a person is breathing, the oxygen content of the blood will relate the

respiration rate to how well the lungs are functioning. One drawback to pulse oximetry is that it can give spuriously high oxygen levels in the presence of carbon monoxide (CO) [33]. The pulse oxygen sensor does not give the amount of carbon dioxide (CO₂) in the blood. In applications such as fire fighting, it may be useful to use an environmental CO₂ detector.

DESIGN

First design prototypes will use a commercial off-the-shelf sensor package called LifeShirt®. The LifeShirt® is currently seeking FDA approval for medical applications; however, because the LifeShirt® uses previously approved sensors and sensor data processing algorithms, the approval of the vest and sensor system is not a concern at this time. Currently, the LifeShirt® includes EKG and respiration sensors. The sensor data is sampled by a microcontroller and stored in a hand-held computer. After a monitoring session is over, the data is sent via the internet or mailed to Vivometrics for processing.

Work with the LifeShirt® includes the incorporation of the sensors of interest, making the system wireless, designing real-time monitoring software, and validating the software against the results of post-processed data from Vivometrics.

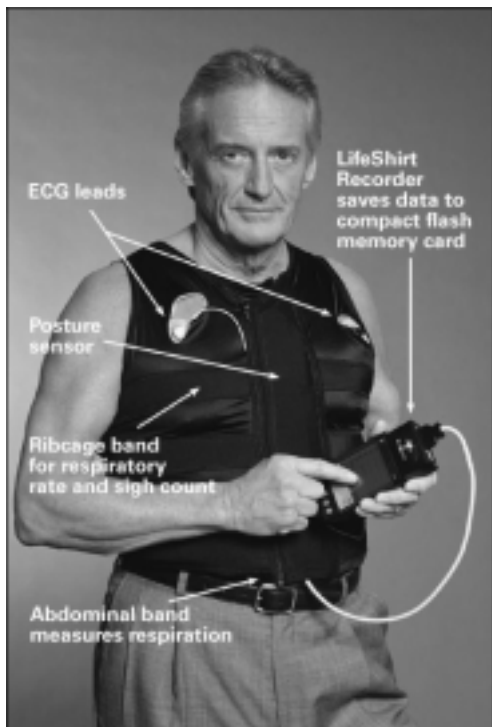


Figure B-3. LifeShirt® sensor vest and wired data recorder [61]

A FreeWave 900 MHz transceiver is used as the wireless transmission device. The FreeWave uses the RS-232 asynchronous communication standard. Thus, the data is

packaged in eight bit bytes. The FreeWave transceiver has a range of approximately 20 miles, line of sight.

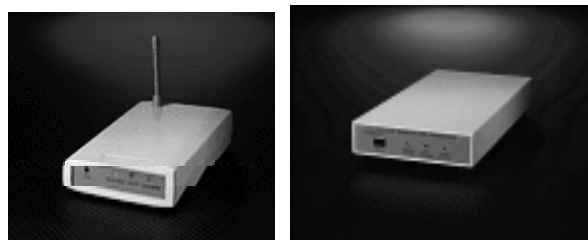


Figure B-4. Freewave transceiver system

The Superstar GPS receiver will be used. It is a 12-channel GPS receiver OEM module approximately the size of a pager. A life-size picture is seen below:



Figure B-5. Superstar receiver OEM module [15]

The Superstar can output selected NMEA messages including GGA, GSA, GSV, RMC, VTG, ZDA, and GLL. This research effort only requires position and velocity information, so the recommended minimum message (RMC) is used. This also facilitates the maximum transmission of physiological data. The Superstar outputs position and velocity in RS-232 format, which is important for data transmission.

The LifeShirt® sensors are sampled by the microcontroller and packaged in RS-232 format. Thus, this data is also in the proper format for transmission. (Work with Vivometrics may include upgrading the microcontroller to be able to include more sensors or include the GPS right into the microcontroller).

The improved sensor package also includes the pulse oximetry sensor. This sensor is a “hospital grade” Nonin fingertip sensor with Xpod data processing board. The

Nonin data is in serial format and thus capable of integration with the GPS receiver and other sensors. A drawback to the Nonin Xpod is the baud rate of 9600, which may limit the amount of data that can be transmitted, and the Xpod is highly susceptible to motion artifacts.

CRITICAL ISSUES

Several critical issues are involved with this research. Data processing algorithms are already written, validated, and approved by the FDA for the various physiological sensors. The real-time software used in this application needs to be validated against these accepted algorithms. Thus, even when wireless transmission is capable, post processing done by Vivometrics will be used to validate the software. LifeShirt® has several patents on their software; a cooperative research and development agreement (CRADA) needs to be signed before algorithms can be shared. We need to develop real-time software capable of displaying team information, while maintaining the accuracy of the Vivometrics' algorithms.

Other issues include physiological sensor errors called motion artifacts. When the body moves, gravity or other forces cause the capillaries or tissue under a sensor to change shape and volume. While these changes may be very small, the accuracy of the sensors during these conditions must be determined and is critical to the success of this research. Motion artifacts may incapacitate the sensor's ability to accurately measure the physiological parameter of interest.

DATA COLLECTION PHASES

Data will be collected in four phases: 1. Transmitting GPS and physiological data; 2. Transmitting LifeShirt® and GPS data; 3. Validating real-time algorithms against post-processed data from LifeShirt®; 4. Team monitoring with validated software. The focus of this research lies with the consequences or outcomes of real-time monitoring with coordination at a central control station. Thus, while the development and integration of the various sensors and systems is important, much work must be done to make the software and GUI easy to use, and to display data in a clear and concise manner. Currently there is great interest from local fire fighters to help test the real-time monitoring system during training exercises. Other test environments such as a battlefield scenario are also being considered.

The research is broken up into four phases, each with a critical milestone and culminates with the real-time monitoring of a team. Phase 1 milestone involves the integration of the GPS data and sensor data for wireless transmission. In this phase, the focus will be on using the Nonin pulse oximetry sensor for integration with the

Superstar GPS data. Critical to this phase is the ability to multiplex the two data streams and transmit the information with the FreeWave.

Phase 2 will focus on transmitting the LifeShirt® physiological data and the Superstar GPS data. Issues in phase 2 include choosing the appropriate data rates, ensuring that the transceiver can handle the desired data rate, and ensuring that the data rate is high enough for accurate representation of the various sensor data.

Phase 3 requires that the software developed for real-time monitoring is validated against the FDA approved Vivometrics algorithm. Data in phase three will be both post-processed by Vivometrics and processed in real-time by the research team. This ensures that the real-time processing algorithms are accurate and reliable. Ideally, the results should be identical; however, errors may be introduced when the data is multiplexed, transmitted, or received. Other areas tested in the phase are the comfort and convenience of the system design. Feedback will be taken from the test subjects and improvements will be incorporated.

Phase 4 culminates with the ability to monitor a team using the validated real-time processing algorithms and a GUI that displays the data to the team coordinator. Tests will be conducted using groups of fire fighters, military members, and others during training. The goals of this final phase are determining how well the GUI works, if it is easily used by the monitor at the central control station, and how well the integrated system works.

SUMMARY

This paper presents the motivation, user requirements, design, critical issues, and data collection phases for a real-time personal navigation and physiological monitoring system. The system will use a physiological sensor package from Vivometrics called LifeShirt® and a SuperStar GPS receiver OEM module as the main sensors. Using a FreeWave transceiver, data will be transmitted to the central control station where the team coordinator will view the data in real-time. Timely decisions can be made regarding the performance and safety of the team given the physiological and position information.

DISCLAIMER

The views expressed in this paper are those of the authors and do not reflect the official policy or position of the United States Air Force, Department of Defense, or the U.S. Government.

Bibliography

- [1] Amburn, Phillip. Qualia Computing, Inc. Beaver creek, OH. Personal Interview. 29 Jan 02.
- [2] Athans, M. et al. "The Stochastic Control of the F-8C Aircraft Using a Multiple Model Adaptive control (MMAC) Method—Part I: Equilibrium Flight," IEEE Transactions on Automatic Control, Vol. AC-22, No. 5, 768-78 (October 1977).
- [3] Banducci, Todd M. An Analysis of the Effects of Phenytoin in Treating Motion Sickness and the Effects of Motion Sickness on the Human Electroencephalogram. MS Thesis, AFIT/GSO/ENG/90D-2, School of Engineering, Air Force Institute of Technology (AU), Wright-Patterson AFB OH, November 1990 (ADA230423).
- [4] Bazzet, HC. "An Analysis of the Time Relations of Electrocardiograms," Heart, 7:353-67 (1920).
- [5] Botzer, L., B. Strasberg, and S. Abboud. "Dynamic QT-RR Relationships in 12 lead ECG in Patients with Coronary Artery Disease," Computer in Cardiology, 27:163-166 (2000).
- [6] Brennan, M., M. Palaniswami, and P.W. Kamen. "A New Cardiac Nervous System Model for Heart Rate Variability Analysis," Proceedings of the 20th Annual International Conference of the IEEE Engineering in Medicine and Biology Society. 349-352. New York: IEEE Press, 1998.
- [7] Burrus, C. S., R.A. Gopinath, and H. Guo. *Introduction to Wavelets and Wavelet Transforms*. Upper Saddle River: Prentice Hall, 1998.
- [8] Clark, Curtis S. Multiple Model Adaptive Estimation and Control Redistribution for the VISTA F-16 During Partial Actuator Impairments. MS Thesis, AFIT/GE/ENG/97D-23, School of Engineering, Air Force Institute of Technology (AU), Wright-Patterson AFB OH, December 1997 (ADA336725).
- [9] Detchmندی, D.M., and R. Sridhar. "Sequential Estimation of States and Parameters in Noisy Nonlinear Dynamical Systems," J. Basic Eng. (Tran. ASME), 362-368 (1966).
- [10] "The ECG Signal in More Detail."
http://www.cardionetics.com/docs/healthcr/ecg/deta_bd.htm. 30 Nov 01.

- [11] Eide, Peter K. Implementation and Demonstration of a Multiple Model Adaptive Estimator Failure Detection System for the F-16. MS Thesis. AFIT/GE/ENG/94D-06, School of Engineering, Air Force Institute of Technology (AU), Wright-Patterson AFB OH, December 1994 (ADA289301).
- [12] Fujisawa, Hiroyuki, Rakashi Uozumi, and Koichi Ono. "Evaluation of Autonomic Nervous System with Correlation Diagram of R-R Interval and P-R Interval," Proceedings of the 20th Annual International Conference of the IEEE Engineering in Medicine and Biology Society. 353-356. New York: IEEE Press, 1998.
- [13] Goldberger AL, Amaral LAN, Glass L, Hausdorff JM, Ivanov PCh, Mark RG, Mietus JE, Moody GB, Peng CK, Stanley HE. PhysioBank, PhysioToolkit, and Physionet: Components of a New Research Resource for Complex Physiologic Signals. *Circulation* 101(23): e215-e220 [Circulation Electronic Pages; <http://circ.ahajournals.org/cgi/content/full/101/23/e215>]; 2000 (June 13).
- [14] Gopalsamy, C., S. Park, R. Rajamanicham, and S. Jayaraman. "The Wearable Motherboard™: The First Generation of Adaptive and Responsive Textile Structures (ARTS) for Medical Applications," *Journal of Virtual Reality*, 4: 152-168 (1999).
- [15] GPS World Product page." Excerpt from product guide. n. pag. <http://www.gpsworld.com/products/suprstar.htm>. 14 Sep 01.
- [16] Gupta, N.K., W.E. Hall, Jr. "System Identification Technology for Estimating Re-entry Vehicle Aerodynamic Coefficients," *AIAA J. Guidance and Control*, 2: 139-146 (1979).
- [17] Gustafson, A.S., Willsky, and J.Y. Wang. "Final Report: Cardiac Arrhythmia Detection and Classification Through Signal Analysis." The Charles Stark Draper Laboratory, Cambridge, MS,. Report R-920 (July 1975).
- [18] Gustavsson, I. "Survey of Application of Identification in Chemical and Physical Processes," *Automatica*, 11: 3-24 (1975).
- [19] Handheld Pulse Oximeter—Digital Technology." http://www3.medical.philips.com/resources/hsg/docs/en-us/custom/handheldpulseoximeterdigtech_generic.asp 03 Feb 02.
- [20] Hanlon, Peter D. Failure Identification using Multiple Model Adaptive Estimation for the LAMBDA Flight Vehicle. MS Thesis. AFIT/GE/ENG/92D-19, School of Engineering, Air Force Institute of Technology (AU), Wright-Patterson AFB OH, December 1992 (ADA259137).

- [21] Hanlon, Peter D. and Peter S. Maybeck. "Multiple-Model Adaptive Estimation Using a Residual Correlation Kalman Filter Bank," IEEE Transactions of Aerospace and Electronic Systems, 36: 393-406 (April 2000).
- [22] Harrington, Ronald R, and Oleh W. Hnatiuk. "Non-Invasive Monitoring," The American Journal of Medicine, 95: 221-228 (August 1993).
- [23] Henderson, Paul E. Development and Testing of a Multiple Filter Approach for Precise DGPS Positioning and Carrier Phase Ambiguity Resolution. MS Thesis, AFIT/GE/ENG/01M-15, School of Engineering, Air Force Institute of Technology (AU), Wright-Patterson AFB OH, March 2001.
- [24] "How Does Pulse Oximeter Work." http://gasbone.herston.uq.edu.au/teach/su602/docs/d19_3pox.html 03 Feb 02.
- [25] Kabrisky, Matthew. Professor Emeritus, Air Force Institute of Technology, Wright-Patterson Air Force Base, OH. E-mail. 01 Mar 02.
- [26] Kabrisky, Matthew. Professor Emeritus, Air Force Institute of Technology, Wright-Patterson Air Force Base, OH. Personal Interview. 14 Dec 01.
- [27] Klabunde, Richard E. "Cardiovascular Physiology Web Resource" <http://www.oucom.ohiou.edu/CVPhysiology/A013.htm> 30 Nov 01.
- [28] Klefors, Daniel. "Artificial Neural Networks." Saint Louis University School of Business and Administration. <http://hem.hj.se/~de96klda/NeuralNetworks.htm>. 03 Feb 02.
- [29] Klimes, R. "EKG Review: Characteristics and Interventions." Excerpt from online course. n. pag. <http://www.ce5.com/ekg100.htm>. 14 Sep 01.
- [30] Koski, Antti. On Structural Recognition and Analysis Methods Applied to ECG Signals. PhD. Dissertation. University of Turku, Finland. Research Reports R-97-1.
- [31] Lewis, Robert W. Multiple Model Adaptive Estimation and control Redistribtuion for the VISTA F-16. MS Thesis. AFIT/GE/ENG/96D-29, School of Engineering, Air Force Institute of Technology (AU), Wright-Patterson AFB OH, December 1996 (ADA324050).
- [32] Lund, Elvind, J. On-line Discrimination and Estimation in Multiple Regime Systems. PhD. Dissertation, Division of Engineering Cybernetics, The Norwegian Institute of Technology University of Trondheim, Trondheim, Norway, June 1992.

- [33] Martin, Daniel, Scott Powers, Michael Cicale, Nancy Collop, David Huang, and Dave Criswell. "Validity of Pulse Oximetry During Exercise in Elite Endurance Athletes," *Journal of Applied Physiology*, 72: 455-458 (1994).
- [34] Maybeck, P.S., D.A. Harnly, and R.L. Jensen. "Robustness of a New Infrared Target Tracker," *Proc. IEEE Nat Aerospace and Electron. Conf.*, Dayton, OH, 639-644 (May 1980).
- [35] Maybeck, P.S., R.L. Jensen, and D.A. Harnly. "An Adaptive Extended Kalman Filter for Target Image Tracking." *IEEE Trans Aerospace Electron, Syst.*, AES-17:172-180 (1981).
- [36] Maybeck, P.S., S.J Cusumano, M. DePonte Jr, and J.E. Negro. "Enhanced Fire Control System Filtering via Refined Air-to-Air Missile Acceleration Modeling." *Proc. 1978 IEEE Conf. Decision and Control*, San Diego, CA (January 1979).
- [37] Maybeck, Peter S. *Class Notes to EENG 768*, Air Force Institute of Technology, Wright-Patterson AFB, Summer Quarter 2001.
- [38] Maybeck, Peter S. and Donald L. Pogoda. "Multiple Model Adaptive Controller for the STOL F-15 with Sensor/Actuator Failures," *Proceedings of the 28th IEEE Conference on Decision and Control*, 1566-157. Tampa, Florida: December 1989.
- [39] Maybeck, Peter S. *Stochastic Models, Estimation and Control, I*. New York: Academic Press, Inc. 1979. Republished Arlington VA: Navtech, 1994.
- [40] Maybeck, Peter S. *Stochastic Models, Estimation and Control, II*. New York: Academic Press, Inc. 1982. Republished Arlington VA: Navtech, 1994.
- [41] Mehra, R.K. "Identification in Control and Econometrics: Similarities and Differences," *Ann. Econ. Soc. Measurement*, 3: 21-48 (1974).
- [42] Miller, Casey C, Mikel M. Miller, and John Agnew. "On Track For a Personal Best," *GPS World*, 38-42 (March 2001).
- [43] Miller, Mikel, M. Modified Multiple Model Adaptive Estimation (M3AE) for Simultaneous Parameter and State Estimation. Air Force Institute of Technology (AU), Wright-Patterson AFB OH, March 1998 (ADA344312).
- [44] Misra, Pratap, Per Enge. *Global Positioning System Signals, Measurements, and Performance*. Lincoln, MS: Ganga-Jamuna Press 2001.
- [45] Mulvihill, Kim. "Indy 500." *San Francisco Gate*, 29 May 01.
- [46] Nakra, Teresa M. *Inside the conductor's Jacket: Analysis, Interpretation and Musical Synthesis of Expressive Gesture*. PhD dissertation. Massachusetts Institute of Technology, Boston, MD. February 2000.

- [47] "A Personal Computer-Based Physiological Training System," NASA Tech Briefs ARC-14048-2. Moffett Field, California: Ames Research Center, January 2001.
- [48] Porat, B. A Course in Digital Signal Processing. New York: John Wiley and Sons, Inc., 1997.
- [49] Powers, Scott, Stephen Dodd, James Freeman, Gregory D. Ayers, Herman Samson, Tipton McKnight. "Accuracy of Pulse Oximetry to Estimate HbO₂ Fraction of Total Hb During Exercise," Journal of Applied Physiology, 67:300:304 (1989).
- [50] Roblyer, Dwight A. A Toposcopic Investigation of Brain Electrical Activity Induced by Motion Sickness. MS Thesis, AFIT/GSO/ENG/92D-03, School of Engineering, Air Force Institute of Technology (AU), Wright-Patterson AFB OH, November 1992 (ADA259024).
- [51] Sahambi, J.S., S.N. Tandon, and R.K.P. Bhatt. "An automated Approach to Beat-by-Beat QT-Interval Analysis," IEEE Engineering in Medicine and Biology," 97-101 (May/June 2000).
- [52] Sardis, G.N., and R.N. Lobbia. "Parameter Identification and Control of Linear Discrete-time Systems, IEEE Trans. Automat. Control, AC-17: 52-60 (1972).
- [53] Satava, Richard, Peter Angood, Brett Harnett, and Ronald Merrell. "The Physiologic Ciper at Altitude: Telemedicine and real-time monitoring of Climbers on Mount Everest," Journal of Telemedicine and e-Health, 6: 303-313 (September 2000).
- [54] Schimming, Thomas. "Analysis and modeling of ECG Signals Using Nonlinear Methods." <http://lanoswww.epfl.ch/personal/schimmin/uni/beleg/> 20 Jan 02.
- [55] Skolnick, Andrew A. "Monitor Passes First Tests with Flying Colors," JAMA, 279: 736-737 (11 March 1998).
- [56] Smith, Russel B. A Cepstral Analysis of EEG Signals in Motion Sickness Studies. MS Thesis, AFIT/GSO/ENG/89D-1, School of Engineering, Air Force Institute of Technology (AU), Wright-Patterson AFB OH, November 1989 (ADA215663).
- [57] Stamkopoulos T, Maglaveras N, Bamidis PD, and Pappas C. "Wave Segmentation Using Nonstationary Properties of ECG," Computers in Cardiology, IEEE Computer Society Press, Piscataway, NJ: 529-32 (2000).
- [58] Stern, Robert M., William J. Ray, Karen S. Quigley. Psychophysiological Recording. Oxford: University Press, 2001.

- [59] Tripp, Lloyd. Contractor, Veridian Corp., AFRL/HEPA, Wright-Patterson Air Force Base, OH. Personal Interview. 13 Nov 01.
- [60] Vasquez, Carolina, Alfredo Hernandez, Fernando Mora, Guy Carrault, and Gianfranco Passariello. "Atrial Activity Enhancement by Wiener Filtering Using an Artificial Neural Network," IEEE Transactions on Biomedical Engineering, 48: 940-944 (August 2001).
- [61] "Vivometrics Photos and Art." Excerpt from product guide. n. pag. <http://www.vivometrics.com/Press/photogallery/index.html>. 24 Aug 01.
- [62] VivoMetrics, Inc. 121 N. Fir Street Suite E. Ventura, California 93001.
- [63] Vogen, George, S. A topographical Analysis of the Human Electroencephalogram for Patterns in the Development of Motion Sickness. MS Thesis, AFIT/GSO/ENG/91D-17, School of Engineering, Air Force Institute of Technology (AU), Wright-Patterson AFB OH, November 1991 (ADA243656).
- [64] Vullings, H.J.L.M, M.H.G. Verhaegen, H.B. Verbruggen. "Automated ECG segmentation with Dynamic Time Warping," Proceedings of the 20th Annual International Conference of the IEEE Engineering in Medicine and Biology Society. 163-165. New York: IEEE Press, 1998.
- [65] Willsky, Alan S. "A Survey of Design Methods for Failure Detection in Dynamic Systems." Automatic, 12: 601:611 (1976).
- [66] Yelderman, Mark and William New, Jr. "Evaluation of Pulse Oximetry." Anesthesiology, 59: 349-352 (October 1983).
- [67] Zyweitz, Christian and B. Schneider. "Computer Application on ECG and VCG Analysis, North Holland, 1973.

Vita

2Lt Gregory S. Hoffman was born in May 1978 in West Allis, WI. He graduated from Milwaukee Lutheran High School in Milwaukee, WI in June 1996. He entered undergraduate studies at the United States Air Force Academy where he graduated with a Bachelor of Science degree in Electrical Engineering in May 2000 and was commissioned a second lieutenant in the United States Air Force. In August 2000, he entered the Graduate School of Engineering and Management, Air Force Institute of Technology. Upon graduation, he will be assigned to the National Air Intelligence Center.

REPORT DOCUMENTATION PAGE

Form Approved
OMB No. 074-0188

The public reporting burden for this collection of information is estimated to average 1 hour per response, including the time for reviewing instructions, searching existing data sources, gathering and maintaining the data needed, and completing and reviewing the collection of information. Send comments regarding this burden estimate or any other aspect of the collection of information, including suggestions for reducing this burden to Department of Defense, Washington Headquarters Services, Directorate for Information Operations and Reports (0704-0188), 1215 Jefferson Davis Highway, Suite 1204, Arlington, VA 22202-4302. Respondents should be aware that notwithstanding any other provision of law, no person shall be subject to a penalty for failing to comply with a collection of information if it does not display a currently valid OMB control number.

PLEASE DO NOT RETURN YOUR FORM TO THE ABOVE ADDRESS.

1. REPORT DATE (DD-MM-YYYY) 26-03-2002		2. REPORT TYPE Master's Thesis		3. DATES COVERED (From - To) Aug 2000 - Mar 2002	
4. TITLE AND SUBTITLE A Novel Electrocardiogram Segmentation Algorithm Using a Multiple Model Adaptive Estimator			5a. CONTRACT NUMBER		
			5b. GRANT NUMBER		
			5c. PROGRAM ELEMENT NUMBER		
6. AUTHOR(S) Hoffman, Gregory S., 2Lt, USAF			5d. PROJECT NUMBER		
			5e. TASK NUMBER		
			5f. WORK UNIT NUMBER		
7. PERFORMING ORGANIZATION NAMES(S) AND ADDRESS(S) Air Force Institute of Technology Graduate School of Engineering and Management (AFIT/EN) 2950 P Street, Building 640 WPAFB OH 45433-7765			8. PERFORMING ORGANIZATION REPORT NUMBER AFIT/GE/ENG/02M-10		
			10. SPONSOR/MONITOR'S ACRONYM(S)		
9. SPONSORING/MONITORING AGENCY NAME(S) AND ADDRESS(ES)			11. SPONSOR/MONITOR'S REPORT NUMBER(S)		
			12. DISTRIBUTION/AVAILABILITY STATEMENT APPROVED FOR PUBLIC RELEASE; DISTRIBUTION UNLIMITED.		
13. SUPPLEMENTARY NOTES					
14. ABSTRACT This thesis presents a novel electrocardiogram (ECG) processing algorithm design based on a Multiple Model Adaptive Estimator (MMAE) for a physiological monitoring system. Twenty ECG signals from the MIT ECG database were used to develop system models for the MMAE. The P-wave, QRS complex, and T-wave segments from the characteristic ECG waveform were used to develop hypothesis filter banks. By adding a threshold filter-switching algorithm to the conventional MMAE implementation, the device mimics the way a human analyzer searches the complex ECG signal for a useable temporal landmark and then branches out to find the other key wave components and their timing. The twenty signals and an additional signal from an animal exsanguination experiment were then used to test the algorithm. Using a conditional hypothesis-testing algorithm, the MMAE correctly identified the ECG signal segments corresponding to the hypothesis models with a 96.8% accuracy-rate for the 11539 possible segments tested. The robust MMAE algorithm also detected any misalignments in the filter hypotheses and automatically restarted filters within the MMAE to synchronize the hypotheses with the incoming signal. Finally, the MMAE selects the optimal filter bank based on incoming ECG measurements. The algorithm also provides critical heart-related information such as heart rate, QT, and PR intervals from the ECG signal. This analyzer could be easily added as a software update to the standard physiological monitors universally used in emergency vehicles and treatment facilities and potentially saving thousands of lives and reducing the pain and suffering of the injured.					
15. SUBJECT TERMS Physiological monitoring, vital-sign monitoring, MMAE, ECG, Electrocardiogram					
16. SECURITY CLASSIFICATION OF:			17. LIMITATION OF ABSTRACT U	18. NUMBER OF PAGES 177	19a. NAME OF RESPONSIBLE PERSON LtC Mikel M. Miller, USAF
a. REPO RT U	b. ABSTRA CT U	c. THIS PAGE U			19b. TELEPHONE NUMBER (Include area code) 937-255-6565x4278

Standard Form 298 (Rev. 8-98)
Prescribed by ANSI Std. Z39-18